論文 / 著書情報
Article / Book Information

題目(和文)	Cu-Ni-Si系合金における析出強化と変形双晶形成挙動
Title(English)	Deformation Twinning in Relation to Precipitation Strengthening in Cu-Ni-Si alloy
著者(和文)	荒木章好
Author(English)	Akiyoshi Araki
出典(和文)	学位:博士（工学）, 学位授与機関:東京工業大学, 報告番号:甲第9753号, 授与年月日:2015年3月26日, 学位の種別:課程博士, 審査員:里　達雄,小林　郁夫,熊井　真次,竹山　雅夫,曽根　正人
Citation(English)	Degree:, Conferring organization: Tokyo Institute of Technology, Report number:甲第9753号, Conferred date:2015/3/26, Degree Type:Course doctor, Examiner:,,,,
学位種別(和文)	博士論文
Type(English)	Doctoral Thesis

Deformation Twinning in Relation to Precipitation Strengthening in Cu-Ni-Si Alloys

by

Akiyoshi Araki

Doctoral Thesis

Department of Metallurgy and Ceramics Science
Tokyo Institute of Technology

2014

Contents

Chapter 1
General introduction

1.1. Background

The world electricity consumption and the electrification rate have been consistently increasing over 40 years as show in **Fig. 1.1** [1]. The world refined copper usage has been also increasing since 1990 as shown in **Fig. 1.2** [2]. The major reason of the increase of the electricity consumption and the copper usage is the spread of electric appliances such as mobile phone or PC. The reduction of the energy and resource consumption is necessary for the sustainable society as well as the utilization of renewable energy.

Copper based alloys have been extensively used for electrical components due to their high electrical and thermal conductivity, high strength and high corrosion resistance. For developing high performance devices and downsizing of the components as well as for saving energy and resources, it is desired to improve the properties of the copper based alloys. Among various copper alloys, precipitation strengthening alloys are widely used in electrical devises, especially as lead frame and connecter materials which require high strength and electrical conductivity, because of the high strength and medium electrical conductivity of the alloys. The high strength is obtained by the formation of fine precipitates and the medium electrical conductivity is achieved by the decrease of solute atoms resulting from the precipitation.

Cu-Be alloys have the highest strength among the copper based alloys, with relatively high electrical conductivity and good formability. Because of the high cost and environmental unfriendliness of beryllium, however, alternative alloys are now required.

Cu-Ni-Si alloys are also precipitation strengthening alloy and have a good balance between strength and conductivity as shown in **Fig. 1.3** [3] and as such, are expected to replace the Cu-Be alloys. Precipitation strengthening and work hardening are important strengthening method in Cu-Ni-Si alloys. In order to increase the strength of the alloys, therefore, it is required to clarify the precipitation sequence. Therefore, the age hardening behavior of Cu-Ni-Si alloys has attracted interests of many researchers. In contrast, no detailed study about the work hardening behavior of Cu-Ni-Si alloys has been conducted.

1.2. Aging behavior in Cu-Ni-Si alloy

1.2.1. Precipitates formed in Cu-Ni-Si alloy

Cu-Ni-Si alloys in which an atomic ratio of Ni to Si is about two have a significant age hardenability. The precipitation hardening in the alloys was first investigated by Corson and the precipitating phase was identified as δ-Ni_2Si on the basis of the phase diagram [4]. Other possibility for the precipitating phase were also reported. The precipitating phase was identified as γ-Ni_5Si_2 by Okamoto [5] and β-Ni_3Si. The crystal structures of these proposed phases are summarized in **Table.1.1**.

Lockyer and Noble [6] found that the precipitating phase is orthorhombic δ-Ni_2Si in Cu-2Ni-1Si (at. %) aged at 723 K for 7.2 ks using high resolution transmission electron microscopy (HRTEM) with the crystal orientation relationships of $(100)_m||(001)_{ppt}$ and $[011]_m||[010]_{ppt}$. In contrast, Fujiwara and Sato [7] found that two phases of δ-Ni_2Si and Ni_3Si with $L1_2$ structure are formed in Cu-4Ni-2Si (at. %) aged at 773 K for 72 ks and the crystal orientation relationships between Cu matrix and δ-Ni_2Si precipitate were $(110)_m||(001)_{ppt}$ and $[001]_m||[100]_{ppt}$. In both case, the δ-Ni_2Si precipitate formed on (110) of matrix.

The precipitates observed in above reports were at peak-aged condition or a little earlier aging condition. The precipitation process during the early stage of aging which determines the later distribution of precipitates is still not clear. To understand the precipitation process during the early stage of aging in the alloy is necessary in order to obtain maximal strength.

1.2.2. Two-stage age-hardening behavior

It has been found that the hardness of the Cu-Ni-Si alloy changes in stages in under-aged condition. To account for the two-stage hardening behavior of the alloy, Takaku *et al*. [8] proposed that the formation of another phase helps the precipitation of the δ-Ni_2Si phase on the basis of the result of differential scanning calorimetry. However, the mechanism of the two-stage hardening behavior is still not clear.

1.3. Work hardening behavior in Cu-Ni-Si alloys

During fabrication processes, the Cu-Ni-Si alloys are cold worked after aging treatment to obtain thinner materials. Being cold worked, generally, the metallic materials are work hardened due to the dislocation accumulation and the refinement of microstructure. To understand the work hardening behavior is, therefore, important to obtain high strength material. However, no detailed report regarding the work hardening behavior of the alloys has been conducted.

1.3.1. Effect of interaction between precipitates and dislocations on the work hardening behavior

The nature of interaction between dislocations and precipitates significantly affects the work hardening behavior of precipitation strengthened alloys. Cheng *et al.* [9] have reported the influence of precipitates on the work hardening behavior in aluminum alloys and rationalized the changes of the work hardening behavior during aging on the basis of whether precipitates are sheared by mobile dislocations or not.

In Cu-Ni-Si alloys, however, the interaction between precipitates and dislocations is unclear. Lockyer and Noble [6] have considered that the precipitates may be able to be cut by dislocations when the precipitates are very small and the precipitates are no longer cut at peak-aged or longer aged condition because of the complexity of the crystal structure and the orientation relationship with matrix of δ-Ni_2Si.

1.3.2. The twining deformation in Cu-based alloys

It is well known that copper based alloys such as Cu-Zn [10] or Cu-Al [11] which have low stacking fault energy (SFE) show an evidence of deformation twinning which makes the work hardening behavior further complicated. Blewitt *et al*. [12] suggested that deformation twinning also occurs in copper single crystals deformed at low temperature. The deformation twinning is much utilized in the twinning induced plasticity (TWIP) steels for strengthening the materials [13][14]. Though it is unknown whether the deformation twinning occurs in Cu-Ni-Si alloy or not, it is of interest to understand these complicated behaviors in both industrial and academic point of

view. Also, this can provide a new methodology for producing high strength materials.

1.4. Objective of this thesis

As mentioned above, the precipitation sequence during the early stage of aging is of interest in this study. The detailed understanding for the effect of precipitates on the work hardening in the Cu-Ni-Si alloy is also necessary in order to optimize the combination of precipitation hardening and work hardening. The main objectives of the present work is, therefore,

- To identify the precipitating phase in the early stage of aging.
- To clarify the effect of the aging condition on the work hardening behavior of the aged Cu-Ni-Si alloy.

As the study progressed, it was found that the deformation twinning occurs in Cu-Ni-Si alloy and the work hardening behavior is significantly affected by the aging conditions. The following points are also the main objective of this thesis.

- To determine the interaction between precipitates and dislocations at each aging condition.
- To clarify the effect of twinning deformation on the work hardening behavior in the Cu-Ni-Si alloy.
- To clarify the effect of precipitates on the deformation twinning.

1.5. Outline of this thesis

The flow chart of the present work is given in **Fig. 1.4**.

Chapter 1 is **"General introduction"**, where background, current problems and the objectives of this study are described.

The precipitation behavior and the two-stage hardening behavior in Cu-Ni-Si alloy are investigated using hardness and electrical resistivity measurement, DSC and TEM. This work is presented in Chapter 2 **"Precipitation behavior in Cu-Ni-Si alloy".**

The change of the interaction between precipitates and dislocations during aging treatment is discussed on the basis of the work hardening behavior and Bauchinger effect. This work is presented in Chapter 3 **"Work hardening behavior in Cu-Ni-Si alloy".**

In chapter 3, deformation twins were found to form in the Cu-Ni-Si alloy. The deformation twinning behavior in the Cu-Ni-Si alloy was investigated by lowering the stacking fault energy in Chapter 4 **"Deformation twinning behavior in Cu-Ni-Si alloys".**

From the obtained understandings about the precipitates-dislocations interaction and the deformation twinning, the effect of the precipitates on the deformation twinning is discussed in Chapter 5 **"Effect of precipitates on deformation twinning".**

Finally, the results and conclusions from Chapter 2 to 5 are summarized comprehensively in Chapter 7 **"General conclusions".**

Reference

[1] International Energy Agency, Energy balance flow,
quoted from http://www.iea.org/Sankey/index.html#?c=World&s=Final consumption

[2] International Copper Study Group: *The World Copper Factbook 2014*, 36
downloaded on November 15, 2014 from
http://www.icsg.org/index.php/component/jdownloads/viewdownload/170/1959

[3] National Institute of Materials Science: Press release (Dec. 2005)
downloaded on November 10, 2014 from
http://www.nims.go.jp/news/press/2005/12/200512050/p200512050.pdf

[4] M.G. CORSON, Trans. AIME (1927) 435

[5] M. OKAMOTO Trans. Inst. Met. Jpn **3**(9) (1939) 336.

[6] S.A. Lockyer and E. F. Noble: J. Mater. Sci., **29** (1994), 218.

[7] M. Fujiwara and T. Sato: J. Japan Inst. Metals, **62** (1998), 301.

[8] A. Takaku, A. Araki, Y. Ishizuka, E. Kobayashi, T. Sato, K. Hirose and T. Eguchi: J. of the JRICu, **50** (2011), 38.

[9] L.M. Cheng, W.J. Poole, J.D. Embury and D.J. Lloyd: Metall. Mater. Trans. A, **34** (2003), 2473.

[10] Y. Nakao and H. Miura: Mater. Sci. Eng. A, **528** (2011), 1310.

[11] M. Niewczas and G. Saada: Philos. Mag. A, **82** (2002), 167.

[12] T. H. Blewitt, R. R. Coltman and J. K. Redman: J. Appl. Phys., **28** (1957), 651.

[13] O. Grässel, L. Krüger, G. Frommeyer and L. W. Meyer: Int. J. of Plasticity **16** (2000) 1391.

[14] S. Allain, J.-P. Chateau and O. Bouaziz: Mater. Sci. and Eng. A **387-389** (2004), 143.

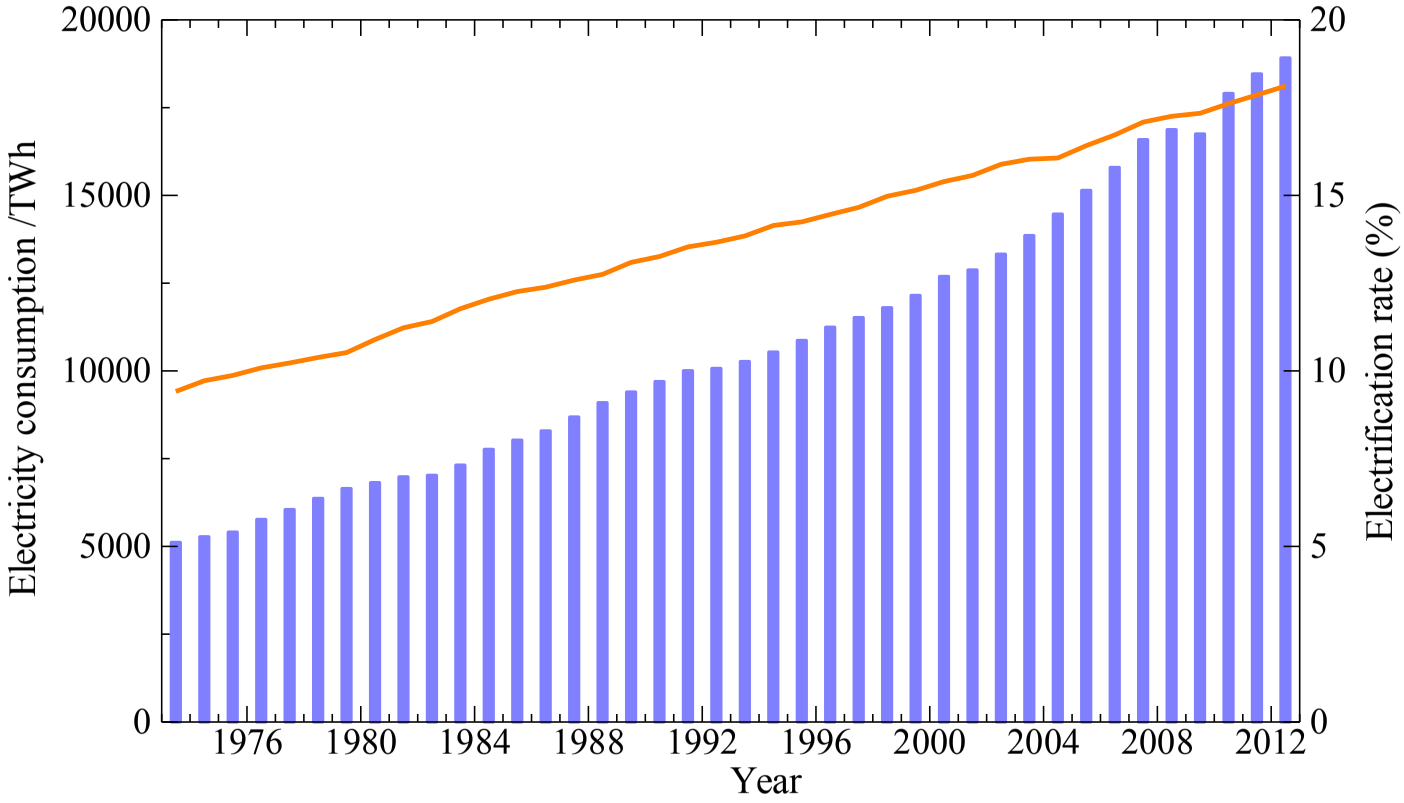

Fig. 1. 1 The world electricity consumption and the electrification rate [1].

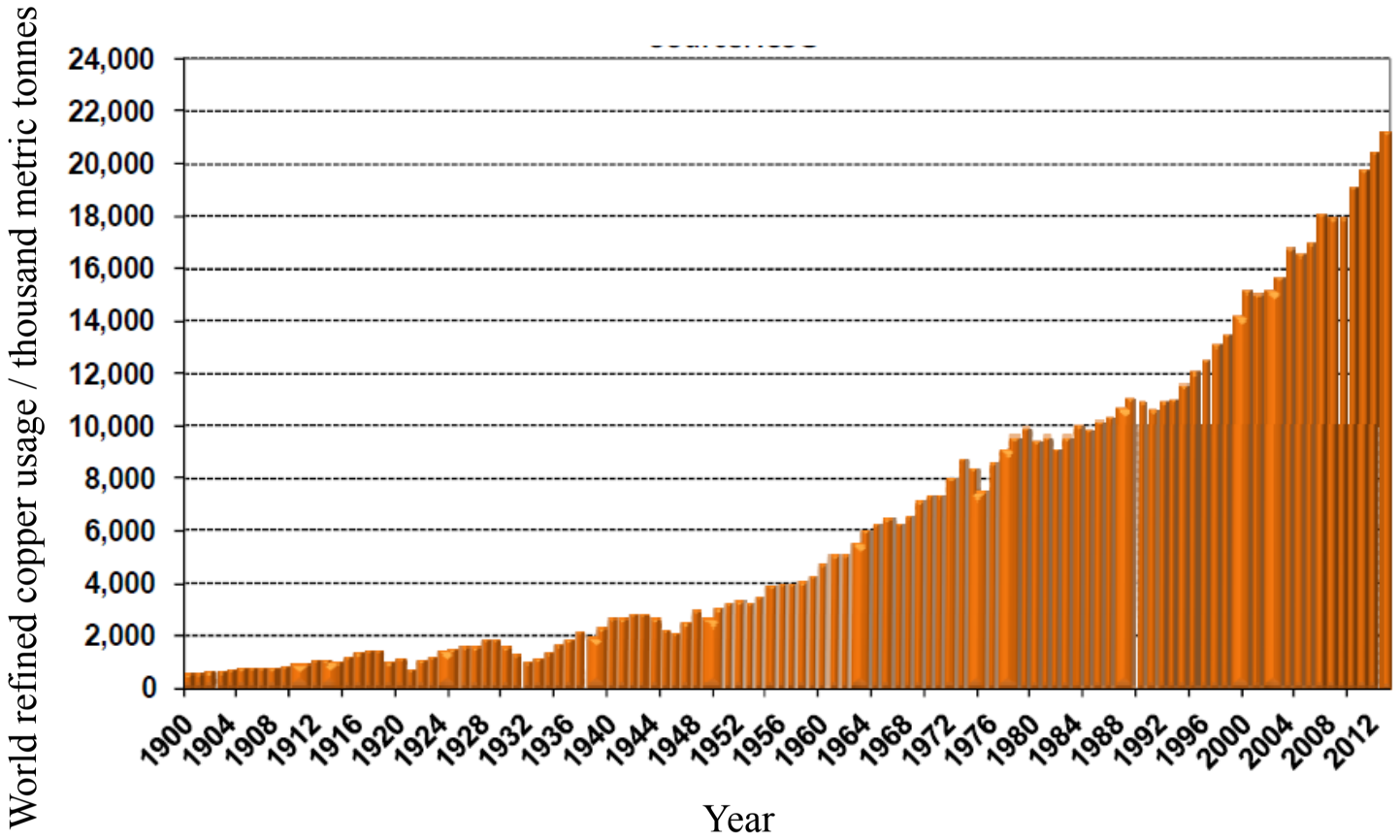

Fig. 1. 2 The world refirned copper usage [2].

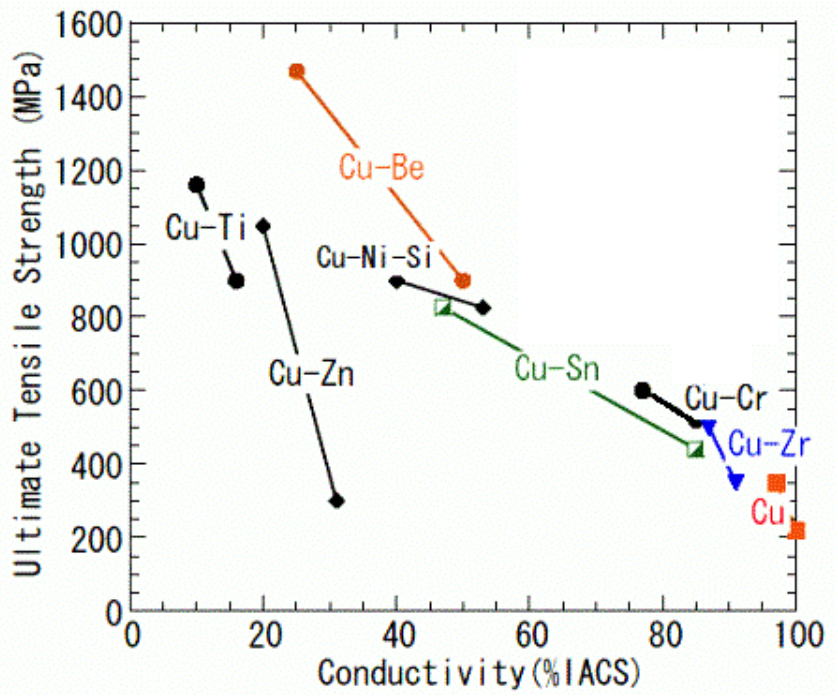

Fig. 1.3 The relation between the strength and electrical conductivity [3].

Table 1.3 The crystal structure of several nickel silicide.

Phase	Crystal structure	Axis constant / nm			Ni/Si
		a	b	c	
Cu	fcc	0.362	0.362	0.362	-
Ni_3Si	$L1_2$	0.351	0.351	0.351	3
Ni_5Si_2	Trigonal	0.667	0.667	1.229	2.5
Ni_2Si	Orthorhombic	0.706	0.499	0.372	2
Ni_3Si_2	Orthorhombic	1.223	1.081	0.692	1.5

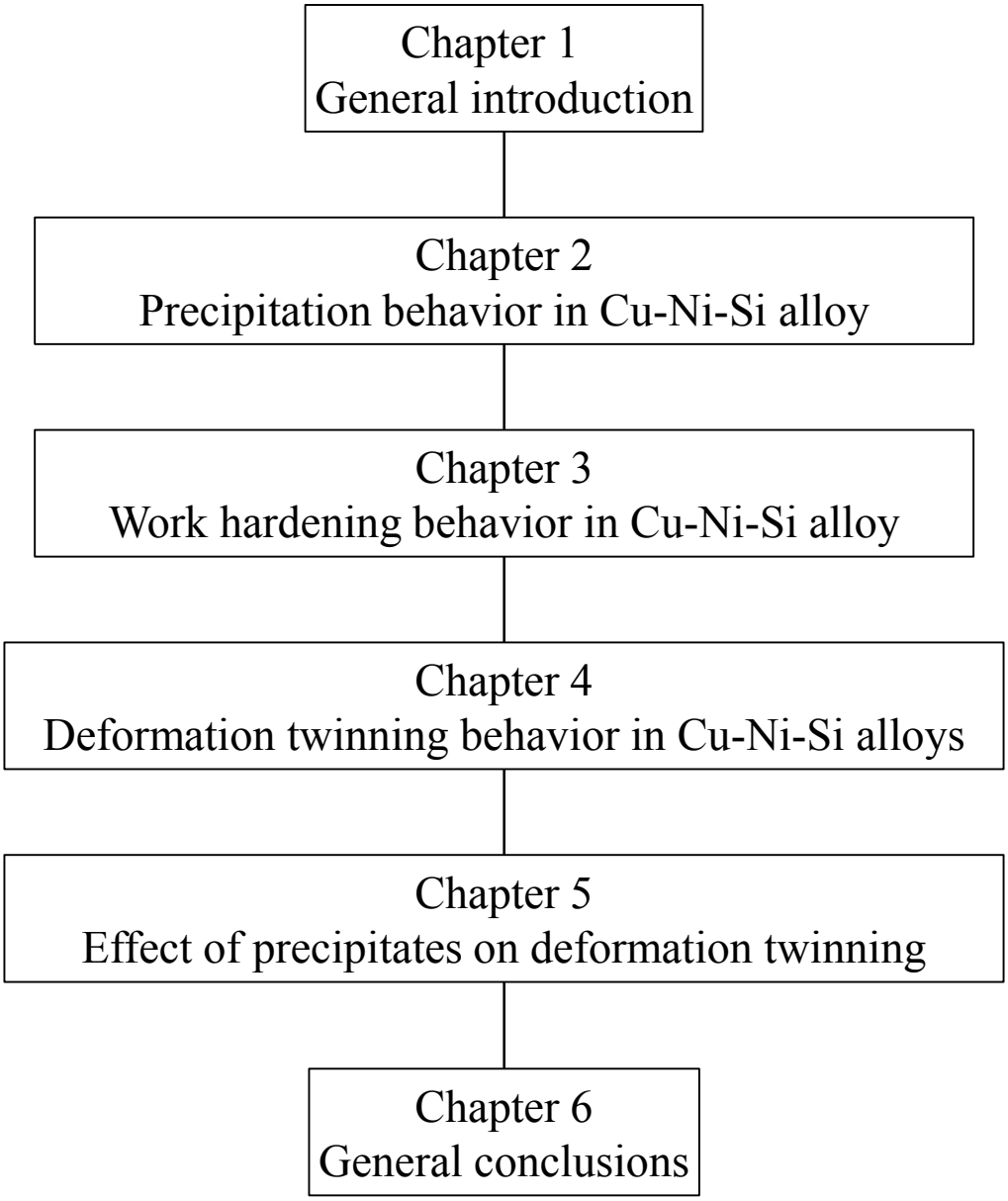

Fig. 1.4 Outline of the present thesis.

Chapter 2
Precipitation behavior in Cu-Ni-Si alloy

2.1. Introduction

It is clear that the precipitates formed in the early stage significantly affect the precipitate distribution in peak-aged condition and the peak strength in precipitation strengthening alloys. Many reports including by Lockyer and Noble [1], Fujiwara and Sato [2] and Monzen and Watanabe [3] identified the precipitating phase at peak-aged condition as δ-Ni_2Si from transmission electron microscopy (TEM). The orientation relationships between the copper matrix and δ-Ni_2Si phase are also identified as $(100)_m//(001)_{ppt}$ and $[011]_m//[010]_{ppt}$ [1]. However, Takaku *et al*. [4] found that two exothermic reactions occurs during heating process by differential scanning calorimetry (DSC), and proposed the formation of another phase, called X phase. Takaku *et al.* [4] also reported that the δ-Ni_2Si precipitates preferentially formed on dislocations or on the other phase because of the difference between the crystal structures of copper matrix and δ-Ni_2Si, resulting in relatively low activation energy of the forming reaction. Zhao *et al.* [5] reported that the spinodal decomposition and the formation of $(Ni, Cu)_3Si$ with DO_{22} structure prior to the formation of δ-Ni_2Si cause the two-stage hardening behavior. As mentioned in chapter 1, however, the precipitation sequence during the early stage of aging and the two-stage hardening behavior appeared in under-aged condition are still not clear.

In this chapter, detailed TEM observation and DSC analysis have been conducted for a Cu-Ni-Si alloy with various aging conditions in order to investigate the precipitation behavior during the early stage of aging at 723 K. The direct observation using TEM is the most convincing evidence to identify the precipitating phase. The precipitates are, however, too difficult to observe during the early stage of aging because the size is very small. In contrast, DSC is useful to investigate the precipitation reaction during the early stage of aging when the solute concentration is high. The activation energy of the two exothermic reactions has also been investigated by applying Kissinger method [6] in order to estimate each reactions. In addition, the hardness and electrical resistivity changes during aging treatment with different conditions of solution heat treatment have been investigated in order to clarify the effect of dislocation density on the precipitation behavior.

2.2. Experimental procedure

The chemical composition of the alloy used in this work is listed in **Table 2.1**. The ingot was homogenized at 1223 K and hot rolled, then cold rolled by about 90 % in thickness. The sheet material was solution-treated with various conditions as summarized in **Table 2.2** using salt bath, subsequently water-quenched. The specimens are designated using the condition of solution heat treatment. For instance, the "1123-600" stands for the specimen solution-treated at 1123 K for 600 s. The grain size and expected dislocation density are summarized in Table 2.2. The specimens were then artificially aged using salt bath at 573 K or at 723 K for up to 1206.9 ks. The heat treatment process is illustrated in **Fig. 2.1**.

Micro-Vickers hardness was measured with a load of 300 g for 15 s. Electrical conductivity is measured by eddy current method using Auto Sigma 3000., then the electrical resistivity was calculated form the conductivity. The DSC analyses were carried out using a Rigaku Thermo plus EVO II/DSC8230 with platinum plate as a reference under an argon flow atmosphere. The specimens for the DSC analysis were prepared as discs with a mass of 140 mg. In order to investigate the precipitation microstructure at each aging condition, TEM observations were carried out using JEOL JEM-3010 transmission electron microscope operating at 300 kV, for the specimens aged for various times.

2.3. Results

2.3.1. DSC analysis for as solution treated Cu-Ni-Si alloy

Fig. 2.2 shows the DSC curves for the 1123-600 specimen conducted with different heating rate. Two exothermic reactions, reaction A and reaction B, are detected in all the curves. The peak-top temperatures of each reaction with different heating rate are summarized in **Table 2.3**. The peak-top temperatures had good duplicability. The apparent activation energy for the reactions was estimated by applying Kissinger method as shown in **Fig. 2.3**. The relation among the heating rate, peak-top temperature and activation energy is given as follows,

$$\frac{d\left(\ln\frac{\gamma}{T_{\mathrm{p}}{}^{2}}\right)}{d\left(\frac{1}{T_{\mathrm{p}}}\right)} = -\frac{E_{\mathrm{a}}}{R} \tag{2.1}$$

where γ is the heating rate, T_{p} is the peak-top temperature and E_{a} is the activation energy of the reaction. The activation energy for the reaction A and B calculated from the tangent of the line are summarized in **Table 2.4**.

2.3.2. Hardness, electrical resistivity, DSC curve and the microstructure changes of Cu-Ni-Si alloy during aging treatment at 573K.

The hardness and electrical resistivity changes of the 1123-600 specimen aged at 723 K are shown in **Fig. 2.4**. The two-stage hardening behavior also appeared during 573 K aging.

Fig. 2.5 shows the DSC curves for the 1123-600 specimen aged at 573 K for various times up to 1209.6 ks measured with a heating rate of 0.167 K/s. Two exothermic reactions, reaction A and reaction B, are detected in the curve for the as-solution-treated specimen. The exothermic peak due to the reaction A became smaller until the aging condition of 0.060 ks as aging progressed and being not detected after the aging condition of 0.060 ks. The exothermic peak due to the reaction B first became larger until 0.060 ks and then became smaller as aging progressed, finally disappeared after the aging time of 0.60 ks. Furthermore, an endothermic reaction C appeared after the aging time of 3.6 ks. The peak top temperature of the endothermic reaction C is lower than that of the reaction B.

Fig. 2.6 shows the microstructure and the corresponding diffraction pattern of the specimen aged at 573 K for 1209.6 ks. The precipitates formed on the dislocation were observed. In contrast, very small strain contrasts with about 1 nm in diameter were observed in the matrix. The calculated diffraction pattern for δ-Ni_2Si phase in Cu matrix is also given in Fig. 2.6. The diffraction pattern obtained from the specimen aged at 573 K was totally different with the calculated pattern for the δ-Ni_2Si phase.

2.3.3. Hardness, electrical resistivity, DSC curve and the microstructure changes of the Cu-Ni-Si alloy aged at 723 K.

The hardness and electrical resistivity changes of the 1123-600 specimen during aging at 723 K are shown in **Fig. 2.7**. The hardness remarkably changed in stages in under-aged range as aging progressed as mentioned in introduction. One can see the electrical resistivity also changed in stages, that is, the resistivity dramatically drops during the early stage of aging until about 0.60 ks, and then the dropping rate decreased. The drop in electrical resistivity is a result of the decrease of the solute atoms in copper matrix due to the formation of precipitates. It is obvious, therefore, that the precipitation drastically happens during the early stage of aging up to about 0.60 ks. It is also worth noting that the precipitation goes on even during the over-aged condition.

Fig. 2.8 shows the DSC curves for the 1123-600 specimen aged at 723 K for various times up to 345.6 ks measured with a heating rate of 0.167 K/s. The exothermic peak due to the reaction A was not detected after 0.060 ks aging. The peak due to the reaction B became small as aging progressed and finally disappeared after the aging time of 0.60 ks. Furthermore, an endothermic reaction D appeared after 0.060 ks aging condition. In contrary with the case aged at 573 K, the peak-top temperature of the endothermic reaction D was higher than that of the reaction B.

The microstructures in the 1123-600 specimen aged at 723 K for various times from 0.30 ks up to 345.6 ks are shown in **Fig. 2.9**. The corresponding selected area diffraction patterns (SADPs) are shown in **Fig. 2.10**. The fine precipitates with disk shape formed on (110) of matrix were found in all aging condition after 0.30 ks, growing as aging progressed. The fast Fourier transformed HRTEM image for the 0.60 ks aged 1123-600 specimen is given in **Fig. 2.11** and showing good agreement with the calculated diffraction pattern for the δ-Ni_2Si phase. In contrast, the diffraction pattern of the specimen aged for 0.30 ks was consistent with the patterns of the specimen aged at 573 K as allowed in Fig. 2.11.

The diffraction patterns over the 0.60 ks consistent with the calculated patterns for the δ-Ni_2Si. The change of the average precipitate diameter obtained from the HRTEM images are plotted as a function of aging time in **Fig. 2.12**. The previous study about the change of the precipitate size by Lockyer and Noble for the Cu-2a.t%Ni-1at.%Si aged at 723 K [1] is also given in the Fig. 2.12.

The change in the average precipitate diameter after 3.6 ks shows a good consistency with the Lockyer's observation. One can see that the average size of precipitate is almost constant from the aging time of 0.30 ks to 1.2 ks, where the two-stage hardening behavior appears. In contrast, the size drastically increase after the aging time of 3.6 ks.

2.3.4. Hardness and electrical resistivity changes and the DSC curve of Cu-Ni-Si alloy with various conditions of solution heat treatment

The hardness and electrical resistivity changes of the specimens with various solution treatment conditions aged at 723 K are shown in **Fig. 2.13**. The change behaviors of both hardness and resistivity were different among the specimens and the two-stage hardening behavior was the most remarkable in 1123-600 specimen.

The increment of the hardness, ΔHV, and the decrement in the resistivity, $\Delta\rho$, from the as-solution-treated condition are plotted in **Fig. 2.14**. The ΔHV and $\Delta\rho$ were defined as

$$\Delta\mathrm{HV} = \mathrm{HV}(t) - \mathrm{HV}(\mathrm{AQ}) \tag{2.2}$$

$$\Delta\rho = \rho(t) - \rho(\mathrm{AQ}) \tag{2.3}$$

where HV(t) and $\rho(t)$ are the hardness and electrical resistivity at the aging time of t, respectively.

The DSC curves for the as-solution-treated specimens with various conditions for the solution heat treatment are shown in **Fig. 2.15**. The exothermic peaks due to the reaction A and B are observed in all the specimen.

2.4. Discussion

2.4.1. Precipitation behavior of Cu-Ni-Si alloy.

First of all, in this section, the precipitation behavior of the 1123-600 specimen will be discussed because the specimen has the largest grain size and lowest dislocation density as shown in Table 2.2 so that the most fundamental precipitation behavior can be discussed.

It has been reported that the exothermic reaction B is consistent with the precipitation of δ-Ni_2Si

phase and the endothermic reaction D is consistent with the solidification of the formed δ-Ni_2Si [4]. Also, it has been proposed that the reaction A indicates the formation of the other phase called X phase. The activation energy analysis revealed that the temperature dependency of the reactions is different. Generally, the higher activation energy of a reaction is, the higher temperature dependency of the rate constant of the reaction is when the reaction is Arrhenius type. Therefore, it can be considered that the temperature dependency of the reaction A corresponding the formation of X phase is higher than that of reaction B corresponding the precipitation of δ-Ni_2Si.

The change of DSC curve during the aging treatment at 573 K indicates that the reaction A first occurs from very early stage of aging before 0.060 ks and the reaction B occurs after 0.60 ks. The facts that the diffraction pattern of the specimen aged for 1209.6 ks shows completely different pattern from the calculated pattern of δ-Ni_2Si phase and the endothermic reaction C appears at lower temperature than the temperature of reaction B revealed the main precipitating phase at 573 K is different from the δ-Ni_2Si phase. Therefore, the endothermic reaction C detected in the DSC curves in Fig. 2.5 can be considered as the dissolution of such fine precipitates.

It was found that the precipitates were formed on the {110} planes of matrix in all aging conditions after the aging treatment at 723 K for 0.30 ks in the specimen. As mentioned in introduction, the δ-Ni_2Si phase forms on the {110} planes of the copper matrix with disk shape. The corresponding diffraction patterns also consistent with the calculated pattern for the δ-Ni_2Si except for the diffraction pattern for the 0.30 ks aged specimen. The diffraction pattern of 0.30 ks aged was consistent with that of the specimen aged at 573 K. The precipitating phase formed before 0.30 ks will be discussed in later part of this section. The fast Fourier transformed image shown in Fig. 2.11 revealed that the precipitate observed in the specimen aged at 723 K for 0.60 ks was the δ-Ni_2Si phase. In addition, all the precipitates observed by TEM show two kinds of periodicity along their apparent length direction and in transverse direction, which indicate that the precipitates are δ-Ni_2Si [1]. Above all, the precipitating phase forming after the aging of 0.30 ks is identified as δ-Ni_2Si.

The precipitation behavior before the aging of 0.30 ks will be discussed on the basis of DSC result.

The facts that the exothermic peak due to the reaction A is not detected after 0.060 ks and the diffraction pattern of the specimen aged at 723 K for 0.30 ks has different spots from the δ-Ni_2Si indicates that the reaction A corresponding the formation of the X phase also occurs during the early stage of aging at 723 K. From the fact that the exothermic peak due to the reaction B decreases and the endothermic reaction C appears from 0.060 ks, however, it is obvious that the reaction B also occurs after the aging treatment of 0.060 ks at 723 K. Furthermore, Takaku *et al.* [4] had investigated the activation energy for the first stage of the two-hardening behavior, and is was 90 kJ/mol based on the Arrhenius plot and 83 kJ/mol based on the Johnson-Mehl-Avrami equation. The activation energy of 94.6 kJ/mol for the reaction B calculated in this work is very close to these values. From the above discussion, the main precipitating phase forming before 0.30 ks is also identified as δ-Ni_2Si though the formation of the X phase corresponding with the reaction A also occurs. Considering the diffraction pattern after 0.60 ks of aging at 723 K, the X phase change to the δ-Ni_2Si phase or dissolve into the matrix by further aging treatment. The relation between the X and δ-Ni_2Si phases is still not clear.

Now it is revealed that the precipitating phase in the Cu-Ni-Si alloy is mainly δ-Ni_2Si phase at 723 K and is mainly X phase at 573 K. **Fig. 2.16** shows the relation between the increment of the hardness as a function of the change of the electrical resistivity at each aging temperature. The resistivity change indicates the volume fraction of the precipitates. It is obvious that the precipitate formed at 573 K, has lower contribution to the hardness than the precipitates formed at 723 K. That is, the X phase is weaker obstacle than the δ-Ni_2Si.

2.4.2. Change in volume fraction and number density of δ-Ni_2Si precipitate during the aging treatment at 723 K

Now, the precipitating phase in the Cu-Ni-Si alloy aged at 723 K have been identified as δ-Ni_2Si after the 0.060 ks aging. In order to investigate more detail of the precipitation behavior, the volume fraction and number density of precipitates was estimated from the electrical resistivity decrement and the average precipitate size.

In general, the specific electrical resistivity, ρ, is expressed by following equation,

$$\rho = \rho_{\mathrm{D}} + \rho(T) \tag{2.4}$$

where ρ_D is the specific resistivity of the material at 0 K, related to the purity and lattice defects and called residual resistivity. The $\rho(T)$ is the contribution of the lattice vibration of matrix which is proportional to T at high temperature and T^5 at low temperature. The ρ_D can be expressed as

$$\rho_{\mathrm{D}} = \rho_{\mathrm{chem}} + \rho_{\mathrm{phs}} \tag{2.5}$$

where ρ_{chem} is the contribution to the specific resistivity due to the chemical defects like solute atoms and ρ_{phs} is the contribution to the specific resistivity due to the physical defects like the vacancies and dislocations. Now, using Matthiessen's rule,

$$\rho_{\mathrm{chem}} = \sum C^i \Delta\rho^i(T) \tag{2.6}$$

the specific resistivity in an alloy is given as

$$\rho = \sum C^i \Delta\rho^i(T) + \rho(T) + \rho_{phs} \tag{2.7}$$

where C^i is the molar concentration of solute element, i, and $\Delta\rho^i$(T) is the resistivity contribution per molar concentration of the element at a temperature T. In this work, all the specific resistivity was measured at room temperature, i.e. T = room temperature.

Now, the specific resistivity change, $\Delta\rho$, during aging treatment is expressed as

$$\Delta\rho = \sum \Delta C^i \Delta\rho^i(T) \tag{2.8}$$

where ΔC^i is the molar concentration change of solute element, i, during aging treatment. The resistivity contribution of the solute element in the specimen at room temperature is given in **Table. 2.4**.

In this work, the molar concentration of solute Ni and Si is decreased as aging proceed because the precipitating phase at 723 K is identified as δ-Ni_2Si. Forming one mole of δ-Ni_2Si, two mole of Ni and one mole of Si is decreased from the matrix. Therefore, the resistivity change can be expressed using the amount of formed precipitate, X_{ppt}, as follows,

$$\Delta\rho = \Big(2 \times \Delta\rho^{\mathrm{Ni}}(\text{room temperature}) + \Delta\rho^{\mathrm{Si}}(\text{room temperature})\Big) \times X_{\mathrm{ppt}} \tag{2.9}$$

The total volume of the precipitate, V_{ppt}, can be calculated as,

$$V_{\mathrm{ppt}} = \frac{M_{\mathrm{Ni_2Si}}}{d_{\mathrm{Ni_2Si}}} \times X_{\mathrm{ppt}} \tag{2.10}$$

where $M_{\mathrm{Ni_2Si}}$ is the molecular weight of δ-Ni_2Si, that is 145.47, and $d_{\mathrm{Ni_2Si}}$ is the specific weight, that is 7.23 g cm^{-3} [7].

The volume of specimen does not change during aging treatment, therefore, the total volume of specimen, V_{total}, can also be estimated as,

$$V_{\mathrm{total}} = \frac{M_{\mathrm{matrix}}}{d_{\mathrm{matrix}}} \tag{2.11}$$

In this work, the value of M_{Cu} and d_{Cu} is used as M_{matrix} and d_{matrix}, respectively.

Now, the volume fraction of the δ-Ni_2Si precipitate is given as

$$f = \frac{V_{\mathrm{ppt}}}{V_{\mathrm{total}}} \tag{2.12}$$

Finally, the number density of the precipitate, n, is given as,

$$n = \frac{f}{v_{\mathrm{ppt}}} \tag{2.13}$$

where v_{ppt} is the average precipitate volume calculated from the average precipitate size (Fig. 2.12).

The estimated number density of δ-Ni_2Si precipitate is plotted in **Fig. 2.17** as a function of aging time. The number density increases until 0.60 ks and then decreases after 0.60 ks. This result indicates that the nucleation of the δ-Ni_2Si precipitates is the main reaction until 0.60ks and the growth of the precipitates is the major reaction rather than the nucleation after the aging condition of 0.60 ks at 723 K.

2.4.3. Effect of solution heat treatment on the two-stage hardening behavior

The hardness and resistivity changes during the early stage of aging were different among the specimens with various conditions of solution treatment. It is obvious that the increment in hardness

at peak-aged condition is the lowest in the 1073-30 specimen among the specimens. It has been reported that the δ-Ni_2Si preferentially forms on dislocations and such precipitates grows faster than the ones formed in matrix because of the high diffusion rate on the dislocation. In fact large precipitates formed on the dislocations were observed in Fig. 2.6. The smallest increment of the hardness in the 1073-30 specimen is, therefore, caused by the preferential formation of the precipitates on the dislocations because the 1073-30 specimen has the largest dislocation density as shown in Table 2.2.

One can also see the changes of hardness and resistivity where the two-stage hardening behavior appears are different among the specimens. The correlations of the magnitude of both the hardness and resistivity changes among the specimens at the early stage of aging is shown as following,

$$1073\text{-}30 > 1123\text{-}30 > 1123\text{-}600 \qquad (2.14)$$

The largest change in the 1073-30 is caused by the formation of the precipitates on the dislocation.

The peak area of the reaction A and B in DSC curves are also different among the specimens and the correlations are

reaction A $\qquad 1123\text{-}600 > 1123\text{-}30 > 1073\text{-}30 \qquad (2.15)$

reaction B $\qquad 1073\text{-}30 > 1123\text{-}30 > 1123\text{-}600 \qquad (2.16)$

These correlations indicate that the more the X phase forms, the less the δ-Ni_2Si forms and thus the formation of X phase and δ-Ni_2Si is competitive. As revealed in section 2.4.2, both the X phase and δ-Ni_2Si phase form during the early stage of the aging at 723 K. The correlation about the reaction A indicates that the lower the dislocation density is, the more the X phase forms. Furthermore, the two-stage hardening behavior is most remarkable in the 1123-600 specimen with the lowest dislocation density, in which the X phase easily forms. The two-stage hardening behavior is, therefore, caused by the formation of X phase.

From the above discussion, the formation of X phase and δ-Ni_2Si phase are illustrated in **Fig. 2.18** and **Fig. 2.19** when the dislocation density is low and high, respectively. In both case, the δ-Ni_2Si precipitates preferentially forms on the dislocations. When the dislocation density is low, the

X phase which is weaker obstacle than the δ-Ni_2Si phase easily forms in matrix compared to when the dislocation density is high, resulting in the small hardness change in the early stage of aging and cause the remarkable two-stage hardening behavior. When the dislocation density is high, the δ-Ni_2Si phase easily form on the dislocation density, resulting large hardness change in the early stage of aging and the small increment of hardness at the peak-aged condition.

2.5. Conclusion

The precipitation behavior of the Cu-Ni-Si alloy has been investigated.

(1) Two exothermic reactions corresponding the formation of X phase and δ-Ni_2Si phase occur during heating process. The activation energy for the reactions is estimated as 150 kJ/mol for the formation of X phase and 94.9 kJ/mol for the formation of δ-Ni_2Si phase.
(2) The main precipitating phase is X phase during the aging treatment at 573 K. In contrast, the main precipitating phase is δ-Ni_2Si phase during the aging treatment at 723 K.
(3) The two-stage hardening behavior is caused by the formation of the weak obstacle of the X phase during the early stage of aging treatment at 723 K.
(4) During the aging treatment at 723 K, the highest number density of δ-Ni_2Si precipitate is about 2.7×10^{24} m^{-3} at the aging time of 0.60 ks in the specimen with low dislocation density. The average precipitate diameter and the number density at peak-aged condition were 9.65 nm and 8.1×10^{22} m^{-3}.

Reference

[1] S.A. Lockyer and E. F. Noble: J. Mater. Sci., **29** (1994), 218.

[2] M. Fujiwara and T. Sato: J. Japan Inst. Metals, **62** (1998), 301.

[3] R. Monzen and C. Watanabe: Mater. Sci. Eng. A, **483-484** (2008), 117.

[4] A. Takaku, A. Araki, Y. Ishizuka, E. Kobayashi, T. Sato, K. Hirose and T. Eguchi: J. of the JRICu, **50** (2011), 38.

[5] D. Zhao, Q.M. Dong, P. Liu, B.X. Kang, J.L. Huang and Z.H. Jin: Mater. Sci. Eng. A **361** (2003), 93.

[6] H. E. Kissinger: Journal of Research of the National Bureau of Standards, **57** (1956) 217.

[7] K. Tomas: Acta. Cryst., **5** (1952) 329

Table 2.1 Chemical composition of the specimens

	Ni	Si	Sn	Zn	Mg	Cu
mass%	2.17	0.50	0.15	0.50	0.10	Bal.
mol%	2.33	1.12	0.080	0.48	0.26	Bal.

Table 2.2 Conditions of solution treatment

Specimens	Temperature	Time	Grain size	Dislocation density
1123-600	1123 K	600s	150 μm	Low
1123-30	1123 K	30s	50 μm	Medium
1073-30	1073 K	30s	10 μm	high

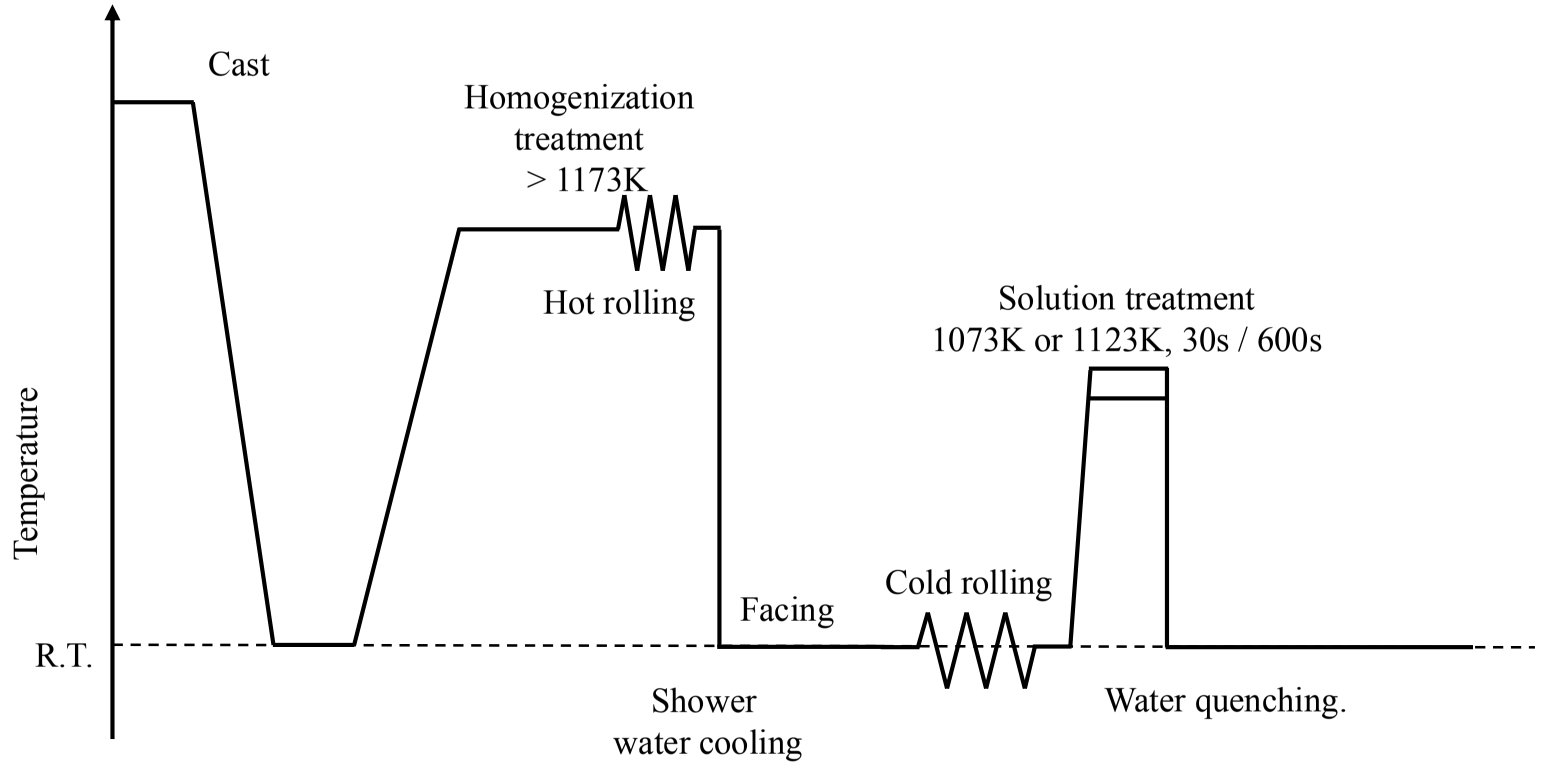

Fig. 2. 1 Schematic illustration of fabrication process of specimens.

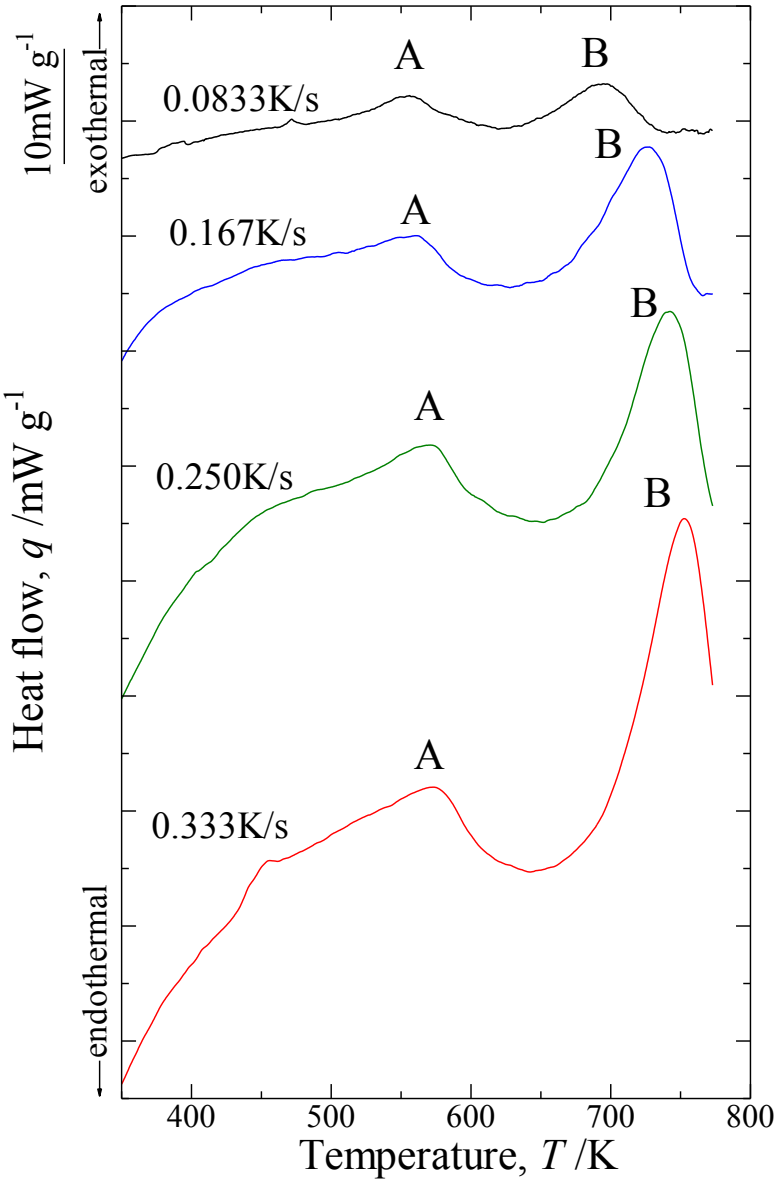

Fig. 2.2 DSC curves of the 1123-600 specimen with various heating rates.

Table 2.3 Peak top temperatures of peak A and B with various heating rates.

Heating rate, γ/K s^{-1}	Peak top temperature, T_p /K			
	Reaction A		Reaction B	
0.0833	556.1	551.2	694.7	695.5
0.167	561.4	560.0	726.8	726.8
0.250	562.3	570.8	743.4	742.6
0.333	573.4	574.7	752.7	739.5

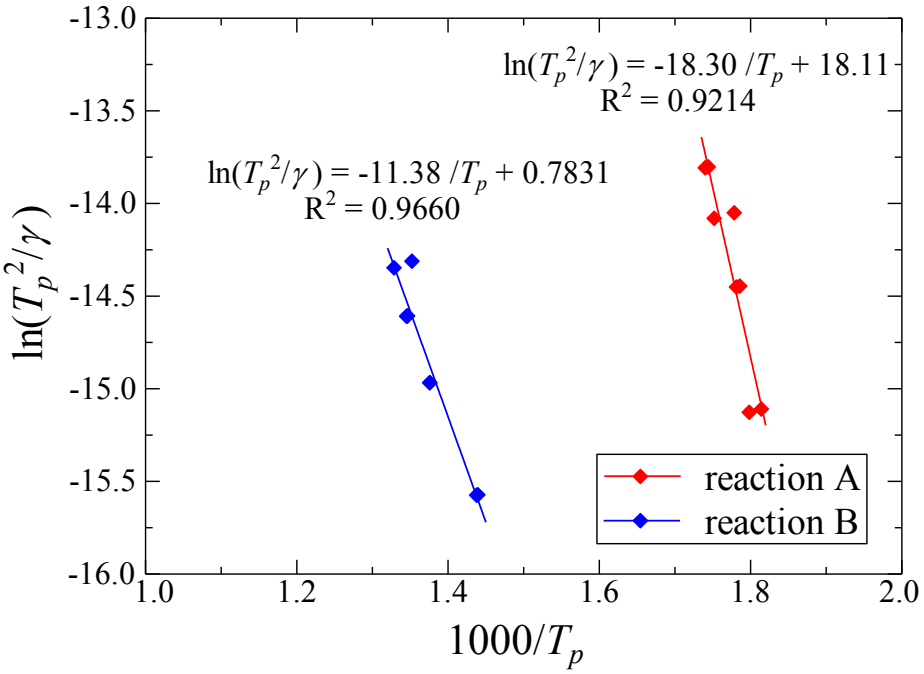

Fig. 2.3 Kissinger plots[6] for peak top temperatures of reaction A and reaction B.

Table 2.4 Activation energy of reaction A and reaction B estimated from Kissinger plot for peak top temperatures.

Reaction	Activation energy, E /kJ mol^{-1}
A	152
B	94.6

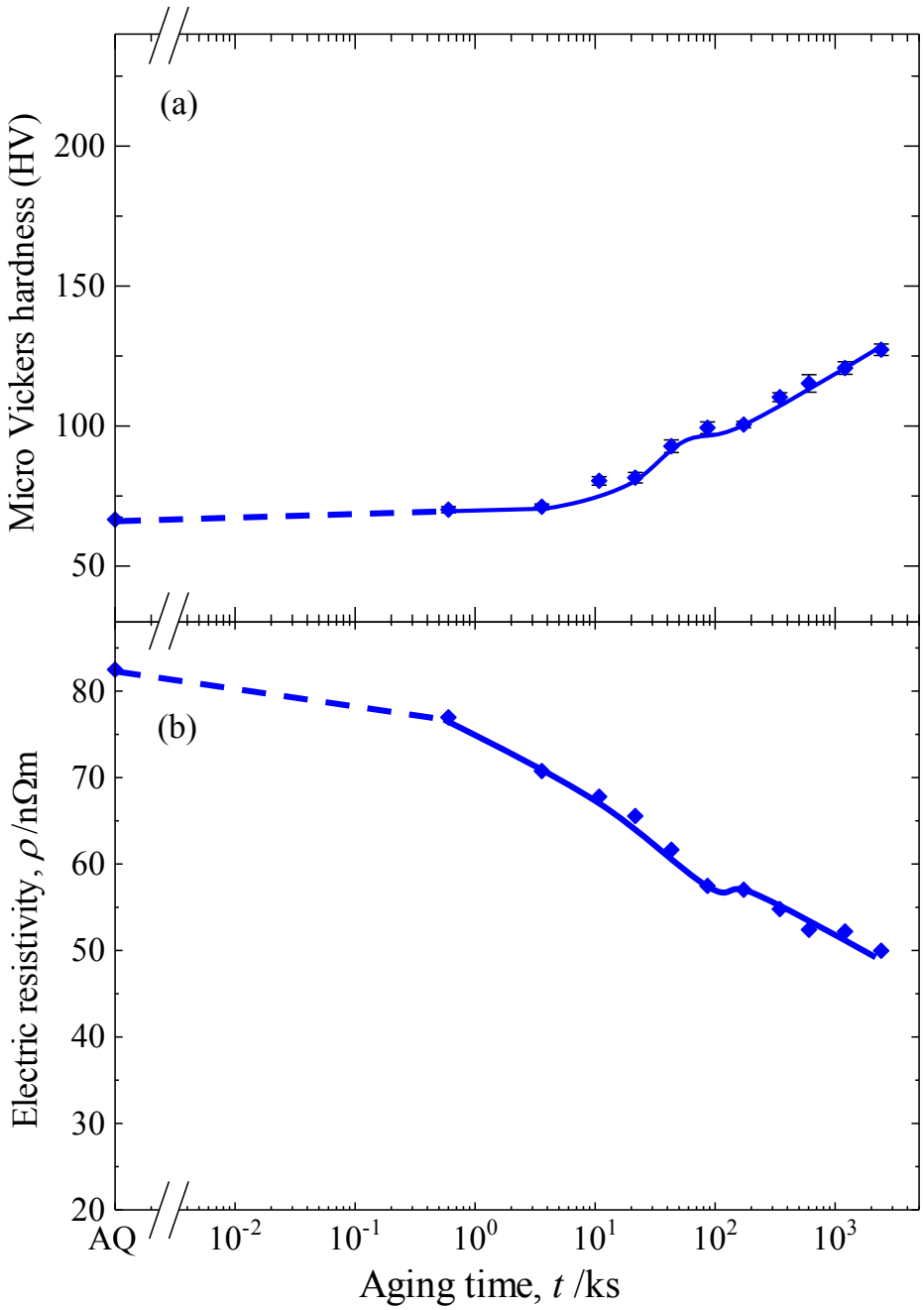

Fig. 2.4 (a) Micro Vickers hardness and (b) electrical resistivity of the 1123-600 specimen aged at 573 K.

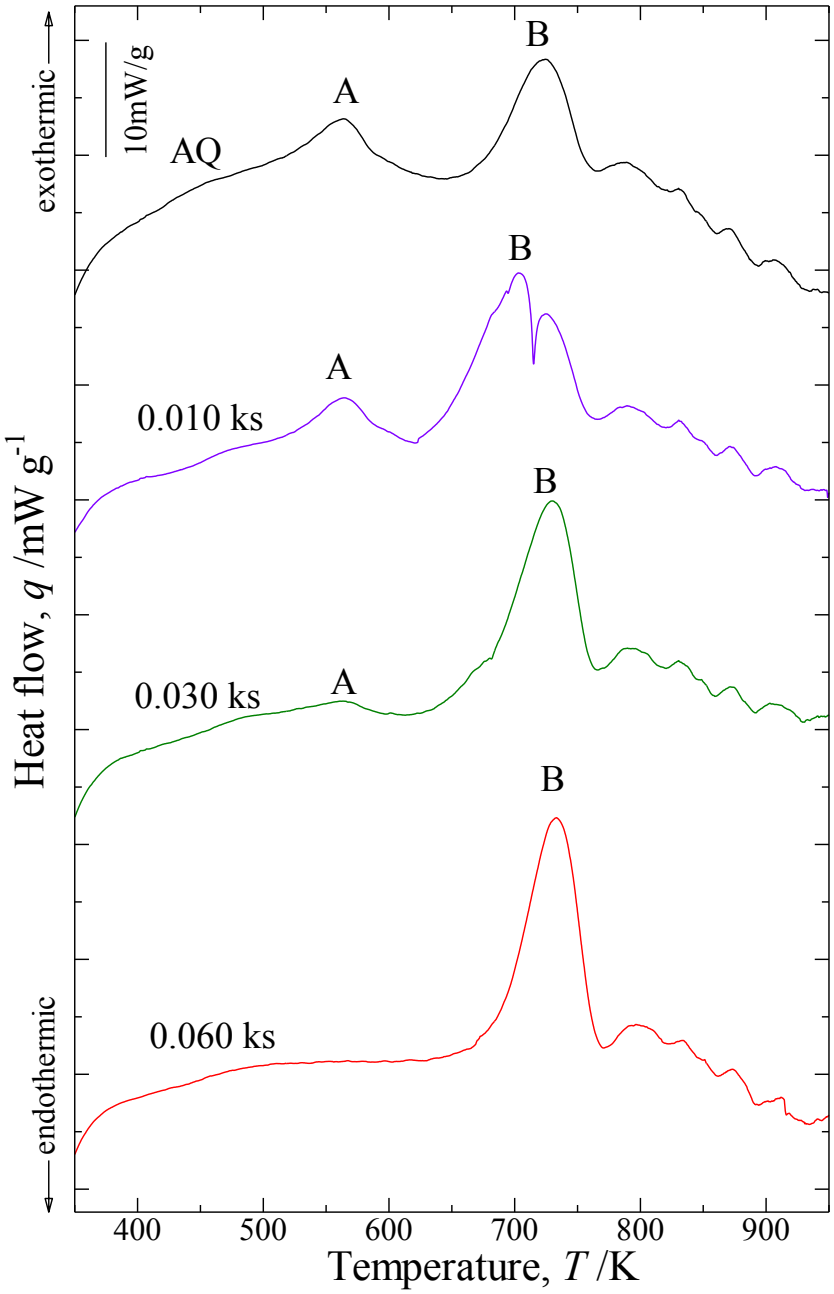

Fig. 2.5 DSC curves of the 1123-600 specimen aged at 573 K.

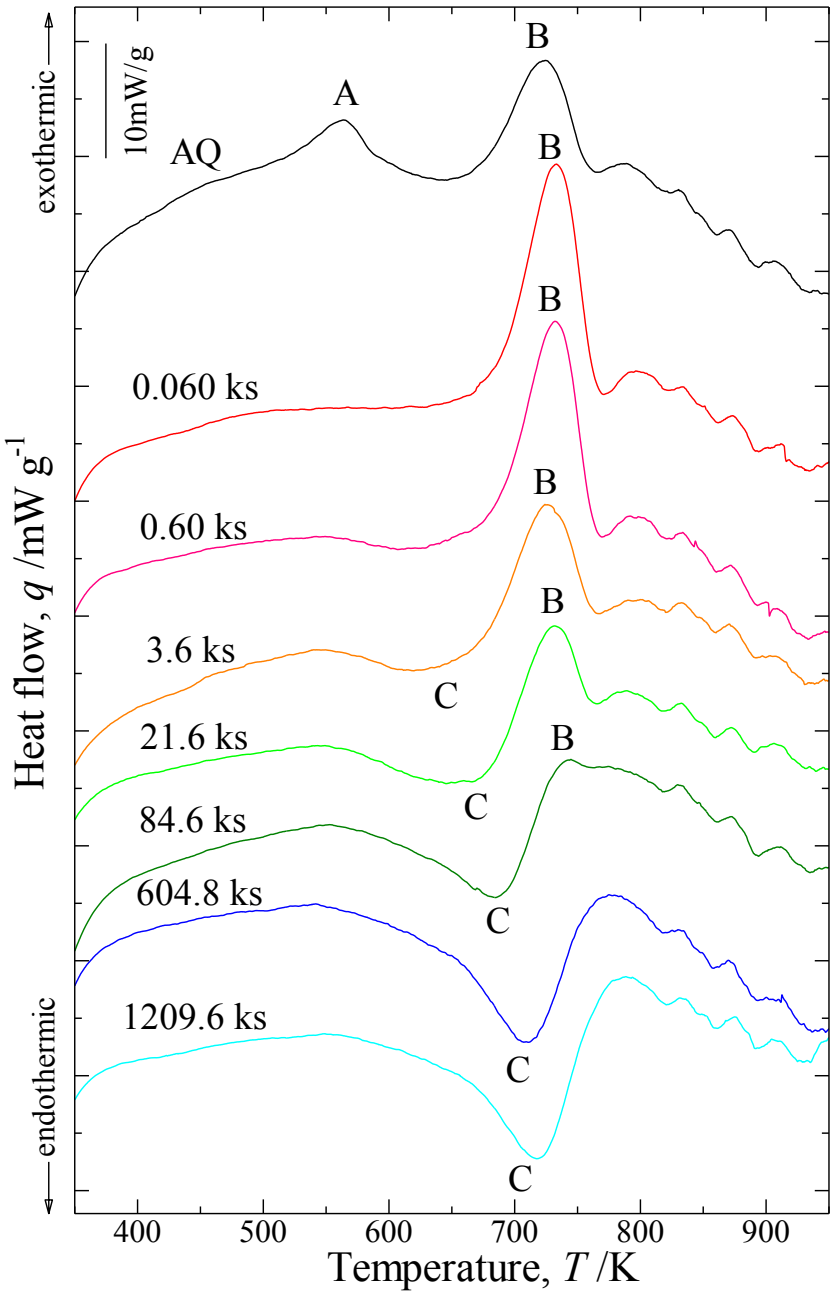

Fig. 2.5 Continued.

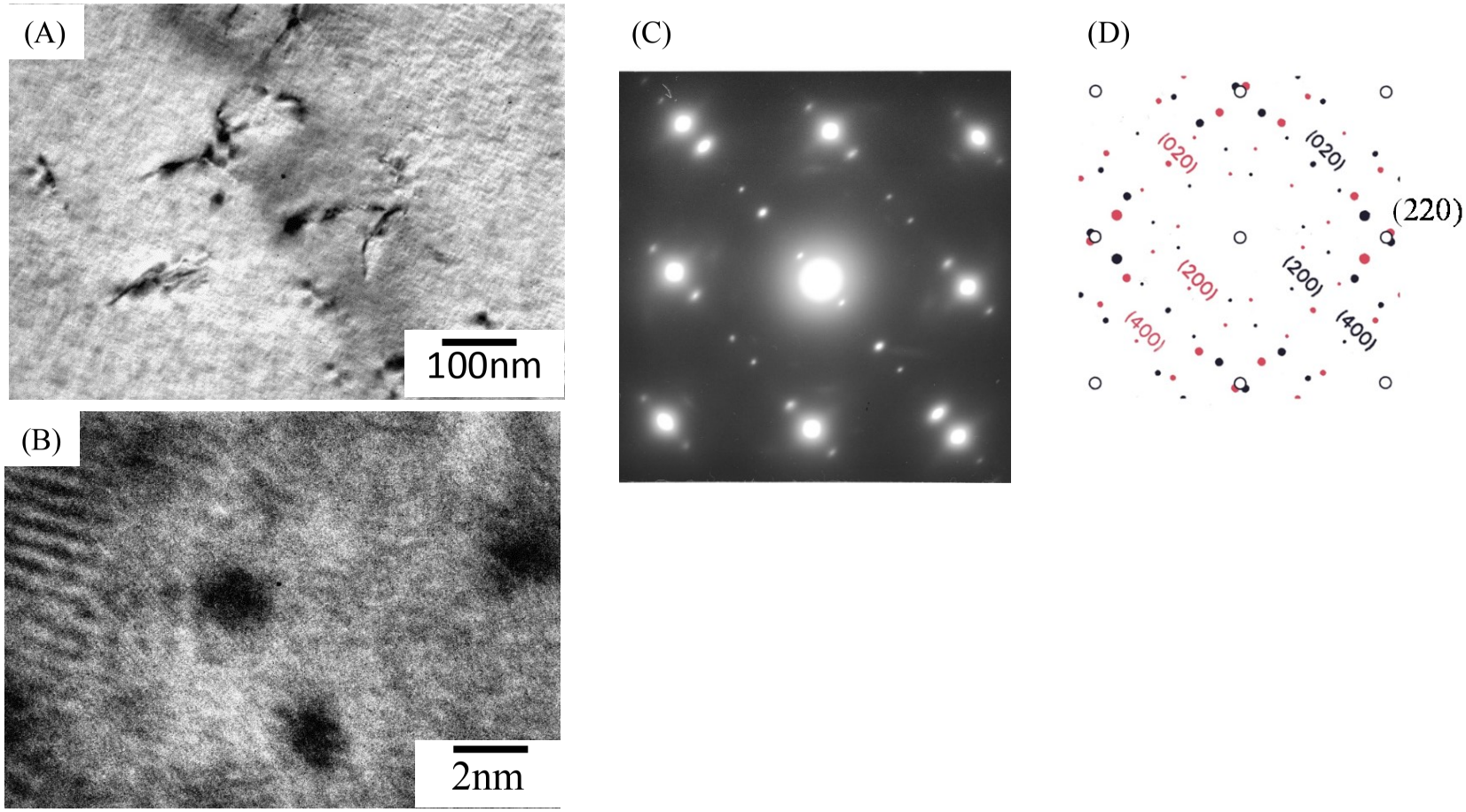

Fig. 2.6 (A) TEM, (B) HRTEM images (C) diffraction pattern of the 1123-600 specimen aged at 573 K for 1209.6 ks. Beam direction is parallel to $[100]_M$. (D) Calculated diffraction pattern for δ-Ni_2Si phase.

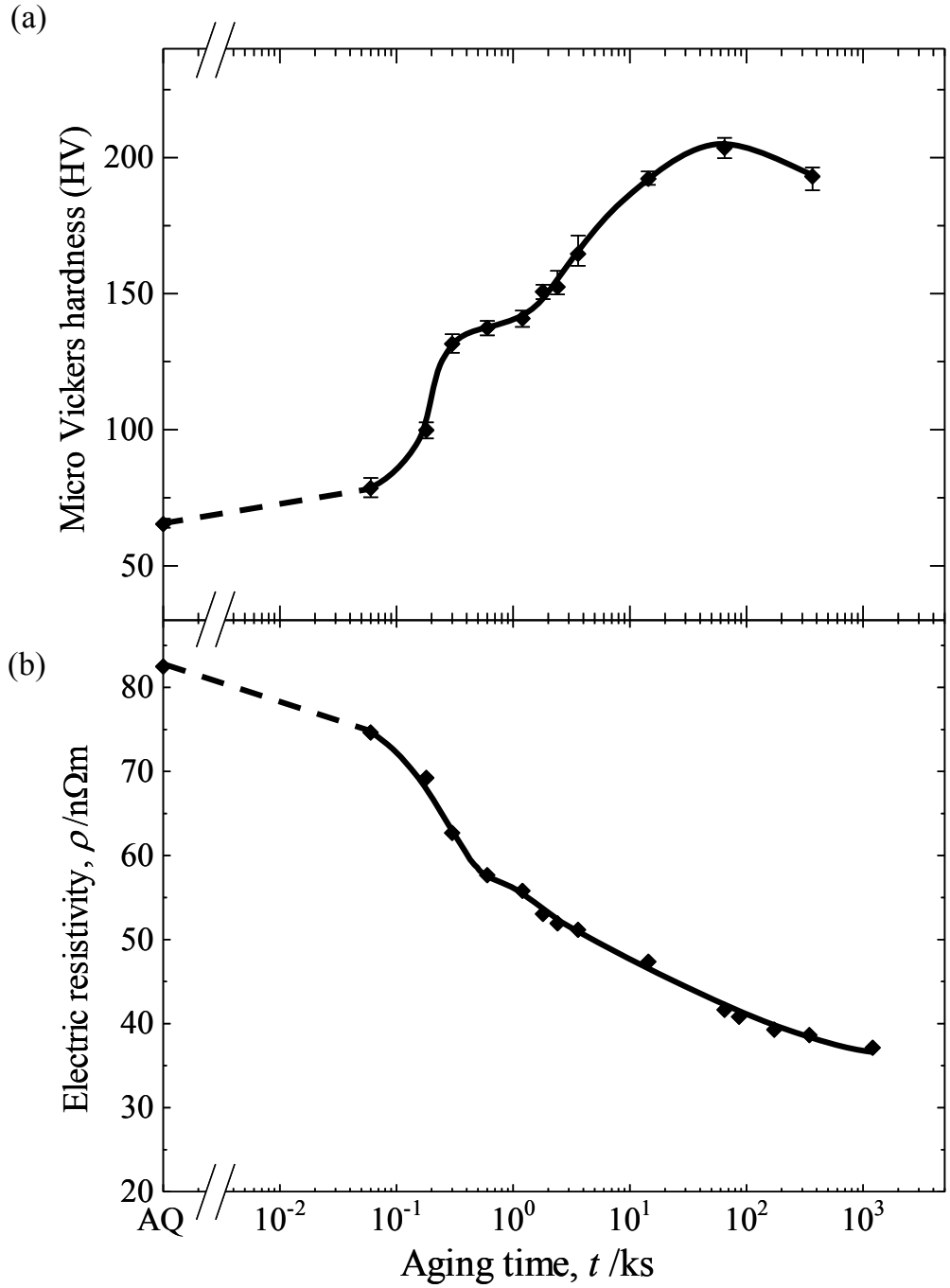

Fig. 2.7 (a) Micro Vickers hardness and (b) electrical resistivity of the 1123-600 aged at 723 K.

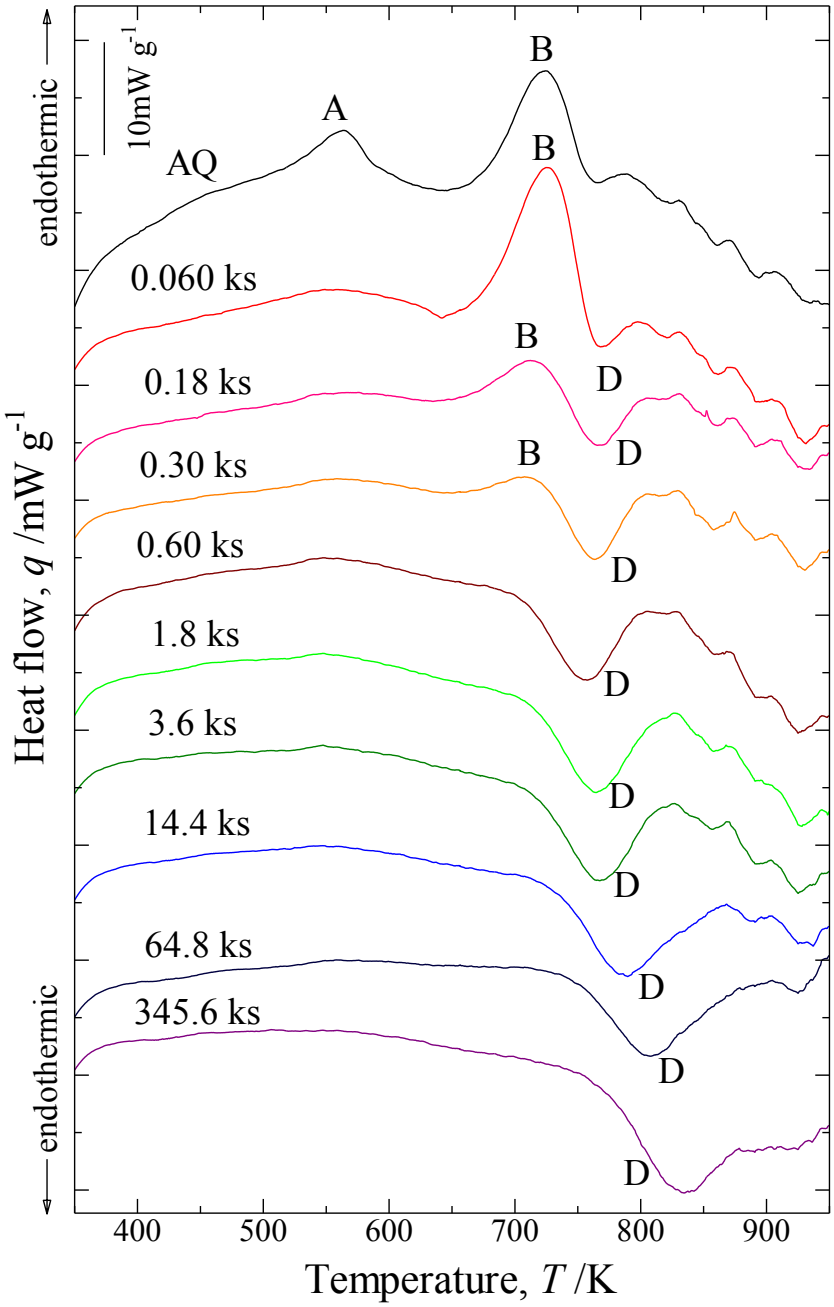

Fig. 2.8 DSC curves of the 1123-600 specimen aged at 723 K.

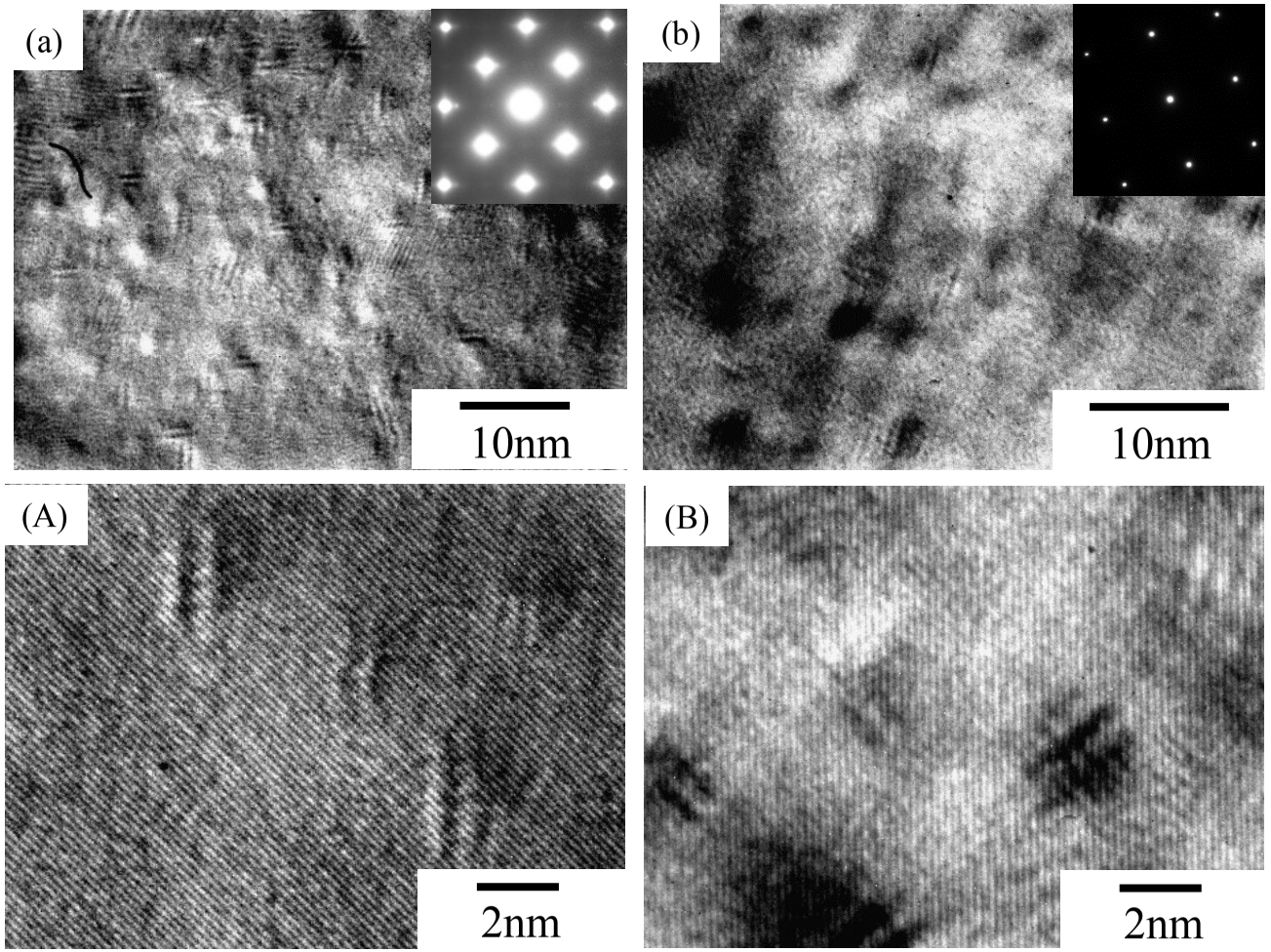

Fig. 2.9 High resolution TEM images of the 1123-600 specimen at 723K for (a) 0.30 ks, (b) 0.60 ks, (c) 3.6 ks, (d) 14.4 ks, (e) 64.8 ks and (f) 345.6 ks. Higher magnification for corresponding (a) – (f) are shown in (A) – (F). Beam direction is parallel to $[100]_M$.

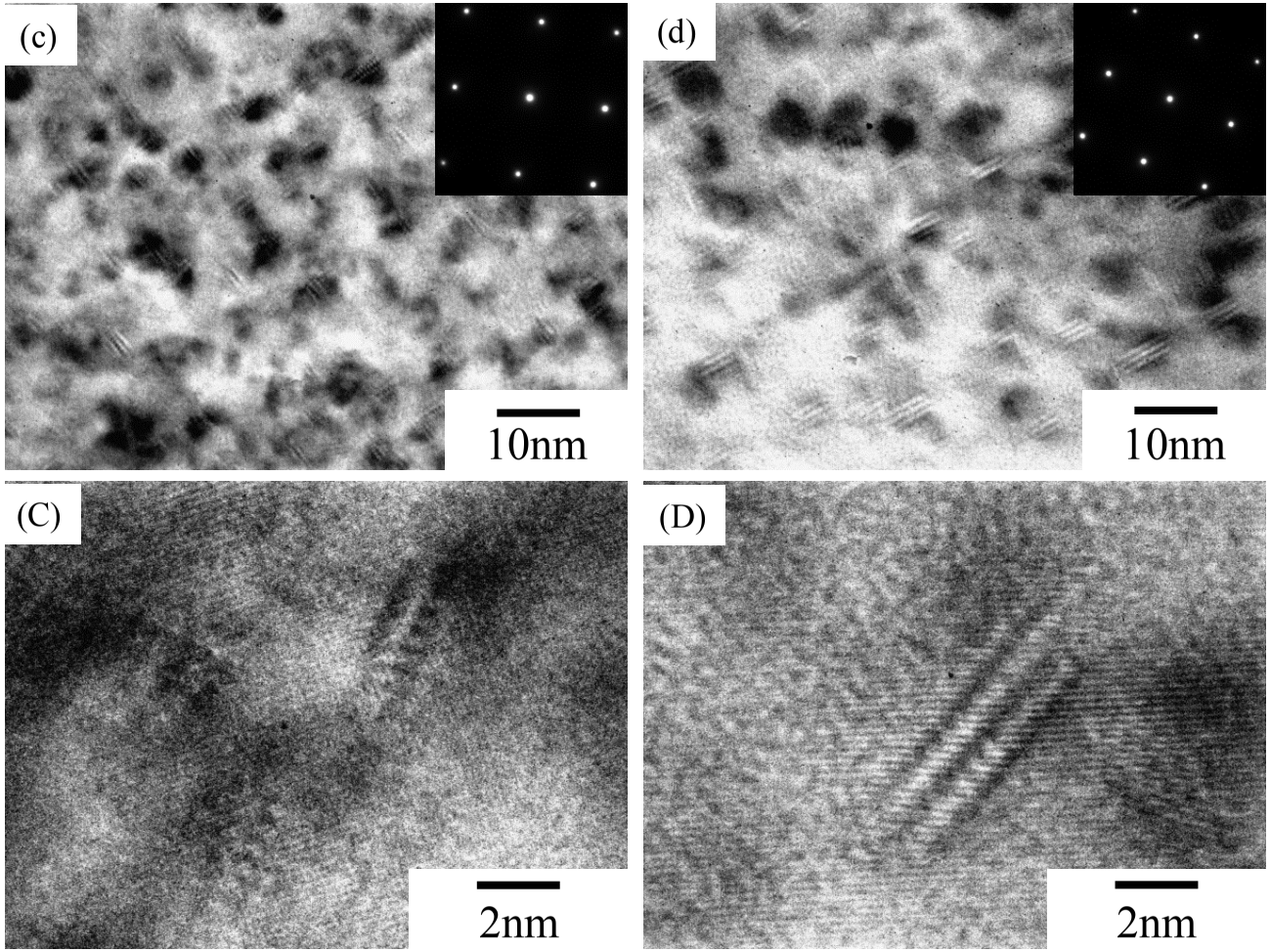

Fig. 2.9 Continued.

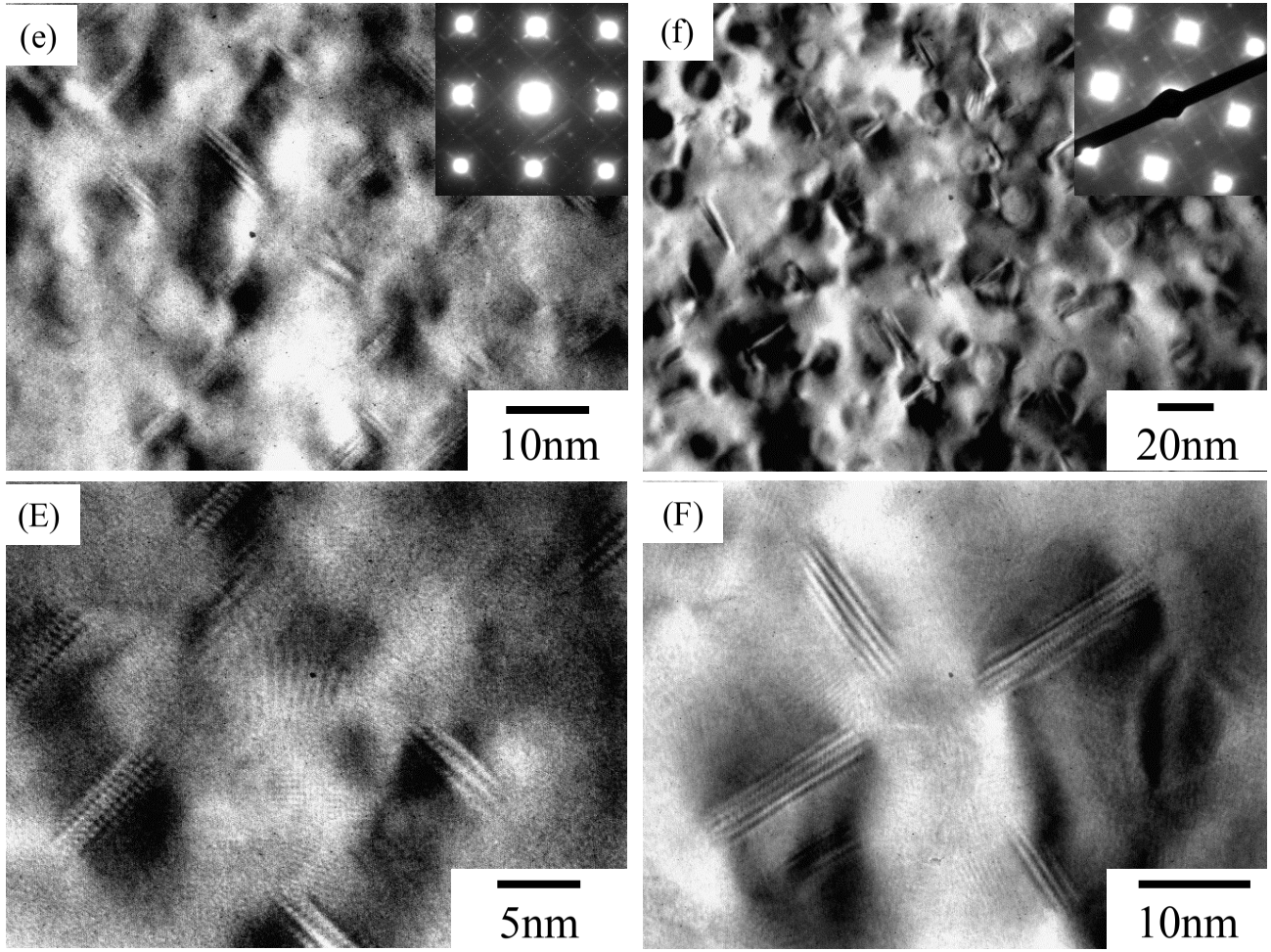

Fig. 2.9 Continued.

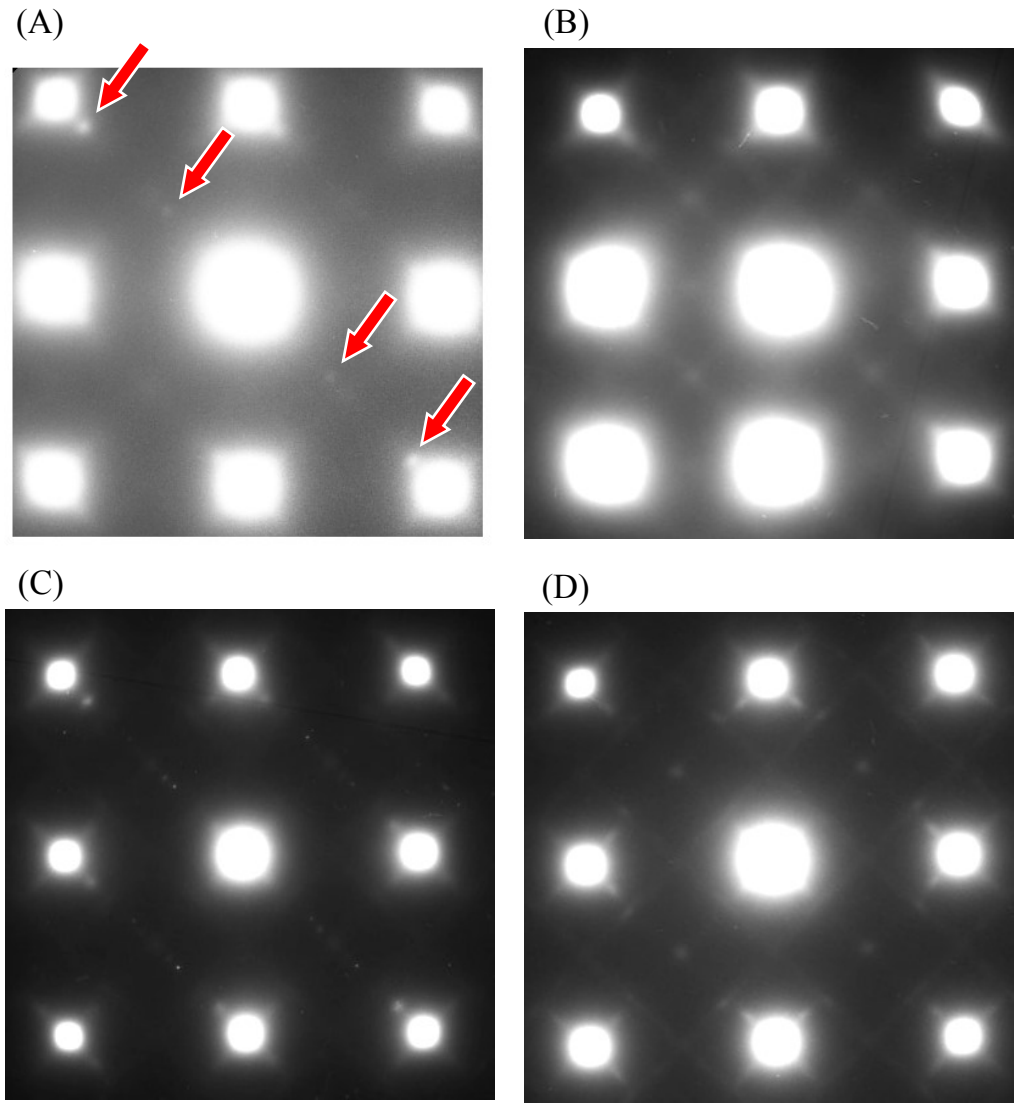

Fig. 2.10 Diffraction patterns of the 1123-600 specimen aged at 723K for (A)0.30ks, (B) 0.60ks, (C) 3.6ks, (D) 14.4ks, (E) 64.8ks, (F) 345.6ks and (G) the calculated diffraction pattern for δ-Ni_2Si. Beam direction is parallel to $[100]_M$.

(E)

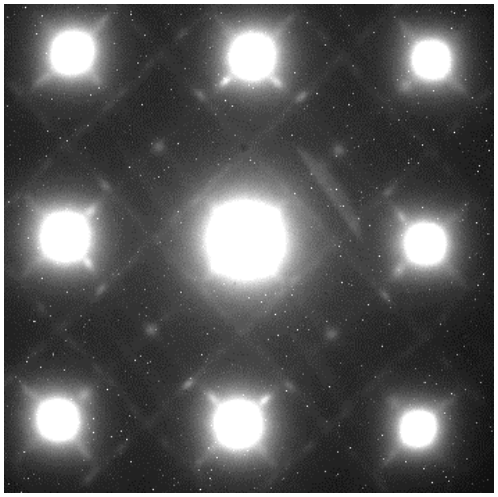

(F)

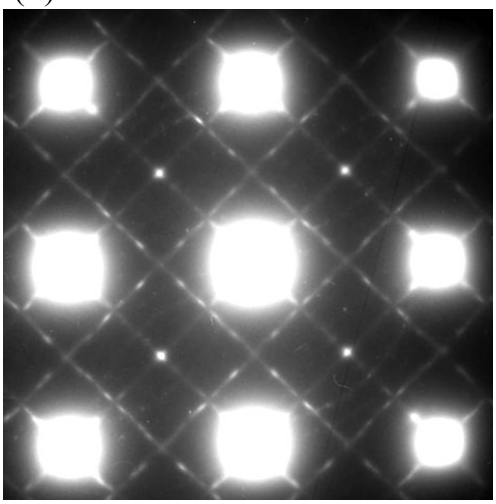

(G)

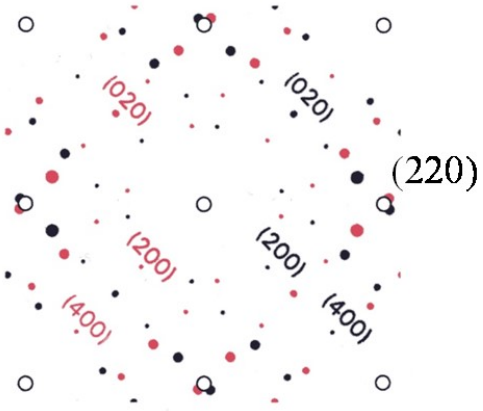

Fig. 2.10 Continued.

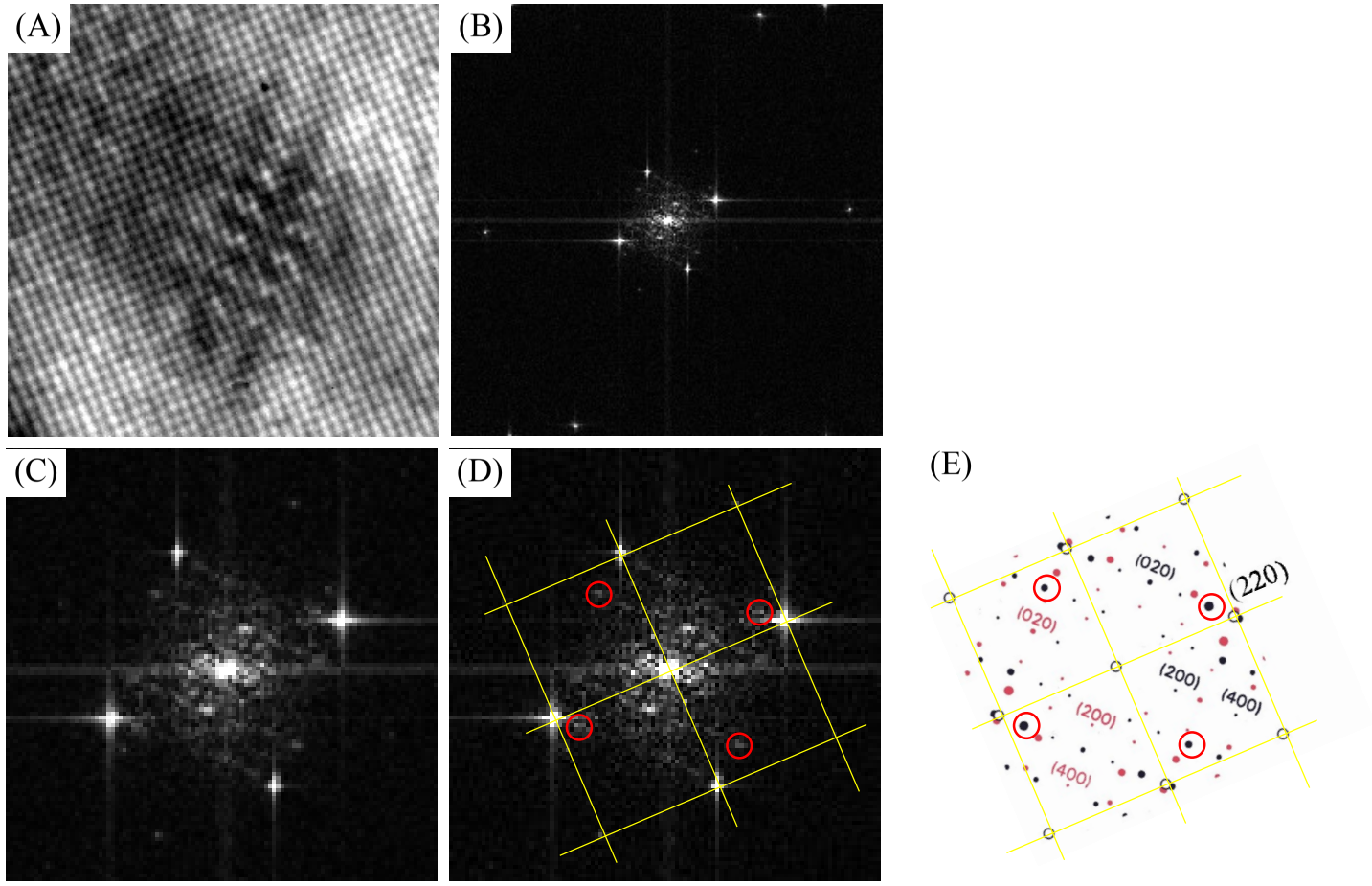

Fig. 2.11 (A) High resolution TEM image of the 1123-600 specimen aged at 723K for 0.60ks, (B) FFT pattern of (A), (C) and (D) enlarged image of (B) amd (E) the calculated diffraction pattern for δ-Ni_2Si.

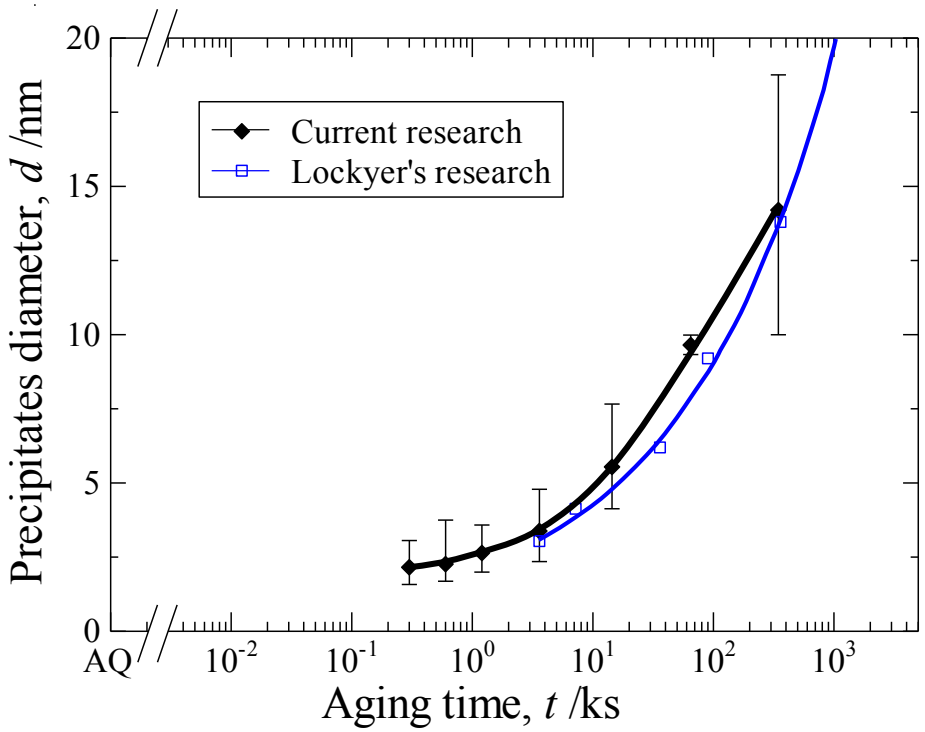

Fig. 2.12 Average precipitate diameter of the 1123-600 specimen aged at 723 K.

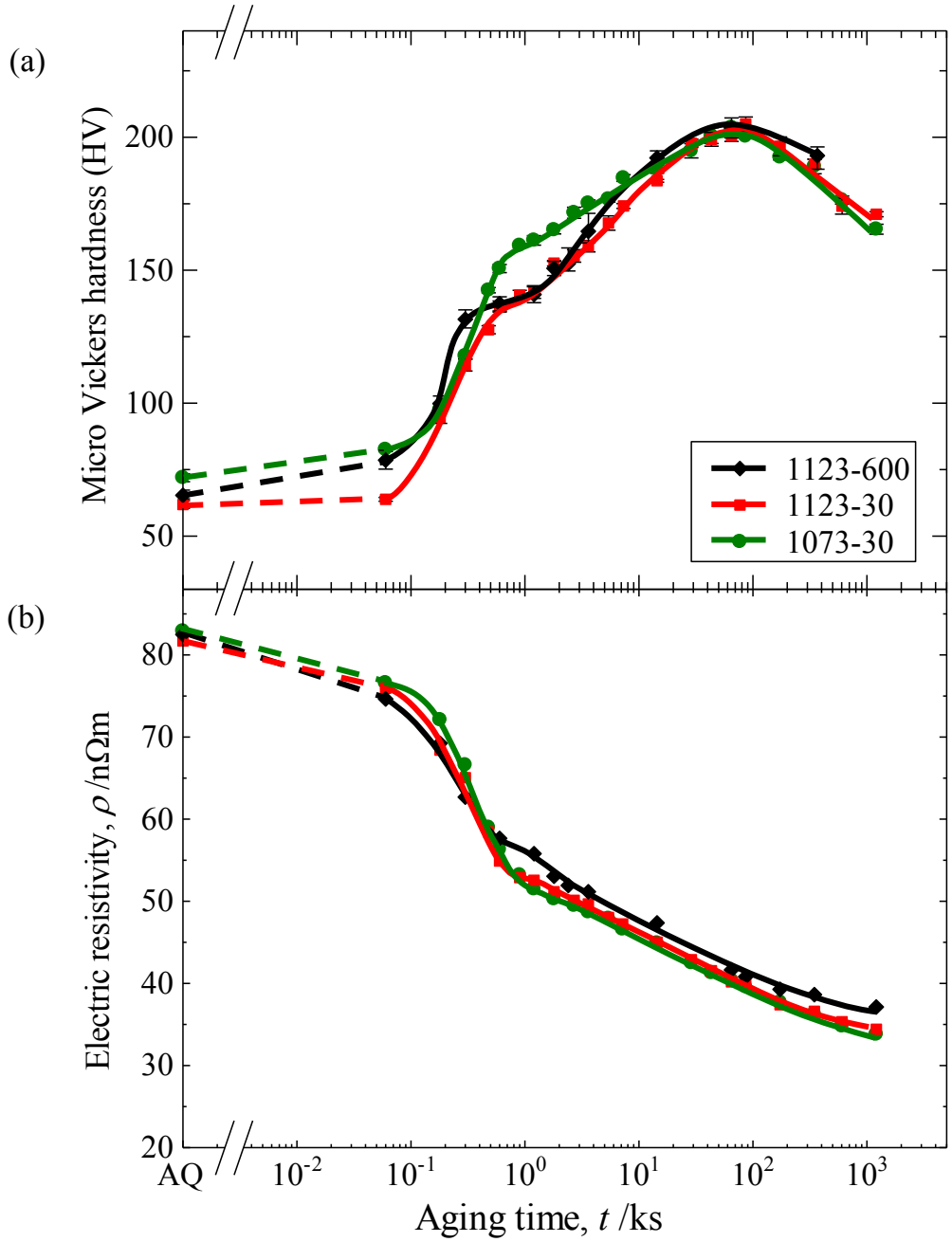

Fig. 2.13 (a) Micro Vickers hardness and (b) electrical resistivity of the Cu-Ni-Si alloy aged at 723K with the various solution treatment conditions.

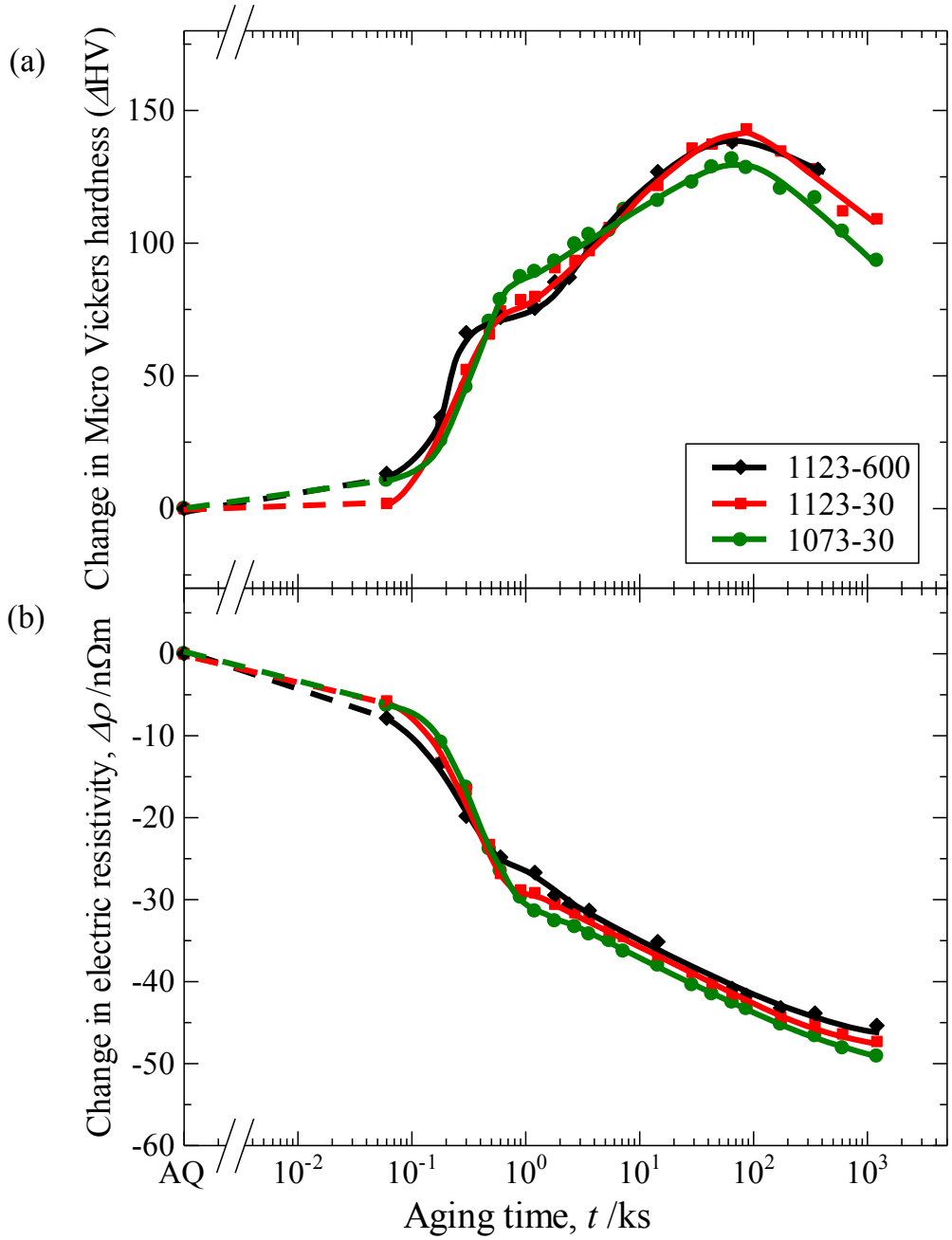

Fig. 2.14 Changes in (a) Micro Vickers hardness and (b) electrical resistivity of the Cu-Ni-Si alloy aged at 723K with the various solution treatment conditions.

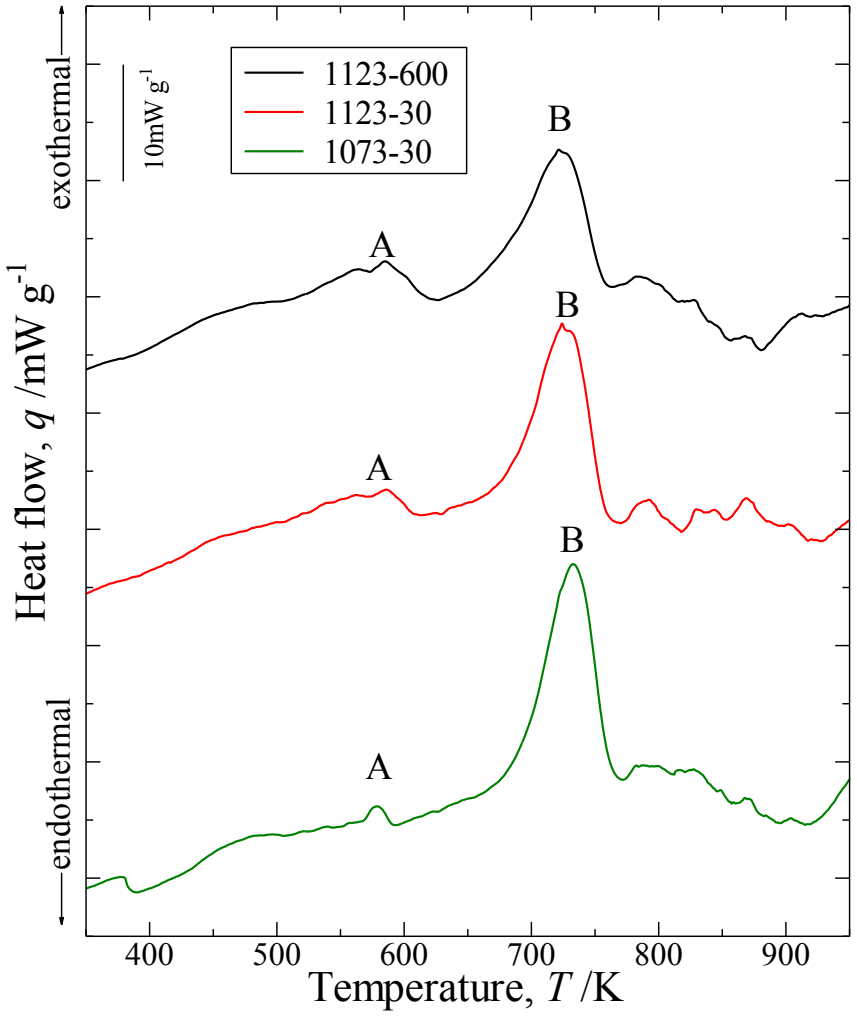

Fig. 2.15 DSC curves for the Cu-Ni-Si alloys with various solution treatment conditions.

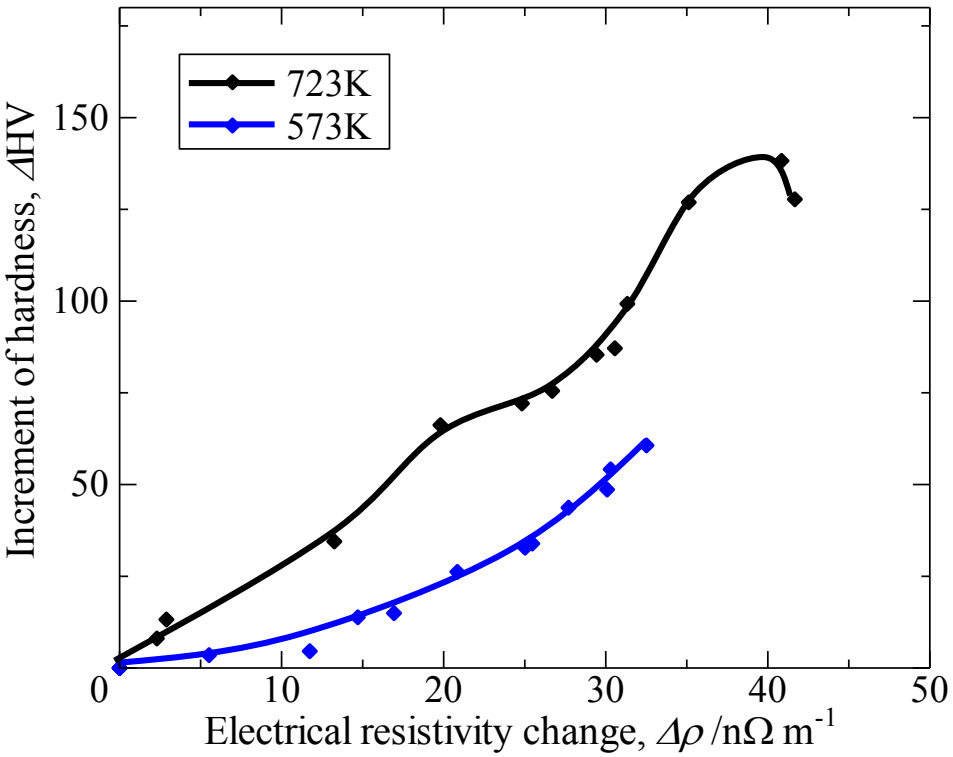

Fig. 2.16 The relation between the increment of the hardness as a function of the change of the electrical resistivity in the 1123-600 specimen at each aging temperature.

Table 2.4 The contribution to specific resistivity per mole percentage of various solute elements in Cu.

Solute elements, *i*	Ni	Si	Sn	Zn	Mg
$\Delta\rho^i$ (nm·m/mol%)	12.5	39.5	6.5	3.2	28.8

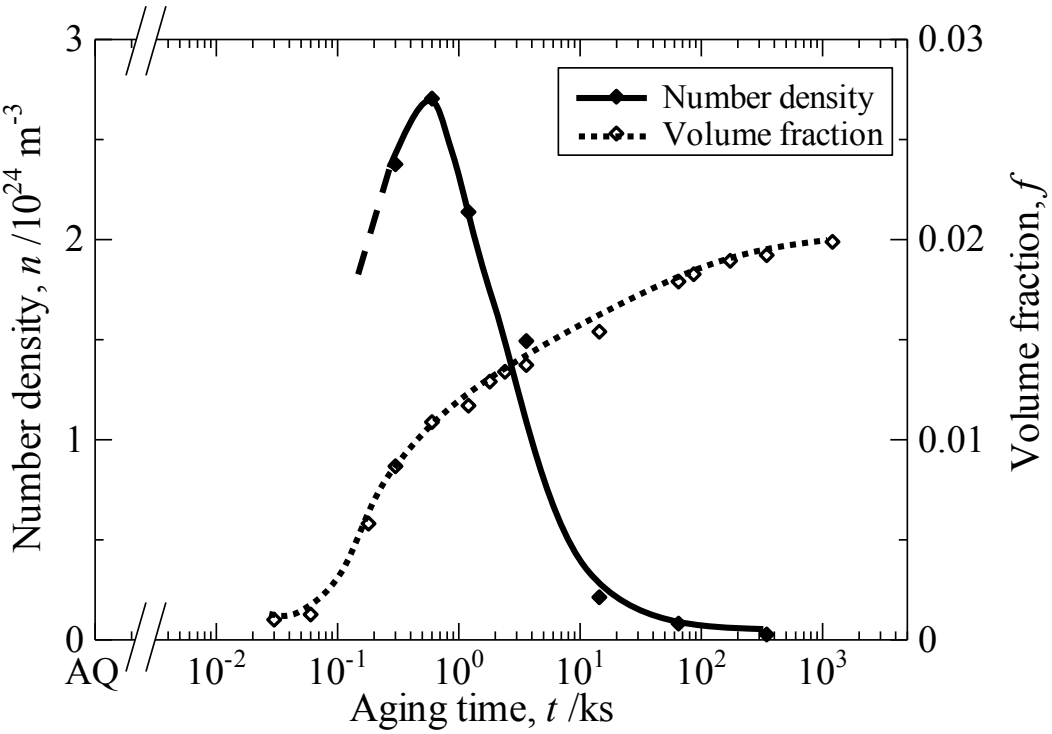

Fig. 2.17 Number density and volume fraction of the precipitate as a function of aging time in the 1123-600 specimen aged at 723 K.

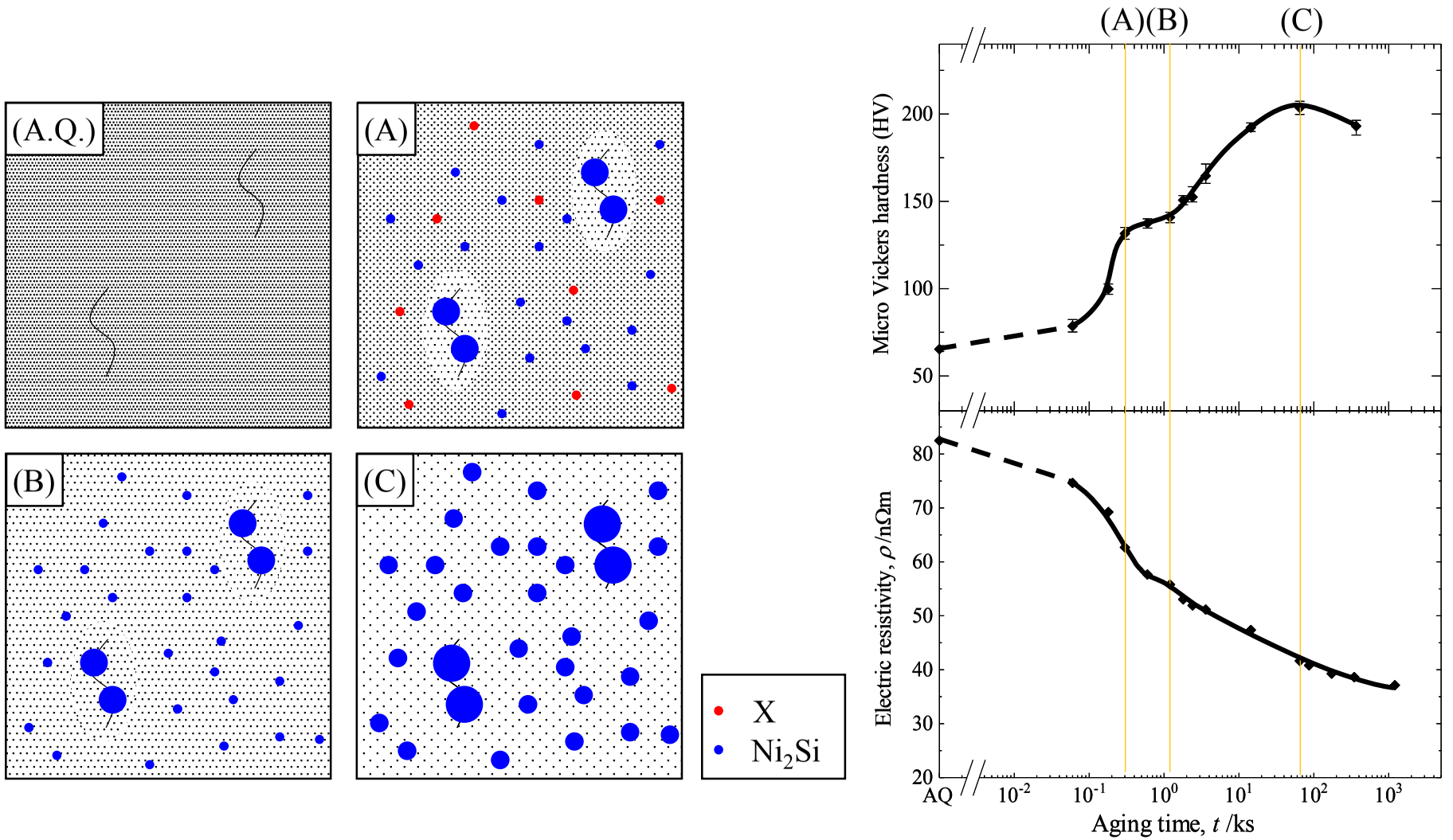

Fig. 2.18 Schematic illustrations of the sequence of precipitation in the 1123-600 specimen aged at 723K.

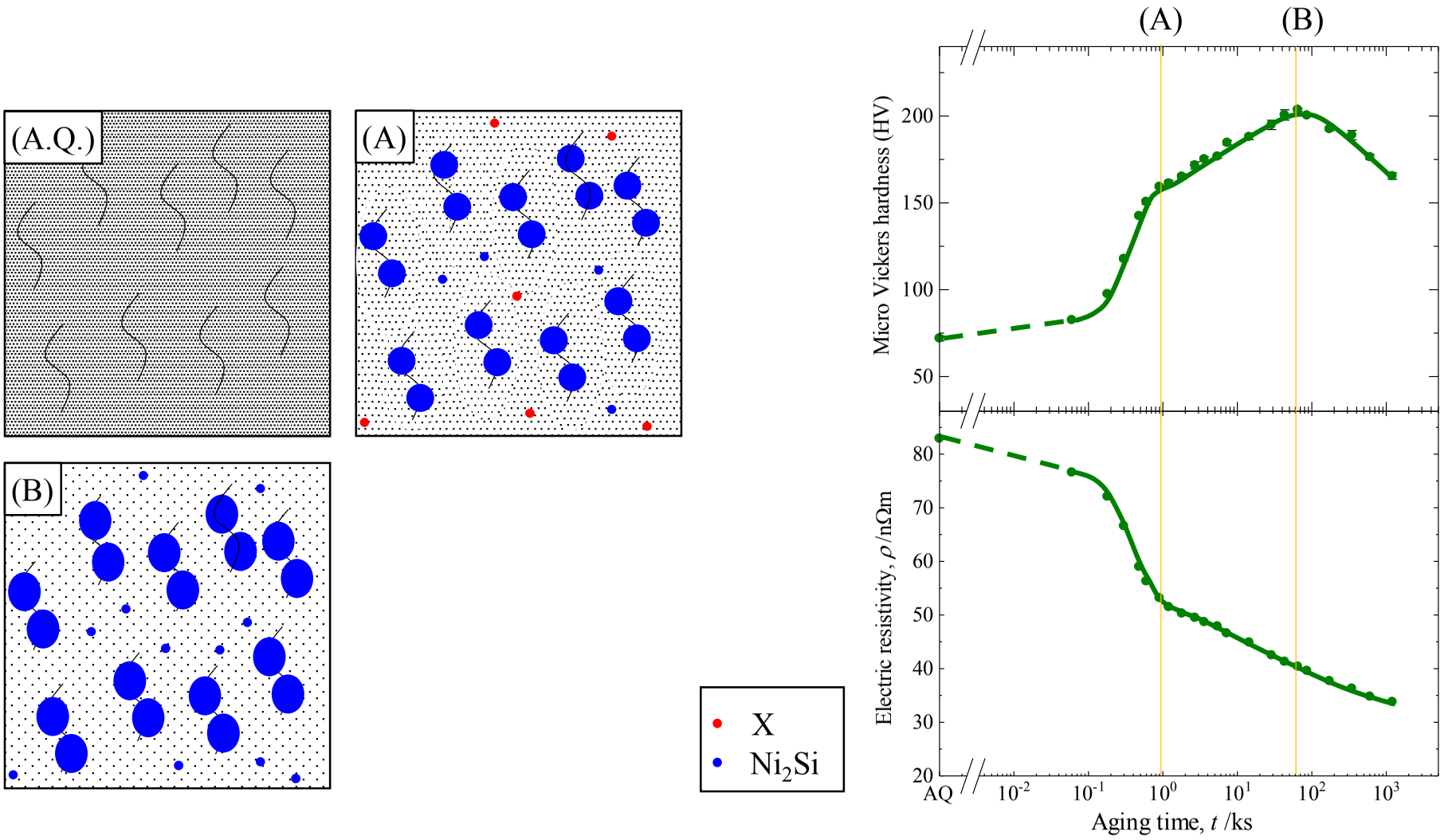

Fig. 2.19 Schematic illustrations of the sequence of precipitation in the 1073-30 specimen aged at 723 K.

Chapter 3

Work hardening behavior in Cu-Ni-Si alloy

3.1. Introduction

It was shown that the δ-Ni_2Si is the main precipitating phase during the aging at 723 K. In industrial processes, the alloy is cold worked after aging treatment to obtain thinner materials. However, no detailed report exists regarding the work hardening behavior of the Cu-Ni-Si alloys. It is well known that both the yield strength and the work hardening behavior of precipitation strengthened alloys are significantly affected by the nature of interaction between precipitates and dislocations. To clarify the interaction between the precipitates and dislocations is, therefore, necessary for the understanding of the work hardening behavior, and to obtain high strength material.

The relationship between the presence of precipitates and the work hardening behavior has shown for the first time by Blankenship *et al.* [1]. Cheng *et al.* [2] have rationalized the influence of precipitates on the work hardening behavior in an AA6111 aluminum alloy on the basis of whether precipitates are sheared by mobile dislocations or not and how this affects dislocation accumulation and dynamic recovery. Poole *et al.* [3] focused on determining the transition point from shearable to non-shearable precipitates by dealing with both microstructure and work hardening behavior. They have shown that the work hardening behavior significantly changes by the transition.

It is known that the Bauschinger effect is also affected by the interaction between the obstacles and dislocations because the Bauschinger effect is also caused by the dislocation accumulation. The analysis for the Bauschinger effect is usually interrupted in terms of polarization of internal stress due to the accumulation of dislocations during plastic deformation. In the case of materials containing second-phase particles, the Bauschinger effect becomes significant due to the pile up of dislocations on the particle.

The objective in this chapter is, therefore, to clarify the work hardening behavior and the interaction between the precipitates and dislocations in the Cu-Ni-Si alloy having a variety of precipitate distributions.

3.2. Experimental procedure

The chemical composition of the specimen is given in Table 2.1. The specimens were solution heat treated with various solution heat treatment summarized in Table 2.2, then aged in a salt bath at 723 K for various times.

The tensile test was conducted at room temperature at a nominal strain rate of 2×10^{-3} s^{-1} using an Instron screw-driven tensile machine for the specimen aged for various times. The strain was measured in the reduced section of the specimens using a clip-on extensometer with a 25.4 mm gauge length. The work hardening rate was determined by differentiating the true stress-true strain data.

In order to investigate the deformed microstructures, transmission electron microscopy (TEM) was carried out using a JEOL JEM-3010 transmission electron microscope operating at 300 kV on specimens aged for various times and deformed by 10 % in tension at room temperature.

In order to investigate the Bauschinger effect, the cylindrical specimen was obtained by reducing the cold rolling process in Fig. 2.1. The aging treatment at 723 K was done to the specimen solution treated at 1123 K for 600 s. The average grain size of the specimen was about 210 μm. The cylindrical specimen with the diameter in deduced area of 5 mm is finally obtained from the aged specimen. The tensile and tension-compression test was conducted on a computer controlled MTS servo-hydraulic machine with a nominal strain rate of 1×10^{-3} s^{-1}. The tension-compression test was conducted as following way. First, the specimen was deformed by 2 % in tension. The strain was then reversed to apply compression strain so that the reverse strain was over 1 %.

3.3. Result

3.3.1. Work hardening behavior in Cu-Ni-Si alloy with various conditions of solution heat treatment

The true stress – true strain curves and corresponding Kocks-Mecking plots, which is the change of the work hardening rate, $\Theta \equiv d\sigma/d\varepsilon$, as a function of the flow stress, σ, of the specimens aged at 723 K for various times are shown in **Fig. 3.1**. A curve for the oxygen free high conductivity (OFHC) copper (99.99 % purity) with the similar grain size with the specimen is also shown in Fig.

3.1. Both the work hardening rate and flow stress are normalized by the shear modulus of pure copper at room temperature. The dotted line in the Kocks-Mecking plots shows the Considére criterion indicating the limitation of uniform deformation. It is obvious that the work hardening behavior is significantly affected by both the aging condition and the solution treatment condition.

3.3.2. Bauschinger effect change in Cu-Ni-Si alloy during aging at 723 K

Fig. 3.2 illustrates the way of analysis to obtain the Bauschinger effect. First, the true stress vs. true strain curve is plotted. Then the compressive data is reversed and plotted as a function of cumulative strain and finally the true stress vs. cumulative true strain is compared to the monotonic behavior. **Fig. 3.3** shows the forward–reverse behavior obtained for different heat treatments after 2 % plastic strain applied in the forward direction. The tension-compression behavior changed as aging progressed. For the specimens until 3.6 ks of aging, the flow stress quickly comes back to the stress reached during the forward straining. On the other hand, for the specimens aged 3.6 ks, longer strain is needed to get back the forward stress.

3.4. Discussion

3.4.1. Transition from shearable to non-shearable precipitate in Cu-Ni-Si alloy

In this work, two parameters are defined in order to characterize the work hardening behavior of the specimens. The first parameter is Θ_{initial} and it is defined as the initial work hardening rate in the plastic regime. In this study, it is defined as the work hardening rate at the strain of 0.02 as shown in **Fig. 3.4**,

$$\Theta_{\text{initial}} = \left.\frac{d\sigma_{\text{t}}}{d\varepsilon_{\text{t}}}\right|_{\varepsilon_{\text{p}}=0.02} \tag{3.1}$$

The theoretical work for the development of constitutive laws for alloys containing shearable and non-shearable particles has been reviewed by Estrin [4]. The evolution equation for the dislocation density with plastic strain is written as

$$\frac{d\rho}{d\varepsilon^{\text{p}}} = M\left(k_1\sqrt{\rho} - fk_2\rho + k_D\right) \tag{3.2}$$

where M is the Taylor factor (3.06 for fcc metals), ρ is the dislocation density, ε^p is the plastic strain, and k_1 and k_2 are constants. The first term on the right side of Eq. (3.1) represents the dislocation storage term due to trapping of dislocations by other dislocations. The second term represents the dynamic recovery term and f represents a modifying factor due to the effect of dislocation/particle interactions on dynamic recovery. The last term represents due to the storage of geometrically necessary dislocations due to non-shearable particles. The value of k_D depends on the interaction between the particle and dislocation, i.e. in the case of shearable precipitates,

$$k_D = 0 \tag{3.3}$$

and when the particle is non-shearable

$$k_D = \frac{\alpha_D}{bL} \tag{3.4}$$

where b is the magnitude of the Burgers vector (2.56×10^{-10}nm for copper), L is the spacing of the particles on the glide plane, which can be estimated from the number density and average size of the precipitate obtained in Chapter 2, and α_D is a constant and the value is 0.3[2]. The flow stress contribution from dislocation hardening, $\sigma_\perp$, can be expressed as

$$\sigma_\perp = M\alpha\mu b\sqrt{\rho} \tag{3.5}$$

where $\alpha_\perp$ is a constant of 0.3, M is the Taylor factor, μ is the shear modulus of matrix (42.1 GPa for copper at room temperature), b is the magnitude of the Burgers vector and ρ is the dislocation density.

In addition, Cheng *et al.* [2] proposed the flow stress addition law to account for different ways of summing the precipitation and dislocation hardening contributions, i.e.,

$$\sigma = \sigma_{SS} + \left({\sigma_\perp}^n + {\sigma_{ppt}}^n\right)^{1/n} \tag{3.6}$$

where n can vary between 1 and 2, and σ_{ss} is the contribution from the solid solution and σ_{ppt} is the contribution from the precipitation hardening contribution. The computer simulations of Foreman and Makin [5] suggest that the case of $n = 1$ is applied when there is a high density of weak obstacles and a low density of strong obstacles. This would correspond to the early stage of aging in this work when there is a high number density of small precipitates. On the other hand, a value of n =2 would be appropriate when there is a high density of strong obstacles, corresponding the later stages

of aging in this work. At intermediate cases, the appropriate value of n is between 1 and 2.

The work hardening rate, Θ is derived from the Eq. (3.6),

$$\Theta = \left(\frac{{\sigma_\perp}^n}{{\sigma_\perp}^n + {\sigma_{\text{ppt}}}^n}\right)^{1-\frac{1}{n}} \left(\frac{M\alpha\mu b k_1}{2} - \frac{f k_2}{2}\sigma_\perp + \frac{(M\alpha\mu b)^2 k_D}{2\sigma_\perp}\right) \tag{3.7}$$

For the case that the specimen contains no precipitate, n = 1, σ_{ppt} is zero and k_D is also equal to zero, the well-known Voce's law is given,

$$\Theta = \left(\frac{M\alpha\mu b k_1}{2} - \frac{f k_2}{2}\sigma\right) \tag{3.8}$$

This is the case for pure copper and as-solution-treated specimen in this work. The reasonable values for k_1 and k_2 have been chosen by fitting to the Kocks-Mecking plots for the pure copper and as-solution-treated condition, 4.4×10^8 m^{-1} for k_1 and 13 for k_2.

Without the work hardening, the dislocation density in the specimen has the order of 10^{10} m^{-2}. This gives the value of the dislocation hardening contribution, $\sigma_\perp$ of about 1 MPa. The initial work hardening rate, Θ_{initial} now can be described as

$$\Theta_{\text{initial}} = \left(\frac{1}{1 + {\sigma_{\text{ppt}}}^n}\right)^{1-\frac{1}{n}} \left(\frac{M\alpha\mu b k_1}{2} - \frac{f k_2}{2} \times 10^6 + \frac{(M\alpha\mu b)^2 k_D}{2 \times 10^6}\right) \tag{3.9}$$

where the σ_{ppt} should have the unit of MPa. The first term in the second parentheses of the right side has the order of 10^9 and the second term has the order of 10^7. The last term depends on the precipitate state as given by Eq. (3.3) and (3.4), the value has the order of 10^{12} at peak aged condition when the precipitates have been considered as non-shearable. The contribution of the dynamic recovery term to the initial work hardening rate is now neglectable compared to the dislocation accumulation term. The value of σ_{ppt}, n and k_D change as the aging proceeds. The magnitude of the first parentheses $\left(\frac{1}{1+{\sigma_{\text{ppt}}}^n}\right)^{1-\frac{1}{n}}$ increases in under-aged condition, when the σ_{ppt} increases monotonically until peak-aged condition. On the other hand, the magnitude of the second parentheses $\left(\frac{M\alpha\mu\mathbf{b}k_1}{2} - \frac{f k_2}{2} \times 10^6 + \frac{M\alpha\mu\mathbf{b}k_D}{2\times10^6}\right)$ does not change when the precipitates are shearable, but drastically increase due to the contribution of the dislocation accumulation on the precipitates when the precipitates became non-shearable.

The second parameter is $d\Theta/d\sigma$ and it is defined as the slope of the Kocks-Mecking plot as proposed by Cheng et al [2]. For the samples with a nonlinear behavior, the slope is taken from near the rupture point of the plot as shown in **Fig. 3.5**. Cheng et al. proposed the parameter $-d\Theta/d\sigma$ which is related to the dynamic recovery rate, to characterize the work hardening behavior.

The variation of $\Theta_{initial}$ and $-d\Theta/d\sigma$ as a function of aging time for the specimens with various solution treatment conditions are shown in **Fig.3.6** and **Fig. 3.7**, respectively. Both the variation of the initial work hardening rate and the value of $-d\Theta/d\sigma$ were different among the specimens. The initial work hardening rate is almost constant until 3.6 ks aging in the 1123-600 specimen, on the other hand it increase from 0.30 ks aging in the 1073-30 specimen.

As discussed in section 3.4.1, the increase of the initial work hardening rate before the peak strength is the result of the shearable/non-shearable transition. It is obvious, therefore, that the shearable/non-shearable transition starts at the aging time of 0.60 ks in the 1123-600 specimen, 0.30 ks in the 1123-30 specimen and 0.060 ks in the 1073-30 specimen. Thus, the shearable/non-shearable transition time becomes shorter as the dislocation density becomes high. The shearable/non-shearable transition is related to both the precipitate size and the spacing between the precipitates. As discussed in Chapter 2, this is because the δ-Ni_2Si precipitates preferentially forms on the dislocations and the precipitates on the dislocations can grow earlier than the ones in the matrix. The higher dislocation density is in the specimen, therefore, the shorter aging time becomes for the shearable/non-shearable transition.

On the other hand, it is difficult to determine the shearable/non-shearable transition time on the basis of the variation of $-d\Theta/d\sigma$, especially in the 1123-600 and 1123-30 specimens. The variation of $-d\Theta/d\sigma$ continue until the peak-aged condition. The appropriateness of the discussion based on the variation of $-d\Theta/d\sigma$ will be discussed in the following section.

Now, **Fig. 3.8** shows the variation of the initial work hardening rate of the 1123-600 specimen aged at 723 K plotted as a function of the average precipitate diameter obtained in Chapter 2. This figure indicates that the shearable/non-shearable transition starts when the precipitate diameter is about 3.5 nm. In addition, from the experimental results for the initial work hardening rate, the value of n in equation (3.6) can be estimated from the equation (3.9). The initial work hardening

rate is constant until the aging time of 3.6 ks. This result indicates that the initial work hardening rate for this aging condition is not affected by the first parenthesis in equation (3.9). Thus, the value of n is estimated as being equal to one, which means the precipitates are shearable. On the other hand, the estimated value for n at the peak-aged condition and over-aged conditions was 1.9 and 2 respectively on the basis of the initial work hardening rate. Thus, it can be estimated that the most of precipitates after the peak-aged condition are non-shearable.

In order to confirm the estimation, the TEM observations were conducted for the 1123-600 specimen aged at 723 K for various times and deformed by 10 % at room temperature. **Fig. 3.9** shows the HRTEM image of the 1123-600 specimen aged at 723 K for 0.60 ks and deformed by 10 % in tension. It looks that fine precipitates are sheared by dislocations as arrowed. **Fig. 3.10** shows the two-beam dark field image for the 1123-600 specimen aged at 723 K for various times and deformed by 10 % in tension. No dislocation loop was observed in the specimen aged for 0.30 ks aged. A few dislocation loops were observed in the 3.6 ks aged specimen and many loops were observed in the 64.8 ks aged specimen. Based on the TEM results, it was confirmed that the precipitates are shearable before 0.60 ks aging and the precipitates are no longer shearable after 3.6 ks aging at 723 K.

3.4.2. Increase of work hardening rate during tensile deformation

It is obvious that the work hardening behavior of the 1123-600 aged at 723 K shows no longer the typical work hardening behavior. In particular, the specimens aged for 0.30 and 3.6 ks show unusual work hardening behavior, i.e. the work hardening rate first increase and then rapidly decrease after the maximum point. The increase of in the work hardening rate is difficult to explain by a simple work hardening mechanism and suggests an increase of additional obstacles to dislocation slip during deformation.

To clarify the mechanism for this work hardening behavior, TEM observation was carried out for the 3.6 ks aged at 723 K and 10 % deformed specimen. The specimen aged for 3.6 ks shown the most remarkable increase in the work hardening rate during deformation and the 10 % deformation consistent with which the specimen shows the maximal work hardening rate. The

TEM images shown in **Fig. 3.11(a)** illustrates that several planar defects can be observed, which had not been found before deformation. **Fig 3.11(b)** shows the high resolution HRTEM image for the planar defect. The selected area diffraction pattern obtained from this region is also shown in Fig. 3.11(b). The HRTEM image and diffraction pattern revealed that the planar defects were twins and the twinning plane was the {111} planes of the matrix. These observations demonstrate that deformation twins form during tensile deformation in the specimen.

In addition, it is found that the deformation twins are with the range of thickness from 1 to 40 nm, which is finer than the twins in observed in TWIP steels studied by Jacques and co-workers[11, 12] but is similar to that observed in Cu-Al alloys[7]. It is believed that the deformation twins act as strong obstacles for the subsequent movement of dislocations as with grain boundaries[13, 14]. Lu et al.[15] have confirmed that the Shockley partial dislocations are left behind at the coherent nanoscale annealing twin boundaries in pure Cu specimen. As such, interactions between dislocations and the deformation twins formed during tensile deformation represent new obstacles to the dislocation slip which can increase the work hardening rate due to the introduction of new obstacles during deformation. From the above observations and discussions, we conclude that the increase of work hardening rate during tensile deformation observed in the under-aged condition is caused by the formation of deformation twins acting as new obstacles to dislocation slip.

It is interesting that only the under-aged specimens show the increase of work hardening rate during deformation corresponding to the formation of deformation twins. Deformation twinning occurs at a critical stress of the order of γ/b, where γ is the stacking fault energy (SFE) and b is the length of the Shockley partial dislocation[7]. In the Cu-Si system, the SFE decreases as silicon concentration increases[16]. According to this, the SFE of the Cu-Ni-Si alloy is the lowest in the as-solution-treated condition and increases as aging progresses due to the decrease of silicon content in the matrix silicon content resulting from the precipitation of δ-Ni_2Si. Based on this argument, the as-solution-treated condition should have the greatest tendency to cause deformation twinning. Fig. 3.1 indicates, however, that no or few deformation twinning occurs in the as-solution-treated condition in comparison to under-aged specimens. We suggest that this is because the applied stress to the as-solution-treated specimen is too low to cause deformation twinning, while by contrast, the

stress is increased on the sample due to the precipitation hardening and deformation twinning is then possible. Thus, deformation twinning in the precipitate containing alloys depends not only on the SFE but also the precipitates state. The effect of the precipitates on the twinning deformation will be discussed in Chapter 6.

Now, the work hardening behavior at high strain is affected by not only the interaction between the precipitates and dislocations, but also the formation of nano twins and the interaction between the dislocations and nano twins. Therefore, the study based on the analysis of the second parameter, $-d\Theta/d\sigma$ is not appropriate in this work. While, the study based on the initial work hardening rate is still useful because only a few deformation twins have been observed in the specimens deformed by 2 %.

3.4.3. Variation of Bauschinger effect for Cu-Ni-Si alloy during aging at 723 K

When we consider that the flow stress on initial straining is given by the simple linear sum of three terms, the initial flow stress σ_0, the contribution of work hardening which is non-directional, and a component which has the character of an internal stress and is directional, σ_b, the forward stress, σ_{for} required for further forward strain could be written as [6],

$$\sigma_{for} = \sigma_0 + \sigma_S + \sigma_b \tag{3.10}$$

The contribution σ_0 is the initial yield stress of the material including the matrix friction stress, solid solution hardening and precipitation hardening. The contribution σ_0 and σ_S are both considered to be unpolarized contributions to the flow stress so that they oppose deformation in both the forward and reverse senses to the same degree. The term σ_b is the long range back stress, in the sense of the mean stress in the matrix as described by Brown and Clarke [7].

The flow stress in the reverse sense, σ_{rev} after the forward prestrain is given by simply reversing the sign of the directional stress, thus,

$$\sigma_{rev} = \sigma_0 + \sigma_S - \sigma_b \tag{3.11}$$

because the component σ_b opposes the continued deformation in the forward sense, but it aids deformation in the reverse sense. From the above two equations, the internal stress σ_b is given by

In this work, the forward stress is obtained as the tensile stress at the forward strain is 0.03, and

$$\sigma_b = \frac{\sigma_{for} - \sigma_{rev}}{2} \quad (3.12)$$

the reverse stress is obtained as the stress in the tension-compression test at the reverse strain is 0.01, that is the cumulative strain is 0.03 as shown Fig. 3.2.

When the material containing strong obstacles is deformed in one direction, the dislocation loops are left around the obstacle as shown in **Fig. 3.12**. The dislocation loop give rise to the directional internal stress. While when the material containing weak obstacles which can be sheared by the dislocations, no dislocation loop will be left, resulting in low internal stress. Therefore, the transition from shearable to non-shearable can also be estimated from the increase of the internal stress.

Fig. 3.13 shows the variation of the Bauschinger stress obtained from the result of tension-compression test as a function of aging time. The Bauschinger stress is constant of about 5 MPa until 3.6 ks aging. Then the Bauschinger stress drastically increase after 3.6 ks. This clearly indicates that the volume fraction of non-shearable obstacle increase after 3.6 ks of aging at 723 K. It is worth noting that the shearable/non-shearable transition time of 3.6 ks is consistent with the time estimated from the analysis of initial work hardening rate for the 1123-600 specimen, which also has a large grain size.

3.4.4. Slip system of δ-Ni_2Si in copper matrix

The studies about the initial work hardening rate, Bauschinger effect and TEM observation revealed that the δ-Ni_2Si phase formed in copper matrix can be sheared by dislocations until the aging condition of 3.6 ks at 723 K. In this section, the slip system of δ-Ni_2Si phase in copper matrix will be discussed.

The slip plane of δ-Ni_2Si precipitate, first of all, should be parallel to one of the slip planes of matrix which is {111} planes. **Fig. 3.14(a)** shows 100 pole figures for copper and **Fig. 3.14(b)** shows 001 pole figure for δ-Ni_2Si phase. The pole figures are oriented to satisfy the crystal orientation relationship between the copper matrix and the δ-Ni_2Si precipitate, that is $(100)_m//(001)_{ppt}$ and $[011]_m//[010]_{ppt}$ [7]. Comparing the pole figures provides the fact that the (301) plane of the precipitates is almost parallel to the (11-1) plane of the copper matrix. **Fig. 3.15** shows

the projection of atoms along [010] and dotted lines indicate (301) planes [8]. Fig. 3.15 also provides the fact that the (301) plane is a one of close-packed planes. Therefore, the slip plane of δ-Ni_2Si phase in copper matrix is determined as (301) plane. In addition, it is obvious from the crystal orientation relationship that the slip direction in δ-Ni_2Si is [010], which is parallel to [011] direction of copper matrix. In fact, it was observed in Fig. 3.9 that the precipitate was sheared in the direction of [011] for the copper matrix, which corresponds to [010] direction for the δ-Ni_2Si. Thus, the slip system in δ-Ni_2Si precipitate in copper matrix is determined as {301}<010>.

3.5. Conclusion

(1) The variation of initial work hardening rate indicated that the transition from shearable to non-hearable of precipitates occur at 3.6 ks and most of precipitates are non-shearable after the peak-aged condition in the specimen with large grain size and low dislocation density.

(2) The transition time becomes earlier as the dislocation density becomes high because the formation and growth of the δ-Ni_2Si phase is fast due to the formation on the dislocations.

(3) In the 1123-600 specimen, it was found that the twinning deformation form in the under-aged condition. The formed twins have the thickness of 1 – 40 nm and cause the increase of the work hardening rate. The kinetic of deformation twinning is a complex function of the SFE, the precipitate state and stress level.

Reference

[1] C.P. Blankenship, E. Hornbogen and E.A. Starke: Mater. Sci. Eng. A, **169** (1993) 33.

[2] L.M. Cheng, W.J. Poole, J.D. Embury and D.J. Lloyd: Metall. Mater. Trans. A, **34** (2003), 2473.

[3] W.J. Poole, X. Wang. D.J. Lloyd and J.D. Embury: Philos. Mag., **85** (2005), 3113.

[4] Y. Estrin: in Unified Constitutive Laws of Plastic Deformation, A.S. Krausz and K. Krausz, eds., Academic Press New York, NY, 1996, 69.

[5] A.J. Foreman and M.J. Makin: Phil. Mag., **14** (1966), 911.

[6] G.D. Moan: Acta Metallugica, **27** (1979), 903.

[7] S.A. Lockyer and E. F. Noble: J. Mater. Sci., **29** (1994), 218.

[8] K Toman: Acta Cryst., **5** (1952), 329.

(A)

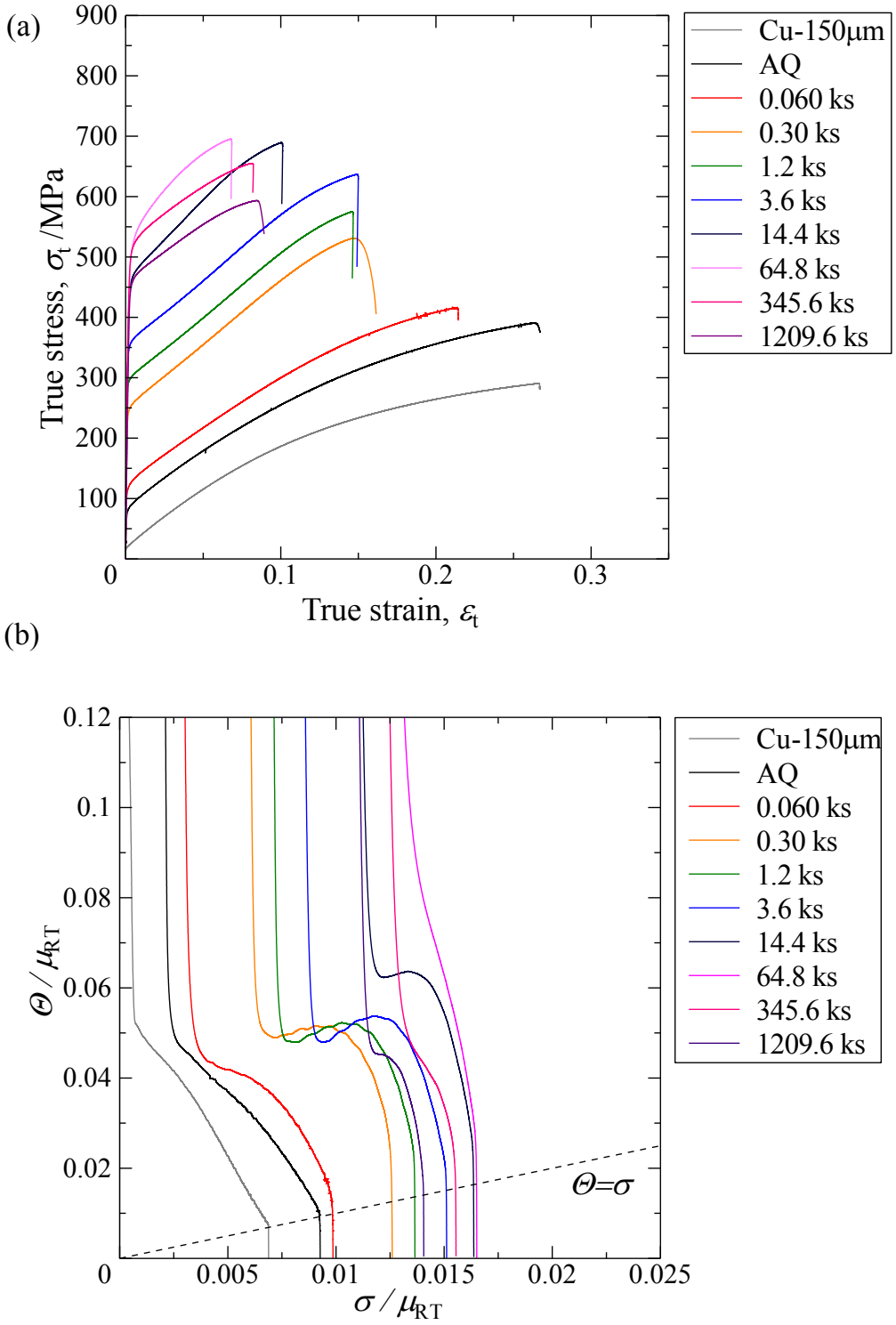

Fig. 3.1 (a) The true stress - true strain curves and (b) the corresponding Kocks-Mecking plots for (A) 1123-600, (B) 1123-30, and (C) 1073-30 aged at 723K for various times.

(B)

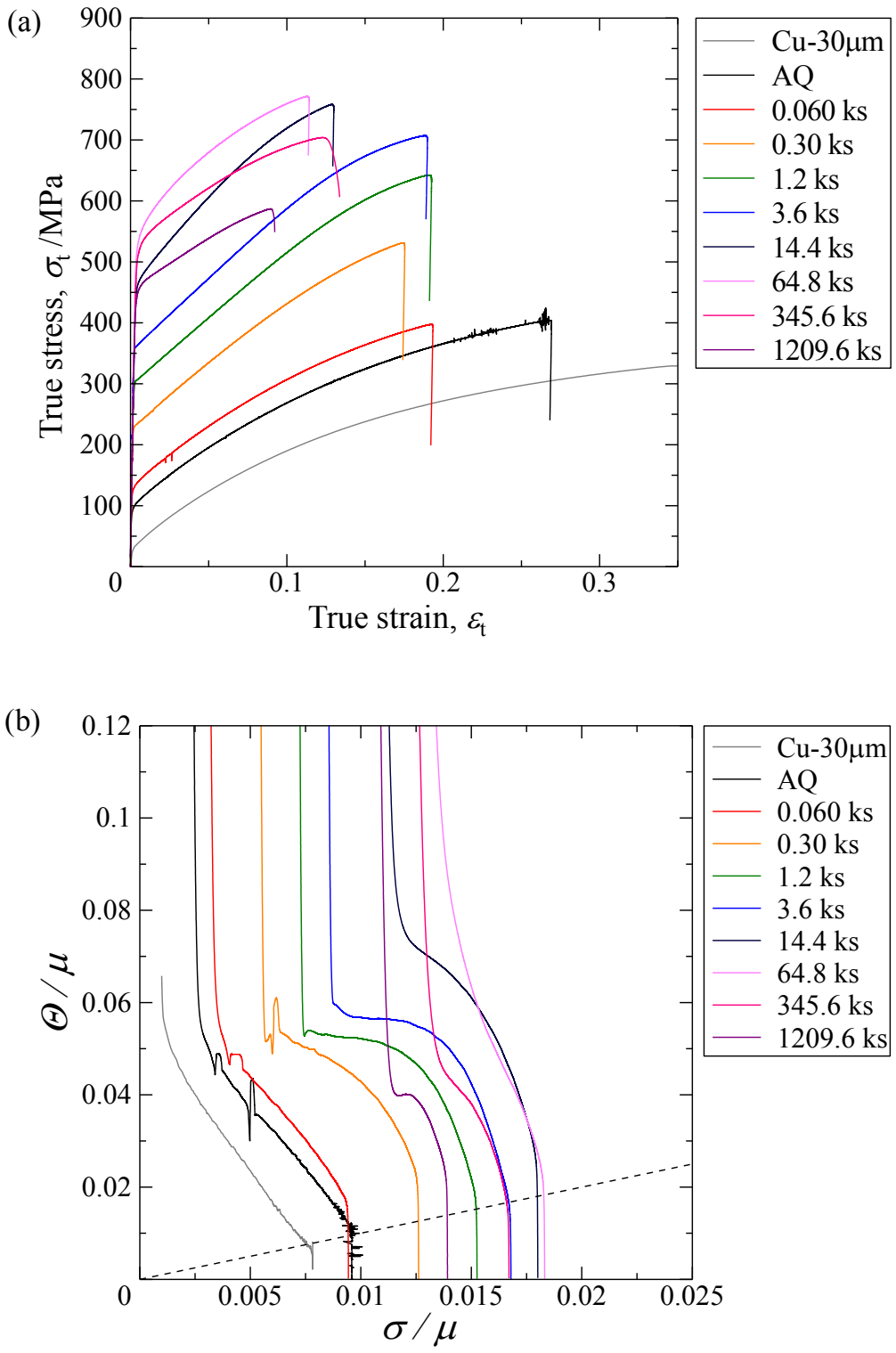

Fig. 3.1 Continued.

(C)

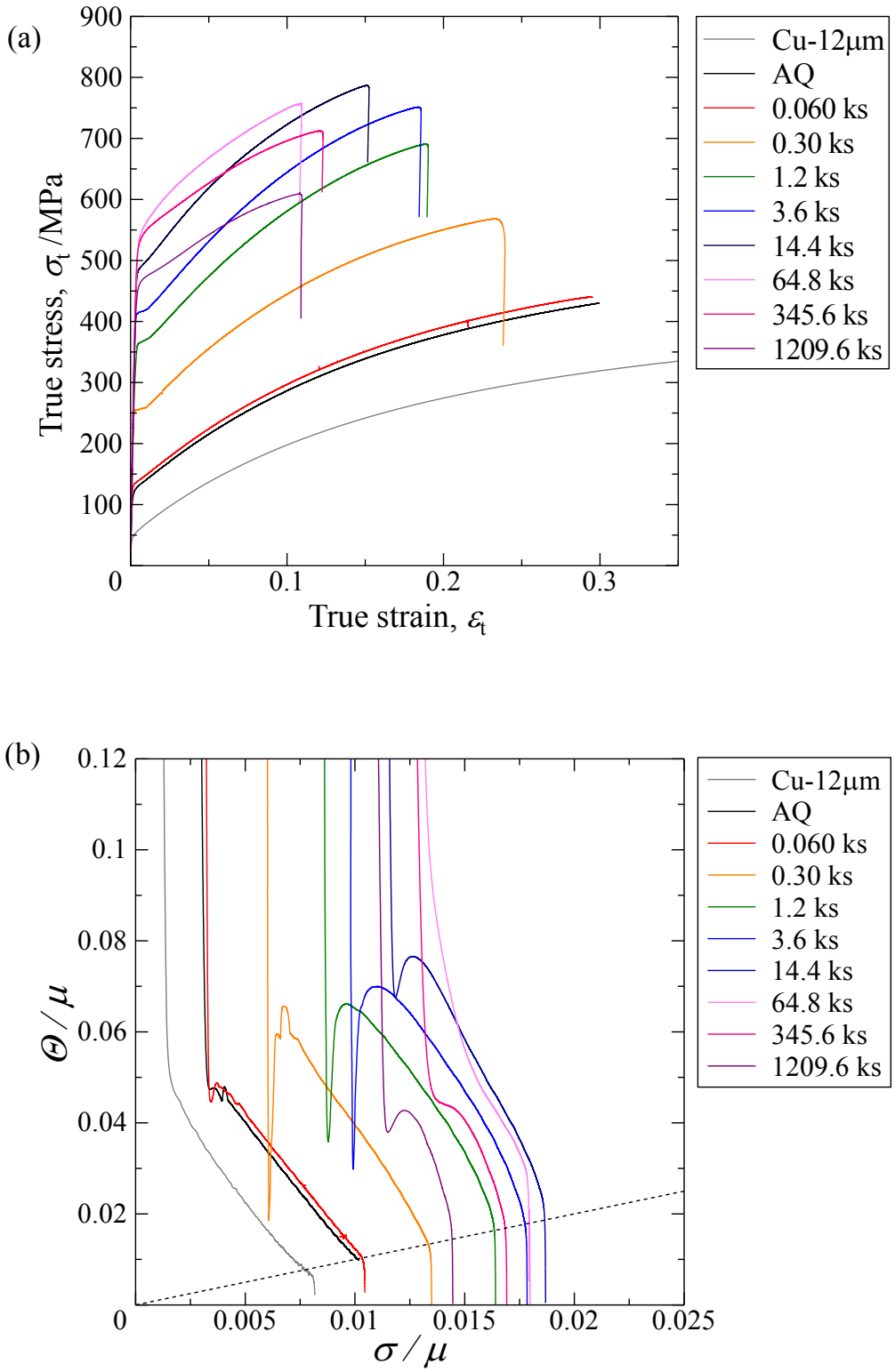

Fig. 3.1 Continued.

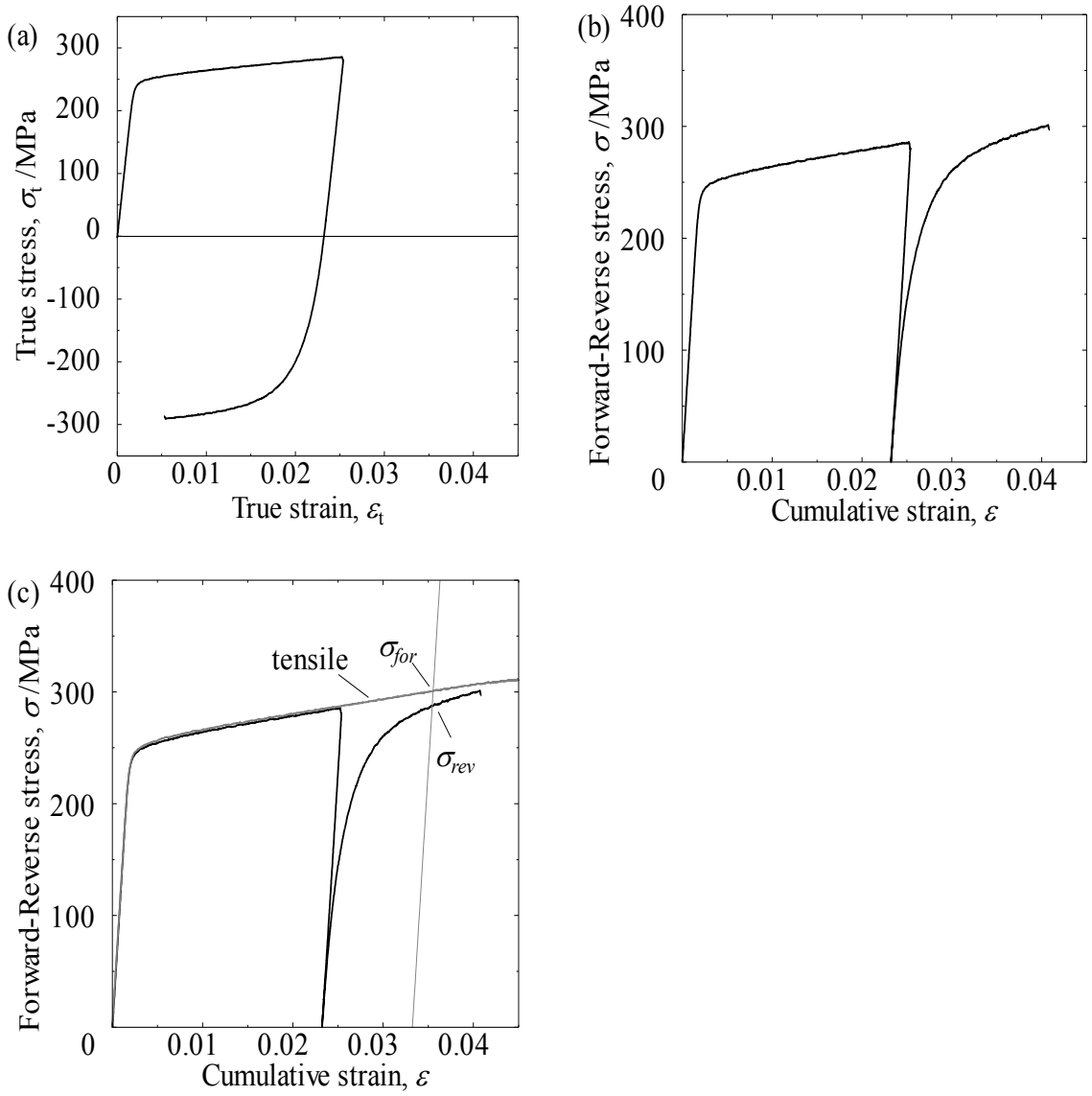

Fig. 3.2 Illustration of the stress-strain analysis in the case of 1.2 ks aged sample: (a) true stress-strain curve, (b) reversed stress-cumulative curve and (c) comparison with the tensile behavior.

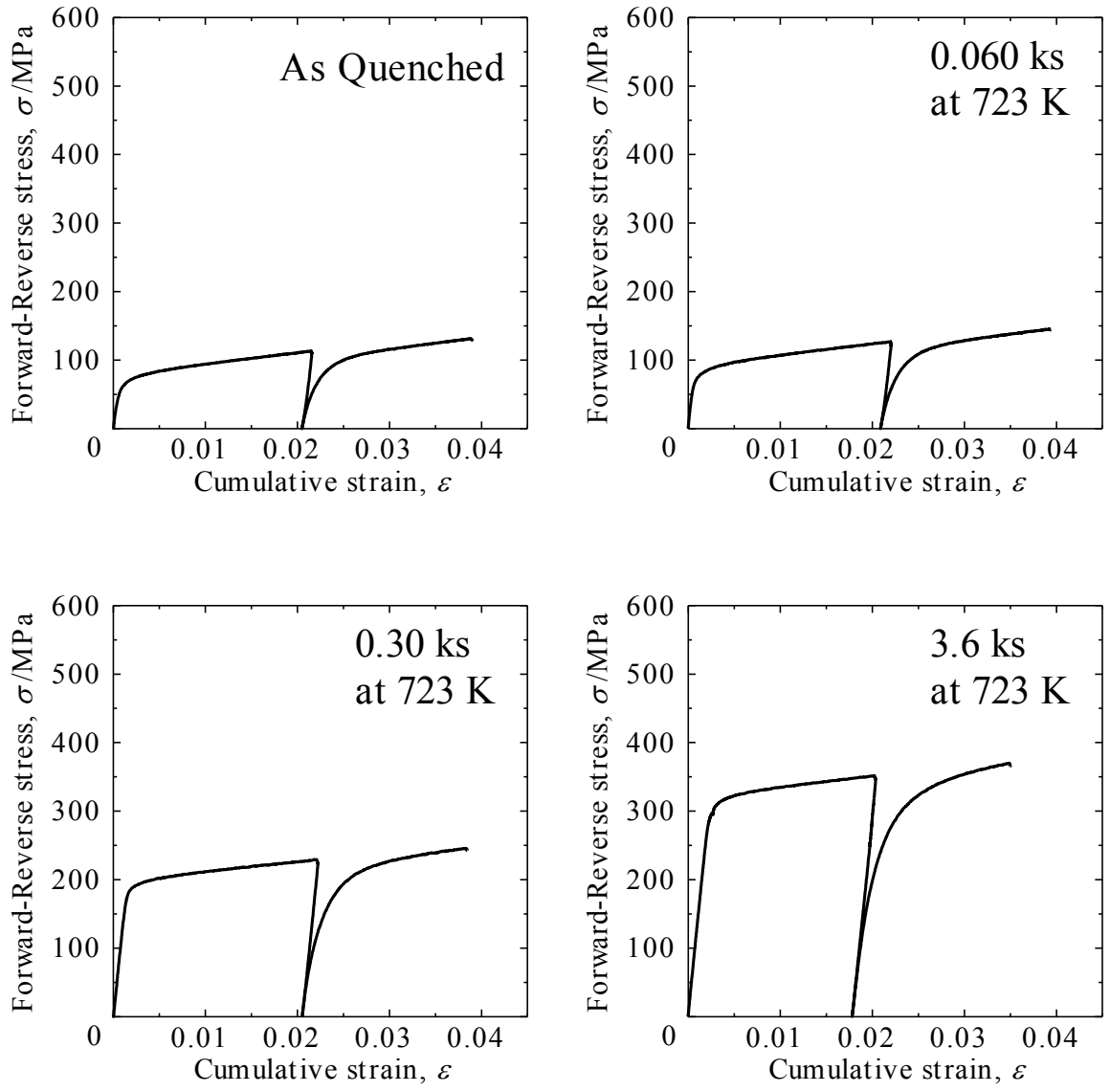

Fig. 3.3 Forward-Reverse stress-strain curves for the Cu-Ni-Si alloy aged at 723 K for various times.

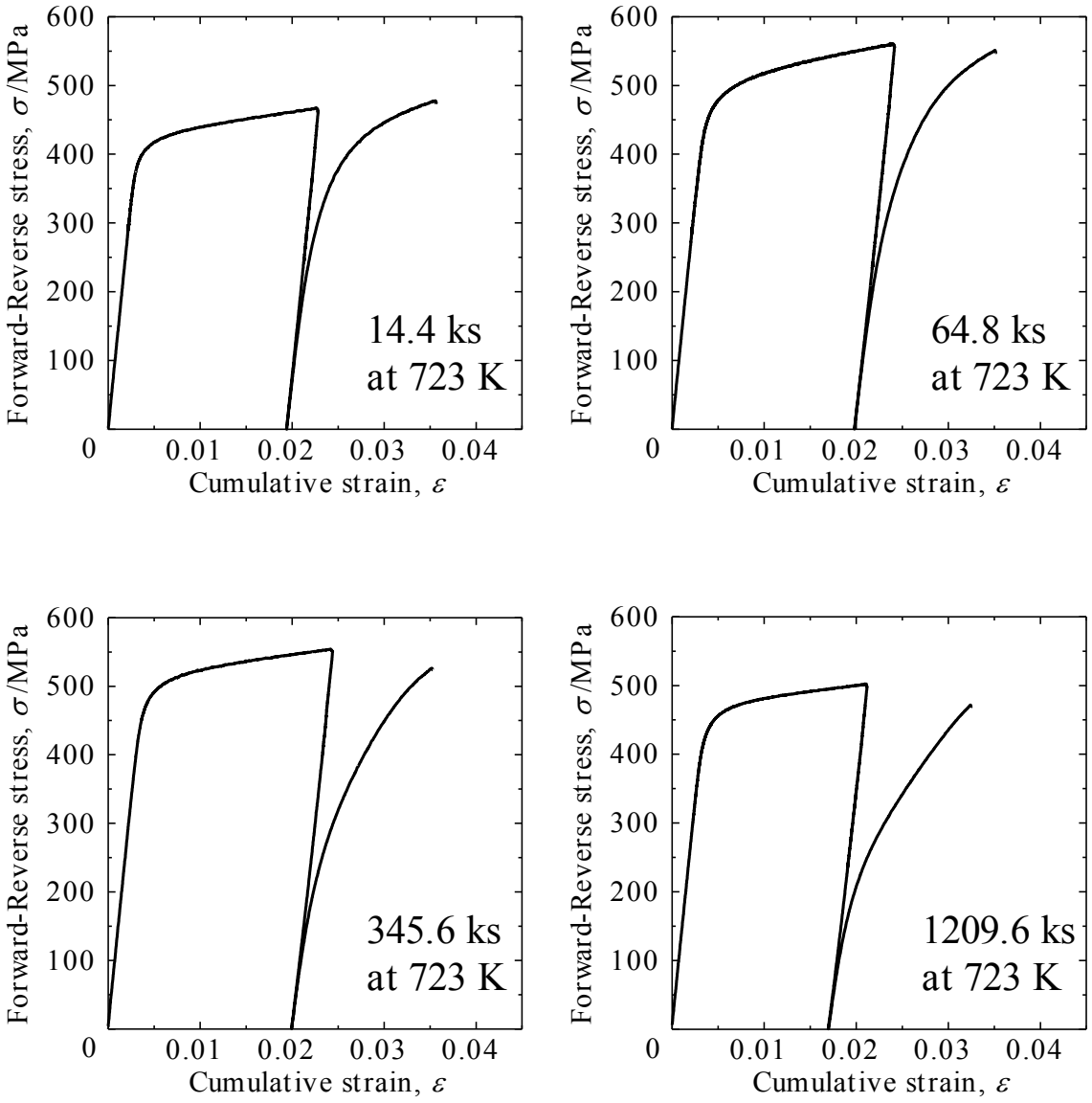

Fig. 3.3 Continued.

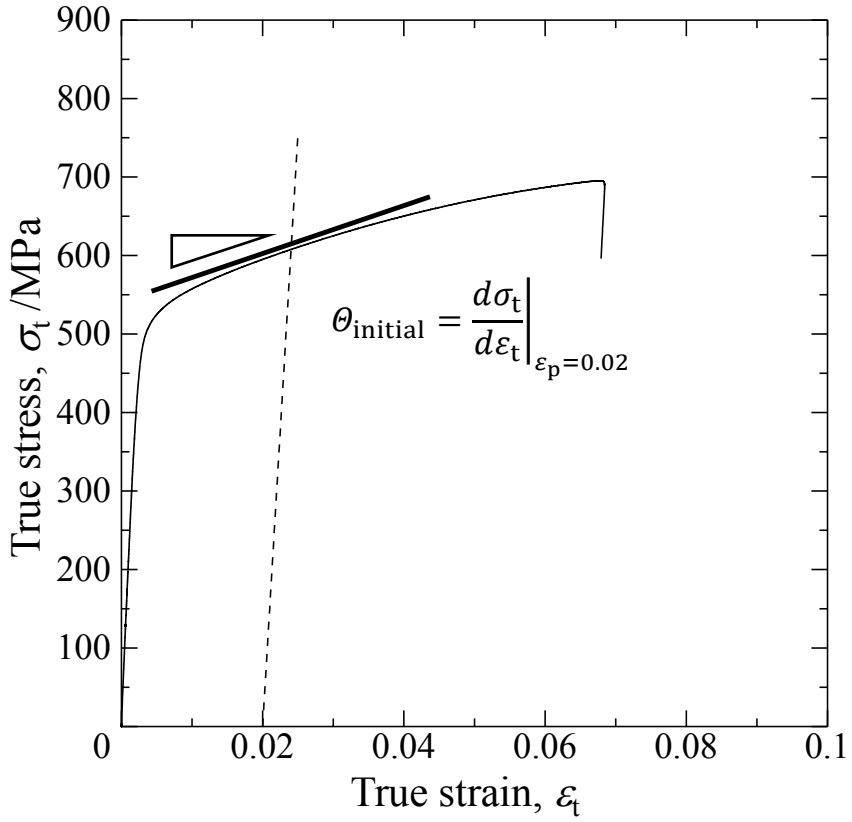

Fig. 3.4 Schematic diagram showing the definition of the initial work hardening rate in this work.

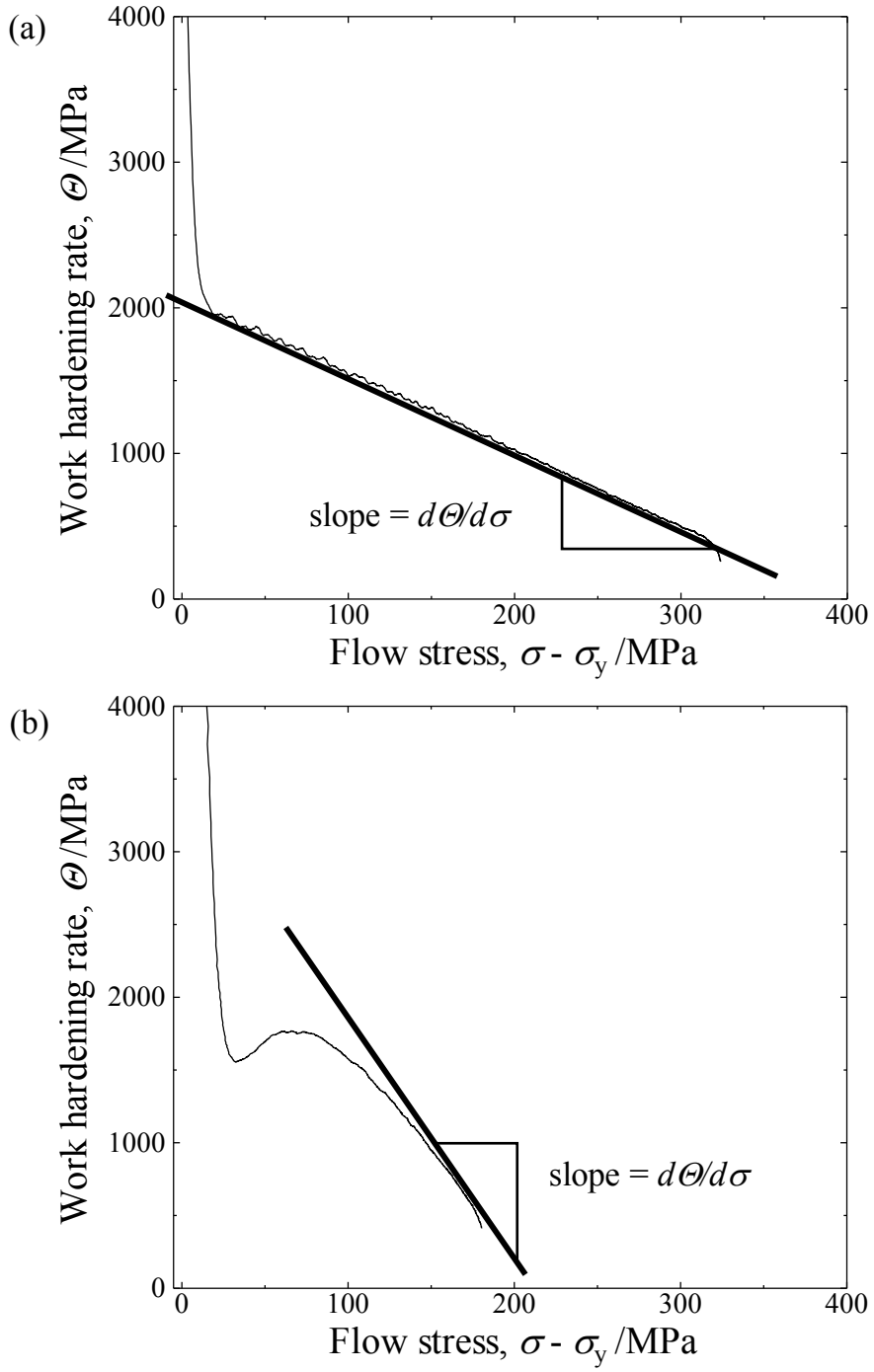

Fig. 3.5 Schematic diagram showing the definition of the slope $d\Theta/d\sigma$ for the two characteristic behaviors observed: (a) linear and (b) nonlinear Kocks-Mecking plots.

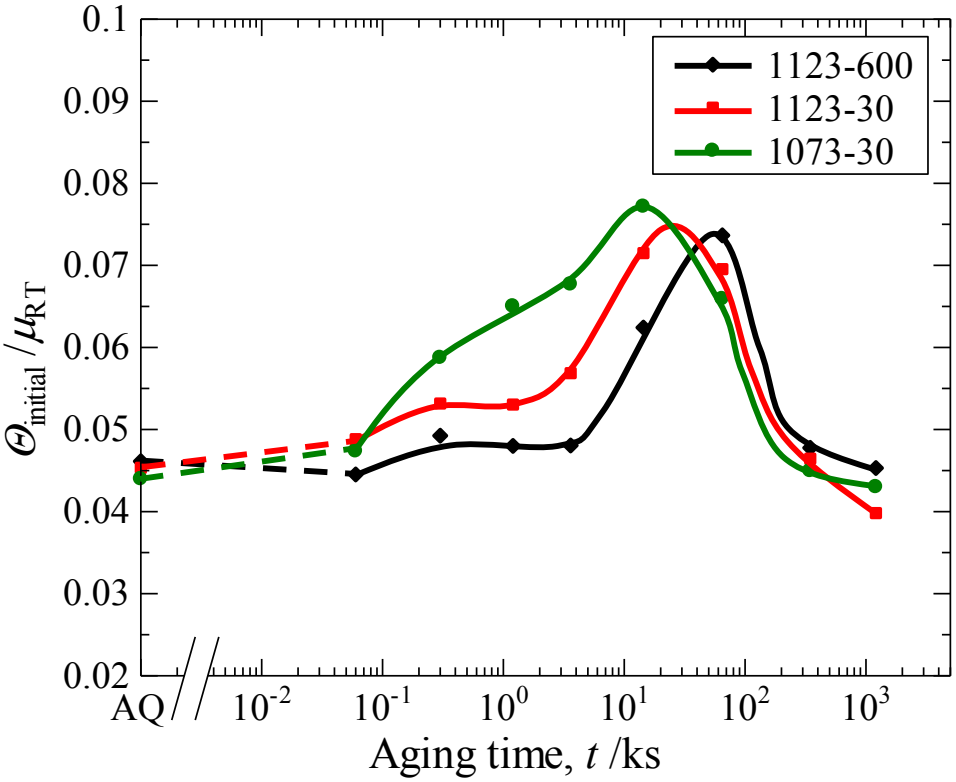

Fig. 3.6 The variation of the initial work hardening rate as a function of aging time for the Cu-Ni-Si alloy with various solution treatment conditions.

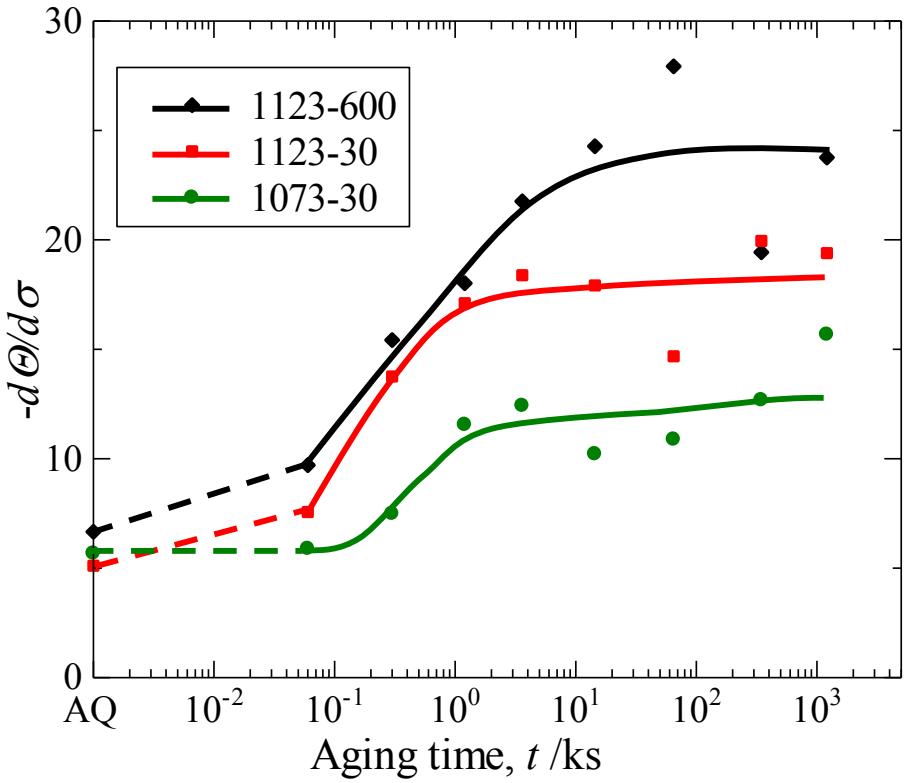

Fig. 3.7 The variation of *–dQ/ds* as a function of aging time for the Cu-Ni-Si alloy with various solution treatment conditions.

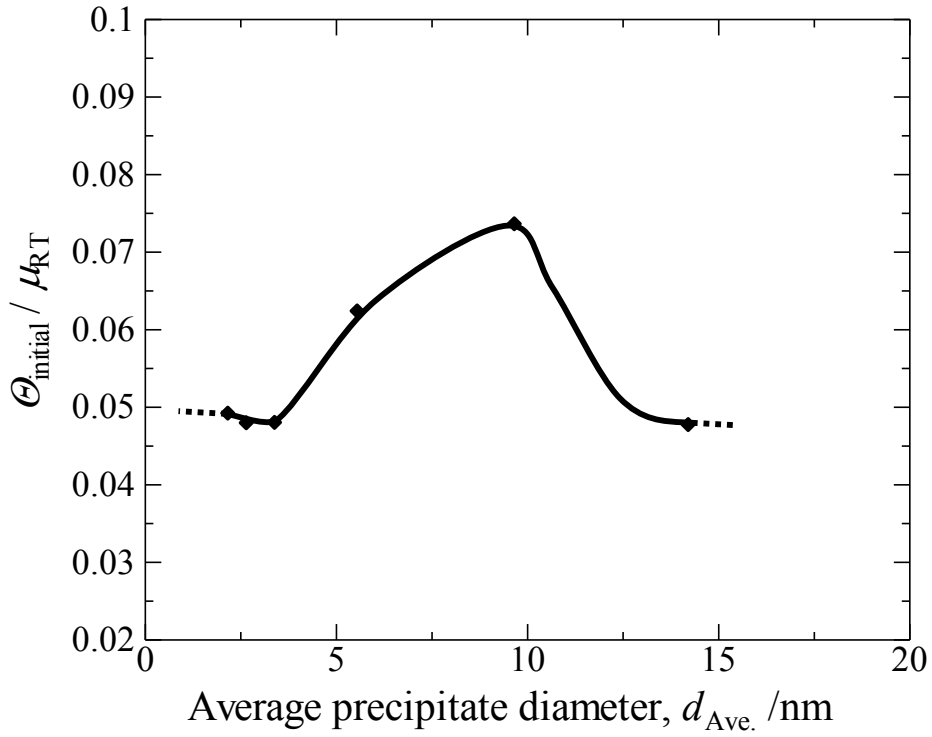

Fig. 3.8 The value of $\Theta_{initial}$ as a function of the precipitate diameter in the 1123-600 specimen.

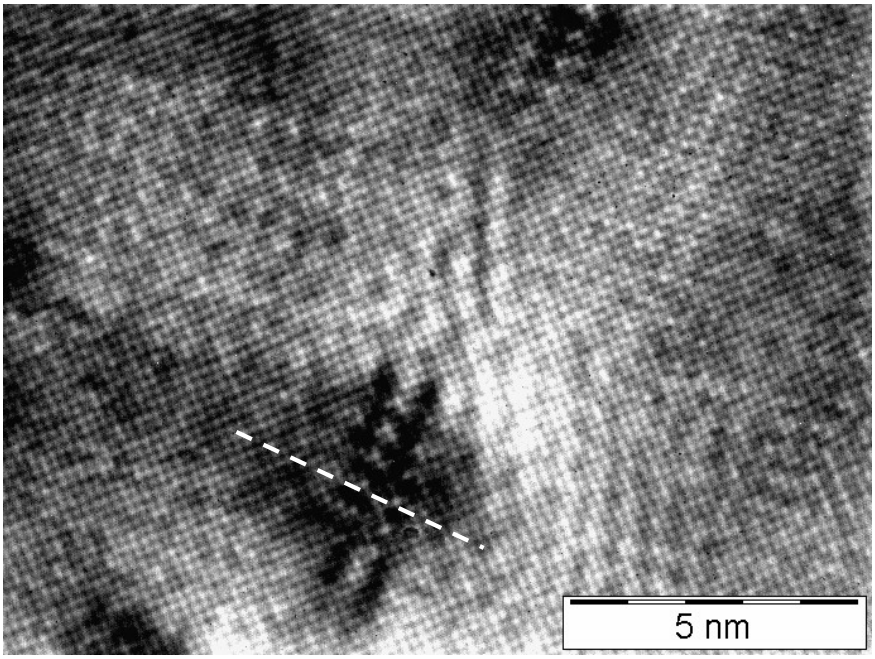

Fig. 3.9 (a) HRTEM image in the 1123-600 specimen aged at 723 K for 0.60 and deformed by 10 % in tension.

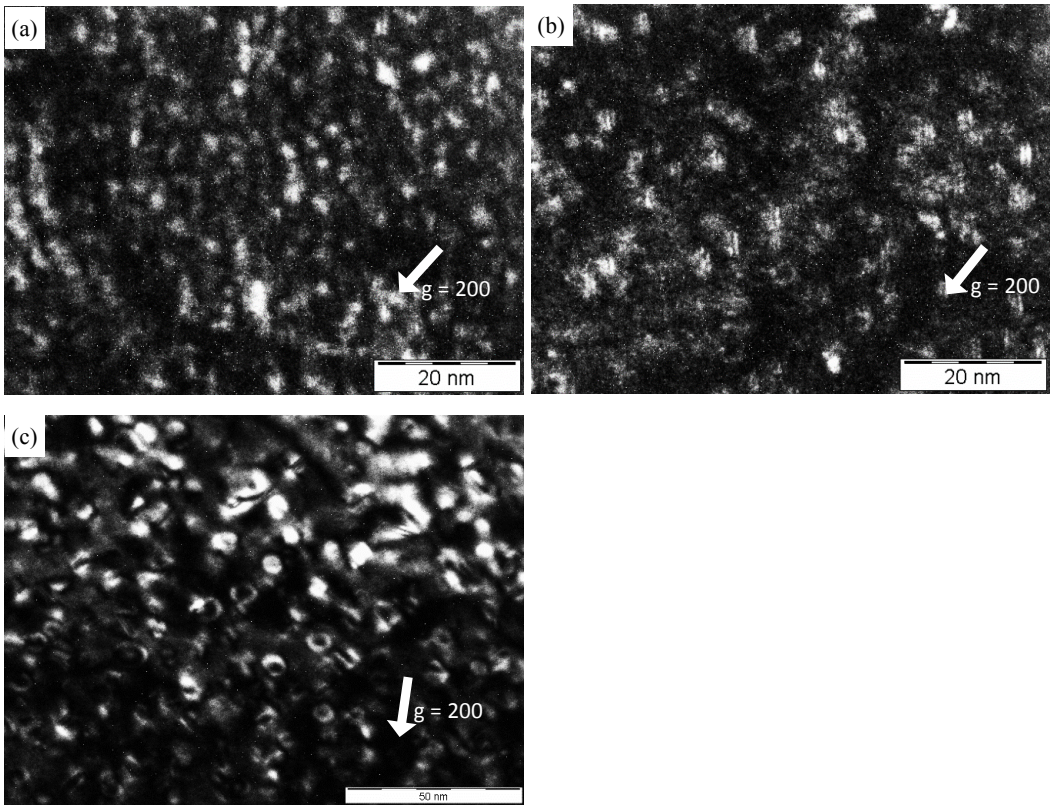

Fig. 3.10 Two-beam dark field image in the 1123-600 specimen aged at 723 K for (a) 0.30 ks (b) 3.6 ks and (c) 64.8 ks and deformed by 2 % in tension.

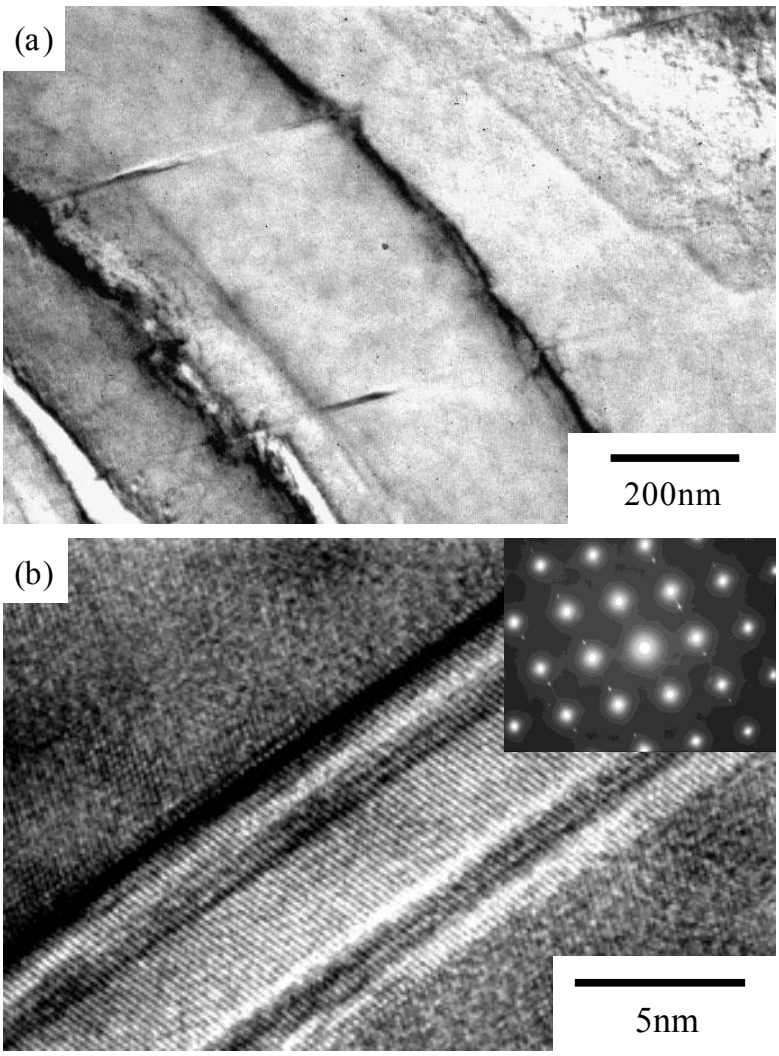

Fig. 3.11 TEM microstructure for the 1123-600s specimen deformed in tension by 10 % after aging at 723 K for 3.6 ks. (b) HRTEM image with a diffraction pattern for a planar defect observed in (a). Beam direction is parallel to $[011]_M$.

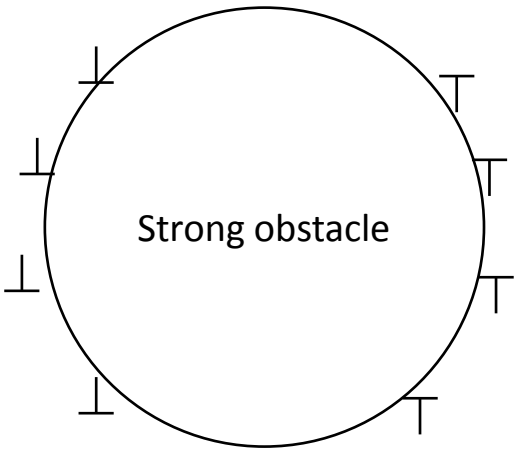

Fig. 3.12 A schematic diagram showing the left dislocation loops around the particle, resulting in the directional internal stress.

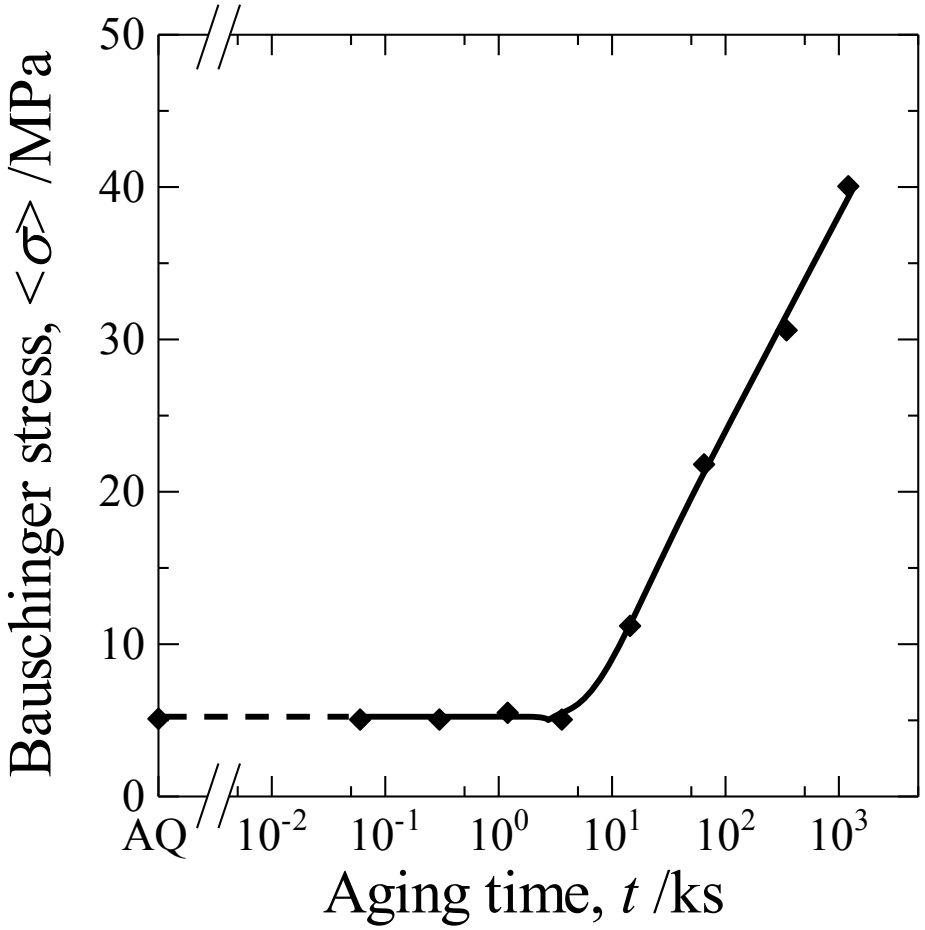

Fig. 3.13 Variation of the Bauschinger stress as a function of aging time for the 1123-600 specimen aged at 723 K.

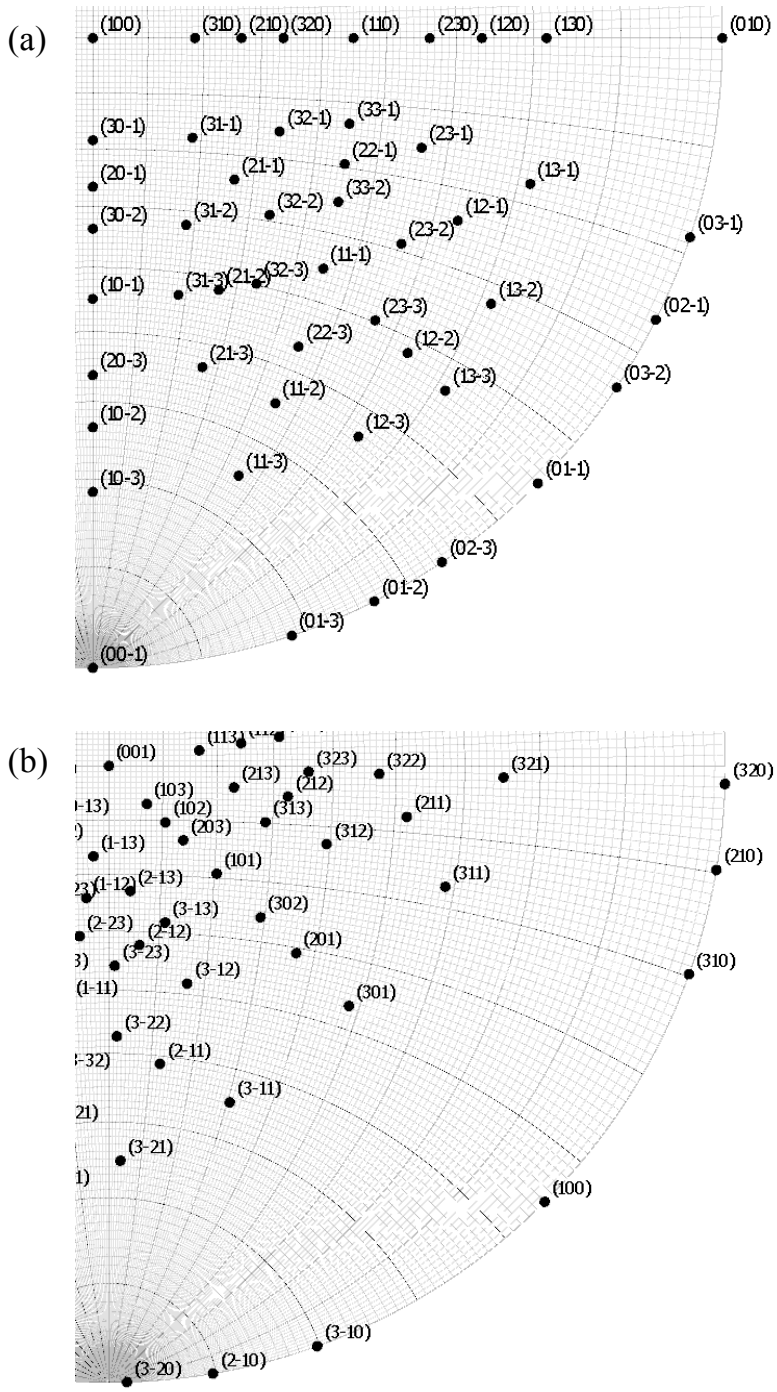

Fig. 3.14 (a) 100 pole figure for copper and (b) 001 pole figure for δ-Ni_2Si phase.

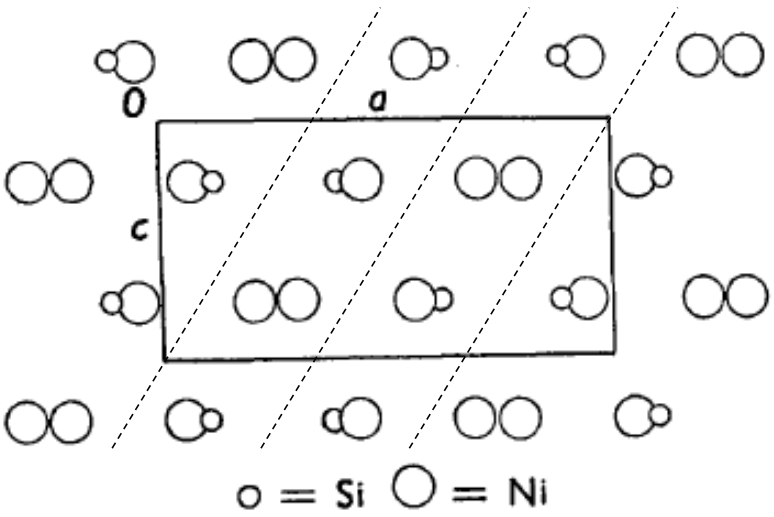

Fig. 3.15 Atom projection for δ–Ni_2Si along [010]. Dotted lines indicate {301} planes.

Chapter 4

Deformation twinning behavior in Cu-Ni-Si alloys

4.1. Introduction

In chapter 3, it has been found that the twinning deformation occur in the 1123-600 specimen and the formation of nano-twin accelerates the work hardening of the specimen. It is well know that the twinning induced plasticity (TWIP) appears in the low stacking fault energy (SFE) materials. Furthermore, it is known that copper based alloys such as Cu-Zn [1] or Cu-Al [2] which have low stacking fault energy (SFE) show evidence of deformation twinning which makes the work hardening behavior further complicated. Blewitt et al. [3] suggested that deformation twinning also occurred in copper single crystals tested at low temperature. The TWIP effect is much utilized in steels like Fe-Mn-C system [4] in order to obtain high ductility and strength. However, the effect of dispersed particle on the TWIP effect is not clarified yet.

In this chapter, the work hardening behavior of the Cu-Ni-Si alloy that the SFE decreased by lowering test temperature or by an addition of Zn with various aging condition was investigated. The objective of this chapter is to investigate the critical factor for the twinning deformation in a precipitate strengthening alloy.

4.2. Experimental

In addition to the alloy with the chemical composition given in Table 2.1, the alloy of which the composition of Zn was increased as given Table 4.1 was prepared. The alloy with the composition given in Table 2.1 was named “Base alloy” and the alloy with high Zn content was named “Zn-added alloy” in this chapter.

For the investigation of the temperature dependence of the work hardening behavior, tensile test at 77 K was also conducted for the Base alloy at a nominal strain rate of 2×10^{-3} s^{-1} using an Instron screw driven tensile machine for the specimen aged at 723 K for various times. The strain was measured in the reduced section of the specimens using a clip-on extensometer with a 25.4 mm gauge length. Tests at 77 K were carried out by immersing the specimens and the extensometer in liquid nitrogen.

For the study about the effect of Zn addition on the work hardening behavior, tensile test was conducted for the Zn-added alloy at room temperature at a nominal strain rate of 1×10^{-3} s^{-1} using

a Shimadzu AG-Xplus screw-driven tensile machine for the specimen aged at 723 K for various times. The strain was measured in the reduced section of the specimens using a Shimadzu SIE-560 automatic extensometer with a 10 mm gauge length.

In order to investigate the deformed microstructures, transmission electron microscopy (TEM) was carried out using a JEOL JEM-3010 transmission electron microscope operating at 300 kV on specimens aged for various times and tensile deformed. Scanning electron microscopy (SEM) and electron backscatter diffraction (EBSD) analyses were also conducted using a JEOL JEM-7000 field-emission scanning electron microscope on the surface of the aged and deformed specimens.

4.3. Result

4.3.1. Work hardening behavior in Base alloy at 77 K

Fig. 4.1 shows the true stress – true strain curves and corresponding Kocks-Mecking plots of the Base alloy aged at 723 K for various times tested at 77 K. Both the work hardening rate and flow stress in Kocks-Mecking plot are normalized by the shear modulus of pure copper at 77 K. The total stress-strain response could not be obtained for as-solution-treated specimen due to slip of extensometer during tensile test. The work hardening behavior at 77 K also changed as aging progressed but it was much different with that at room temperature. It should be noted the work hardening behavior of the 1123-600 specimen aged for 14.4 ks and 64.8 ks were totally different with that at room temperature, i.e. the work hardening rate is low and almost constant (about 1/40 to 1/50 of the shear modulus of copper) throughout tensile deformation.

4.3.2. Deformation microstructure in Base alloy tested at 77 K

Fig. 4.2 shows the inverse pole figure (IPF) maps for the surface of the Base alloy tested to fracture at 77 K with various aging conditions. It was observed that numerous deformation twins were formed in the under aged and peak aged specimens, on the other hand, a few deformation twins were formed in the as-solution-treated and over-aged specimens.

Fig. 4.3 and **Fig. 4.4** show the IPF maps of Base alloy aged at 723 K for 3.6 ks and 64.8 ks deformed at 77 K at various strain, respectively. In both specimen, the area fraction of the

deformation twins increased as strain increased. It was found that the deformation twins were formed at the strain of 0.032 in the 64.8 ks aged specimen, on the other hand, no deformation twin was formed at the strain of 0.051 in the 3.6 ks aged specimen.

4.3.3. Effect of Zn addition on work hardening behavior

Fig. 4.5 shows the true stress – true strain curves and corresponding Kocks-Mecking plots of the Zn-added alloy aged at 723 K for various times tested at room temperature. The curve of the Cu-10Zn brass specimen was also plotted in Fig. 4.5. Both the work hardening rate and flow stress in Kocks-Mecking plot are normalized by the shear modulus of pure copper at room temperature. The curves of the Zn-added alloy were significantly different from the ones of the Base alloy shown in Fig. 3.1, and the total strain was much higher than the Base alloy. The specimens from as-solution-treated to peak-aged condition showed lower work hardening rate than Base alloy. In addition, these specimens had a plateau in the variation of the work hardening rate while the over-aged Zn-added alloy showed no plateau. The Cu-10Zn specimen also showed typical work hardening behavior, that is, linear decrease of work hardening rate and no plateau.

4.3.4. Effect of Zn addition on deformation microstructure

Fig. 4.6 shows the IPF maps for the surface of the Zn-added alloy tested to fracture at room temperature with various aging conditions. It was observed that the deformation twins were formed in the as-solution-treated, under-aged and peak-aged specimens, on the other hand, few deformation twin was observed in the over-aged specimens.

Fig. 4.7 and **Fig. 4.8** show the TEM images in the Zn-added alloy aged at 723 K for 0.30 ks at the strain of 0.10 and 0.20, respectively. **Fig. 4.9** shows the IPF maps for the surface of the Zn-added alloy deformed at various strain. It was observed that the deformation twins formed near a grain boundary at the strain of 0.10 and the twins grew as the strain increased. The very thin deformation twin could not be detected by EBSD with the step size of 0.50 μm up to the strain of 0.20. A few deformation twins were detected by EBSD at the strain of 0.25 and the deformation twin increased as the strain increased. **Fig. 4.10** shows high magnification mapping image at the

strain of 0.28 and 0.31. It was confirmed that the deformation twins have grown mainly in the direction vertical to the twinning plane as the strain increased from 0.28 to 0.31.

4.4. Discussion

4.4.1. Deformation twinning behavior at 77 K

From the microstructure of the specimen after the fracture at 77 K, it is obvious that the tendency of the deformation twinning is strongly depends on the precipitate state. Comparing Fig. 4.1 and Fig. 4.2, it is found that the variation of the work hardening rate during tensile deformation of the specimen in which the deformation twinning occur is very unique. The initial work hardening rate of the 3.6 ks aged specimen is as high as that of the as-solution-treated or over-aged specimen. Then, the work hardening rate gradually decreases as strain increases. Finally, it becomes almost constant over the stress of about 650 MPa. In contrast, the initial work hardening rate is much lower in 64.8 ks aged specimen than that of the other aging conditions. In addition, the work hardening rate of the 64.8 ks aged specimen is almost constant throughout tensile deformation at 77 K.

Fig. 4.11 shows the variation of the area fraction of the deformation twin during the deformation at 77 K obtained from the EBSD maps as a function of strain. Though it is difficult to determine the area fraction of the deformation twin from the EBSD due to the thinness of the deformation twins, it is obvious that the increase of the area fraction starts from small strain in the 64.8 ks aged specimen, while it starts after the strain of 0.05 and significantly increased after the strain of 0.15 in the 3.6 ks aged specimen. This results indicates the critical factor for the formation of the deformation twin is stress rather than strain in the Cu-Ni-Si alloy. In addition, the work hardening stage where the increase of the area fraction of deformation twin corresponds to the stage where the low and constant work hardening rate appears.

Now we can assume that the twinning deformation is much accelerated when the applied stress exceeds the critical stress for twinning. Therefore, the precipitation strengthening plays a significant rule in the deformation twinning. However, the fact that the over-aged specimen that shows higher strength than the under-aged specimens has only a few deformation twins indicates the precipitate state in over-aged condition restricts the twinning deformation. This will be

discussed in chapter 5.

4.4.2. Deformation twinning in Zn added Cu-Ni-Si alloy

The work hardening behavior in the Zn-added alloy also showed the low and constant work hardening rate up to peak-aged condition. These specimens has many deformation twins after the room temperature deformation, while no deformation twin observed in the over-aged specimen. The as-solution-treated specimen also has the deformation twins while it can be considered that no deformation twinning occur in the Cu-10Zn specimen from the work hardening behavior. This indicate the solute atoms in the Cu-Ni-Si alloy also contribute to the deformation twinning even if the content is very small.

From the microstructure change in the Zn-added alloy aged for 0.30 ks given in from Fig. 4.7 to Fig. 4.10, the deformation twinning behavior in precipitate strengthened alloy can be illustrated as shown in **Fig. 4.12**. The deformation twins nucleate at grain boundary, resulting in the low and constant work hardening rate. The low and constant work hardening rate in the specimen in which the deformation twinning occur can be explained by the acceleration of the deformation twinning. The work hardening in the TWIP material is still mainly caused by the dislocation accumulation. When the contribution of the strain by the twinning to total strain increases, the contribution of the strain by dislocation slip decrease. This means that the amount of dislocation gliding decrease, resulting in the low dislocation accumulation rate. In addition, the nano twins can be considered as strong obstacle for dislocations. The formation of nano twins can counteract dynamic recovery of dislocations, resulting in the constant work hardening rate. The reason why the twins nucleate at grain boundary will be discussed in Chapter 5.

Then, the formed twins grows when the work hardening rate decreases. In this grows stage, the nucleation rate decrease as shown in Fig. 4.10, resulting the decrease of the work hardening rate due to the dynamic recovery.

4.5. Conclusion

(1) The formation of the deformation twins significantly depends on the precipitate state. The under-aged and peak-aged specimen had a massive deformation twins after the deformation at 77 K up to fracture. While as-solution-treated and over-aged specimen had only a few deformation twins.

(2) The critical factor for the deformation twinning is considered the applied stress rather than strain. The deformation twins first nucleates near a grain boundary, then grows as strain increases.

(3) The formation of deformation twins results in the low and constant work hardening rate and high elongation.

Reference

[1] Y. Nakao and H. Miura: Mater. Sci. Eng. A, **528** (2011), 1310.

[2] M. Niewczas and G. Saada: Philos. Mag. A, **82** (2002), 167.

[3] T. H. Blewitt, R. R. Coltman and J. K. Redman: J. Appl. Phys., **28** (1957), 651.

[4] O. Bouaziz and N. Guelton: Mater. Sci. Eng. A, **319-321** (2001), 246.

Table 4.1 Chemical composition of the specimens

Specimen		Ni	Si	Sn	Zn	Mg	Cu
Base alloy	mass%	2.17	0.50	0.15	0.50	0.10	Bal.
	mol%	2.33	1.12	0.080	0.48	0.26	Bal.
Zn-added alloy	mass%	2.44	0.51	0.15	9.34	0.13	Bal.
	mol%	2.62	1.15	0.080	9.01	0.34	Bal.

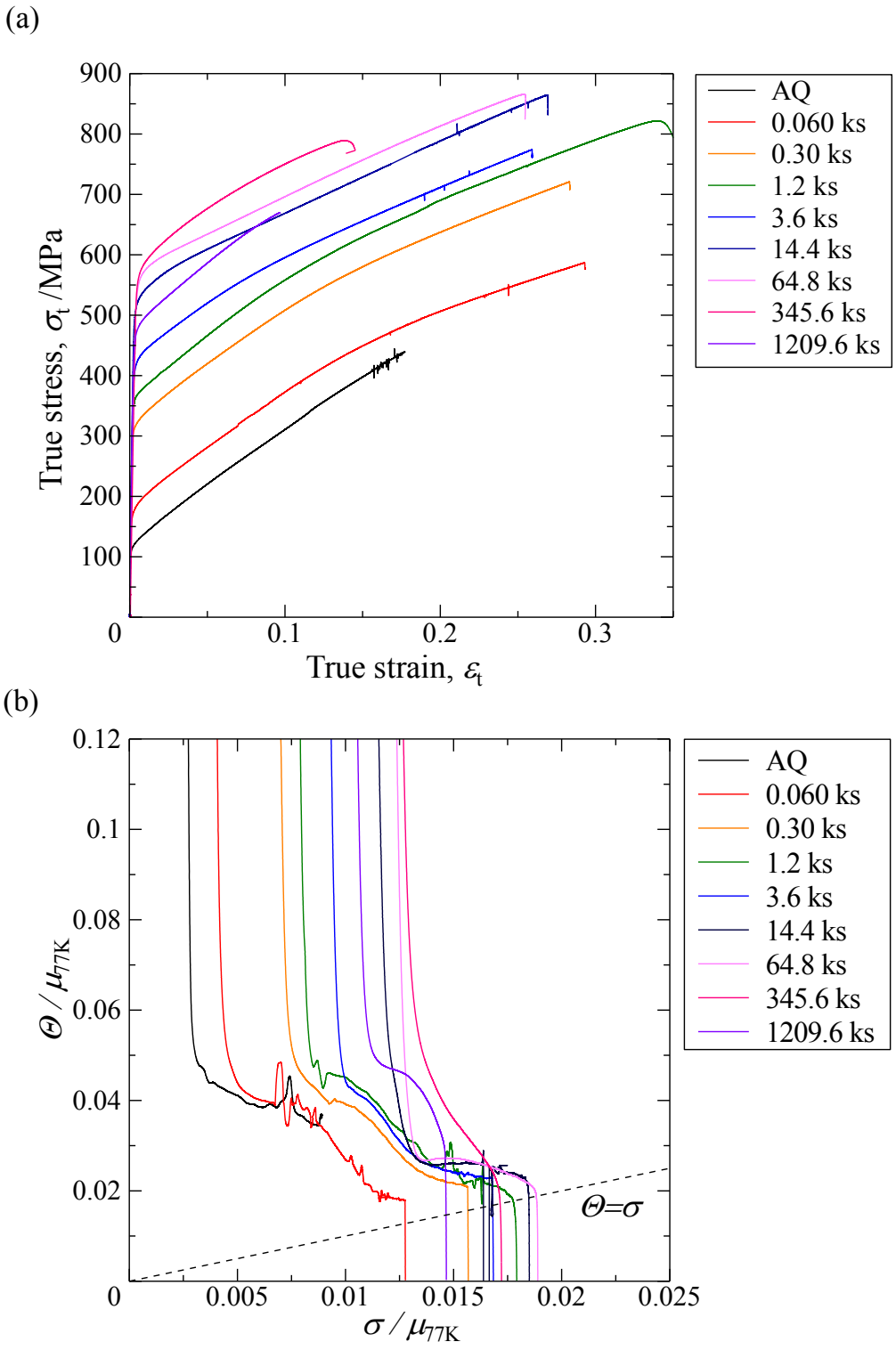

Fig. 4.1 (a) The true stress - true strain curves and (b) the corresponding Kocks-Mecking plots tested at 77 K for the 1123-600 specimen aged at 723K for various times.

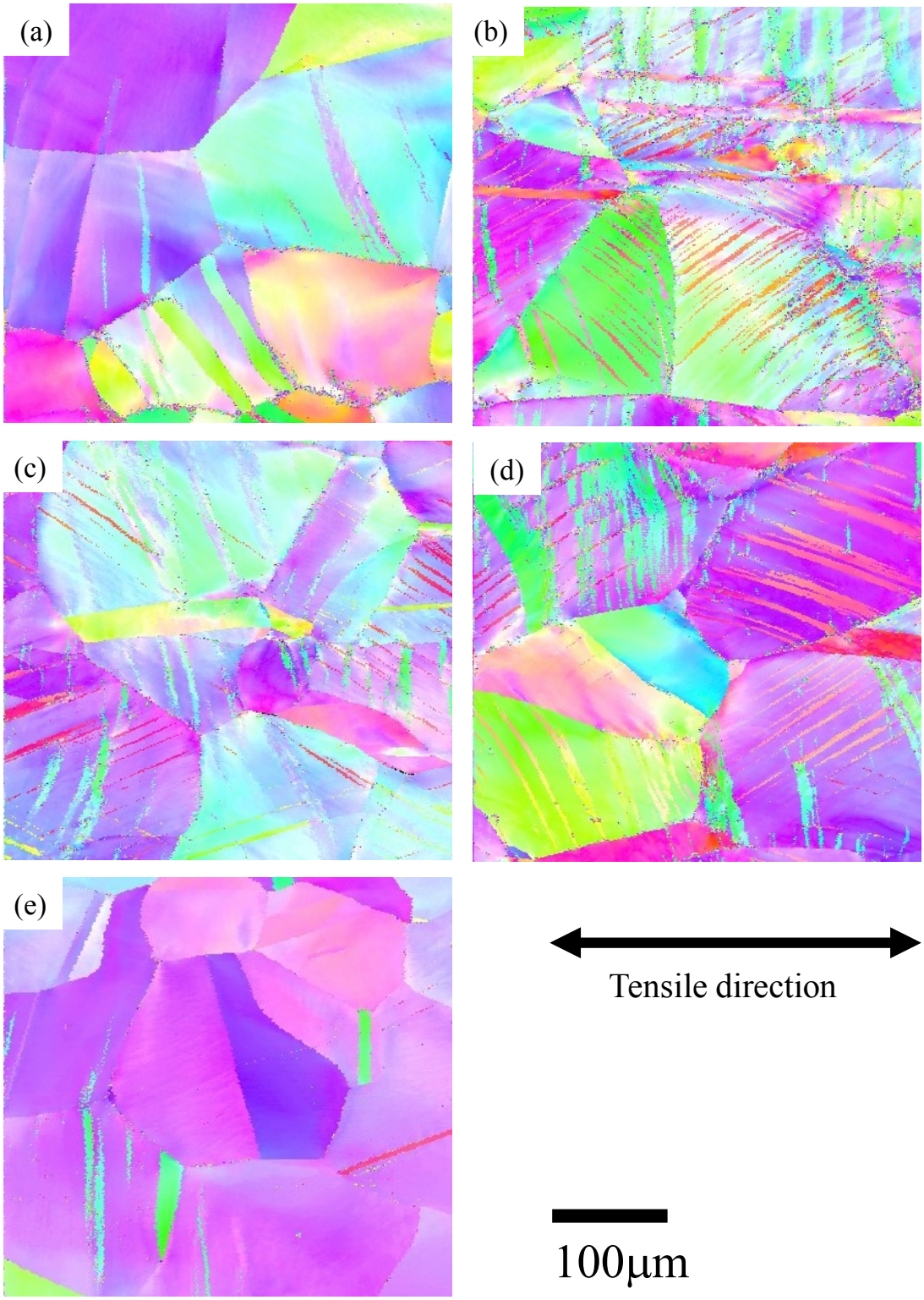

Fig. 4.2 The IPF maps on the surface of the 1123-600 specimen tested to fracture at 77 K for (a) the AQ and aged at 723 K for (b) 0.3 ks, (c) 3.6 ks, (d) 64.8 ks and (e) 1209.6 ks. Note: the true strain at the point of fracture is (a) 0.35, (b) 0.28, (c) 0.25, (d) 0.25 and (d) 0.10.

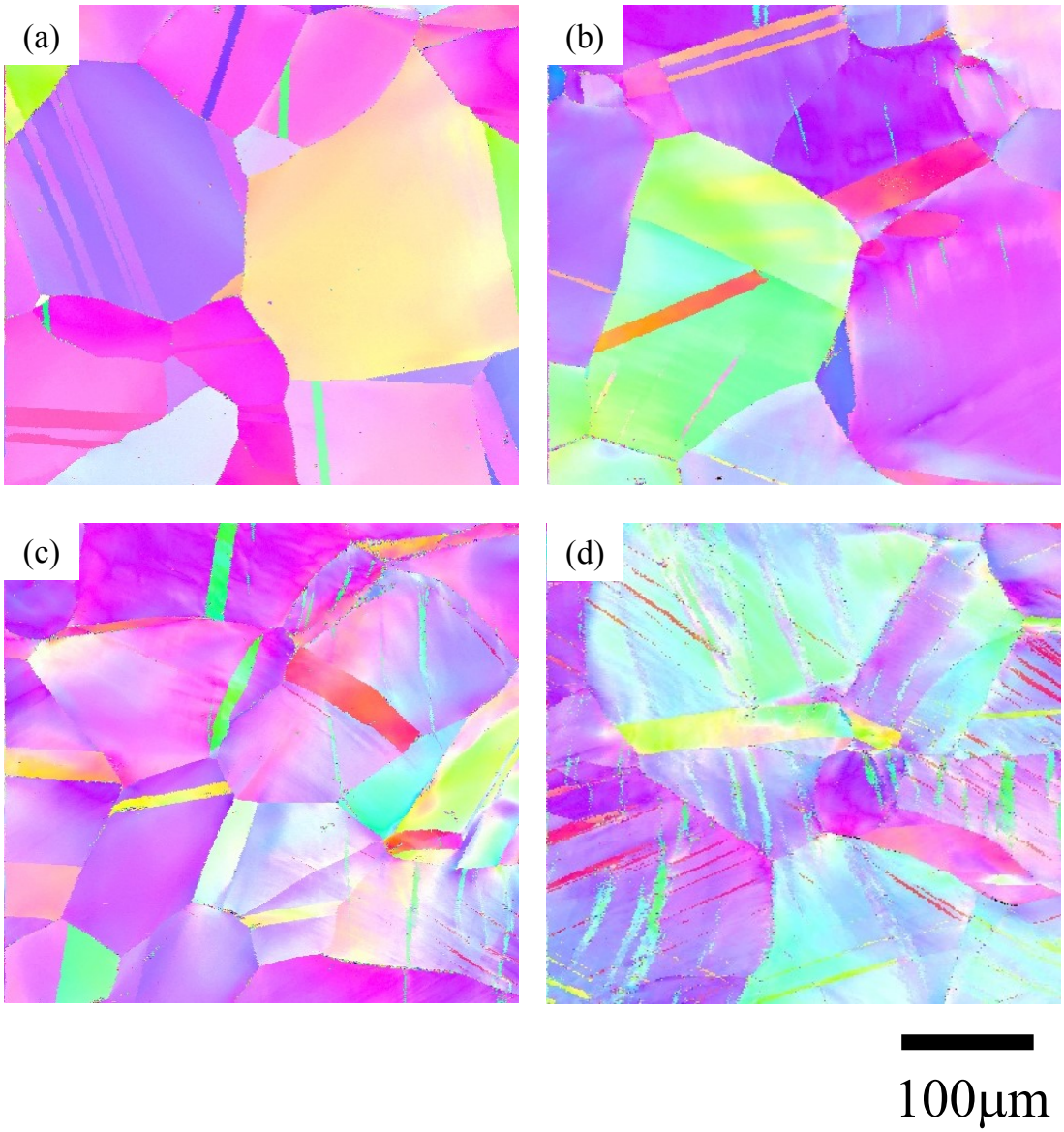

Fig. 4.3 The IPF maps on the surface of the 1123-600 specimen aged at 723 K for 3.6 ks and tested at 77 K to the strain of (a) 0.051, (b) 0.093, (c) 0.16 and (d) 0.25.

.

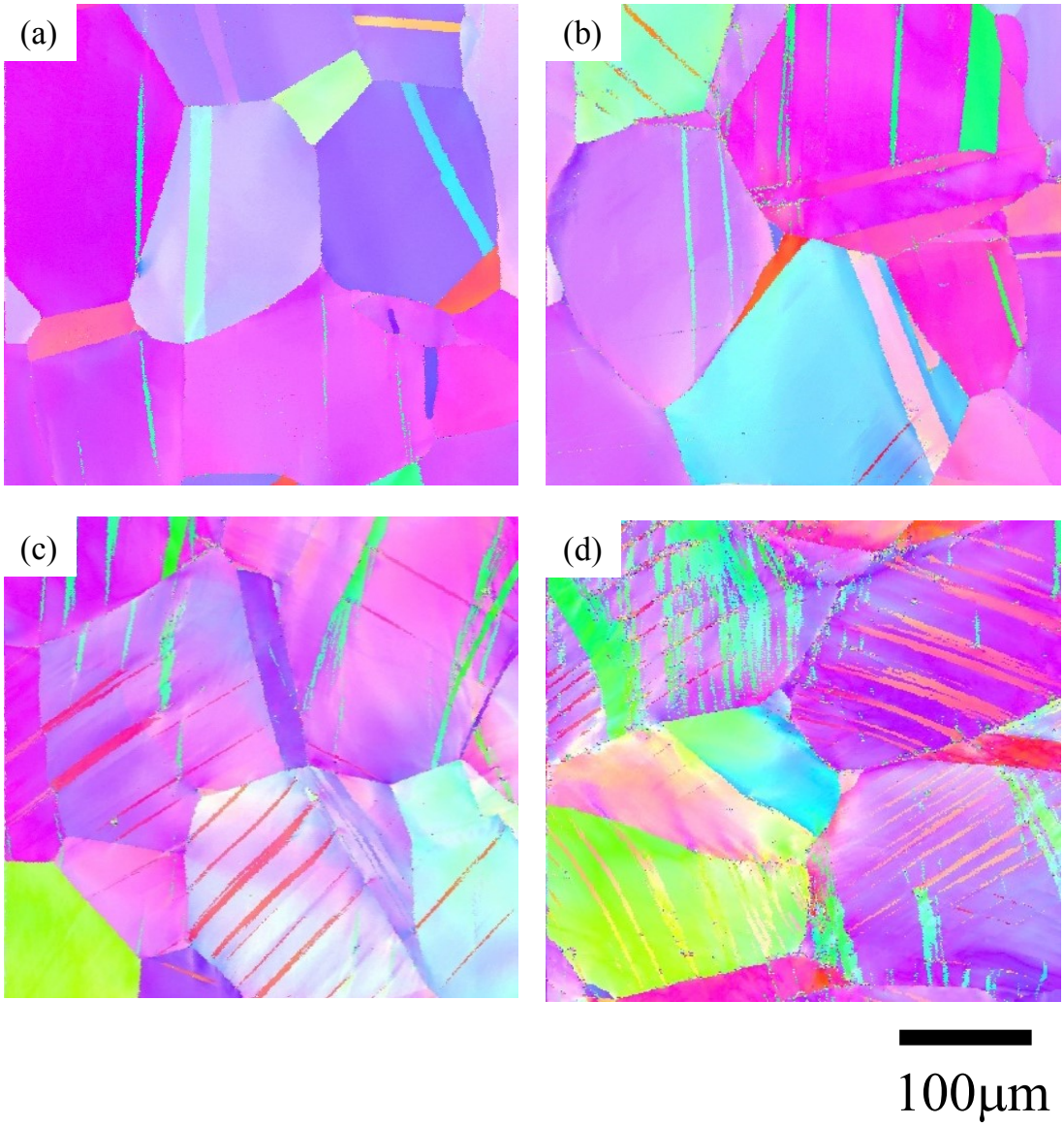

Fig. 4.4 The IPF maps on the surface of the 1123-600 specimen aged at 723 K for 64.8 ks and tested at 77 K to the strain of (a) 0.032, (b) 0.046, (c) 0.11 and (d) 0.25.

.

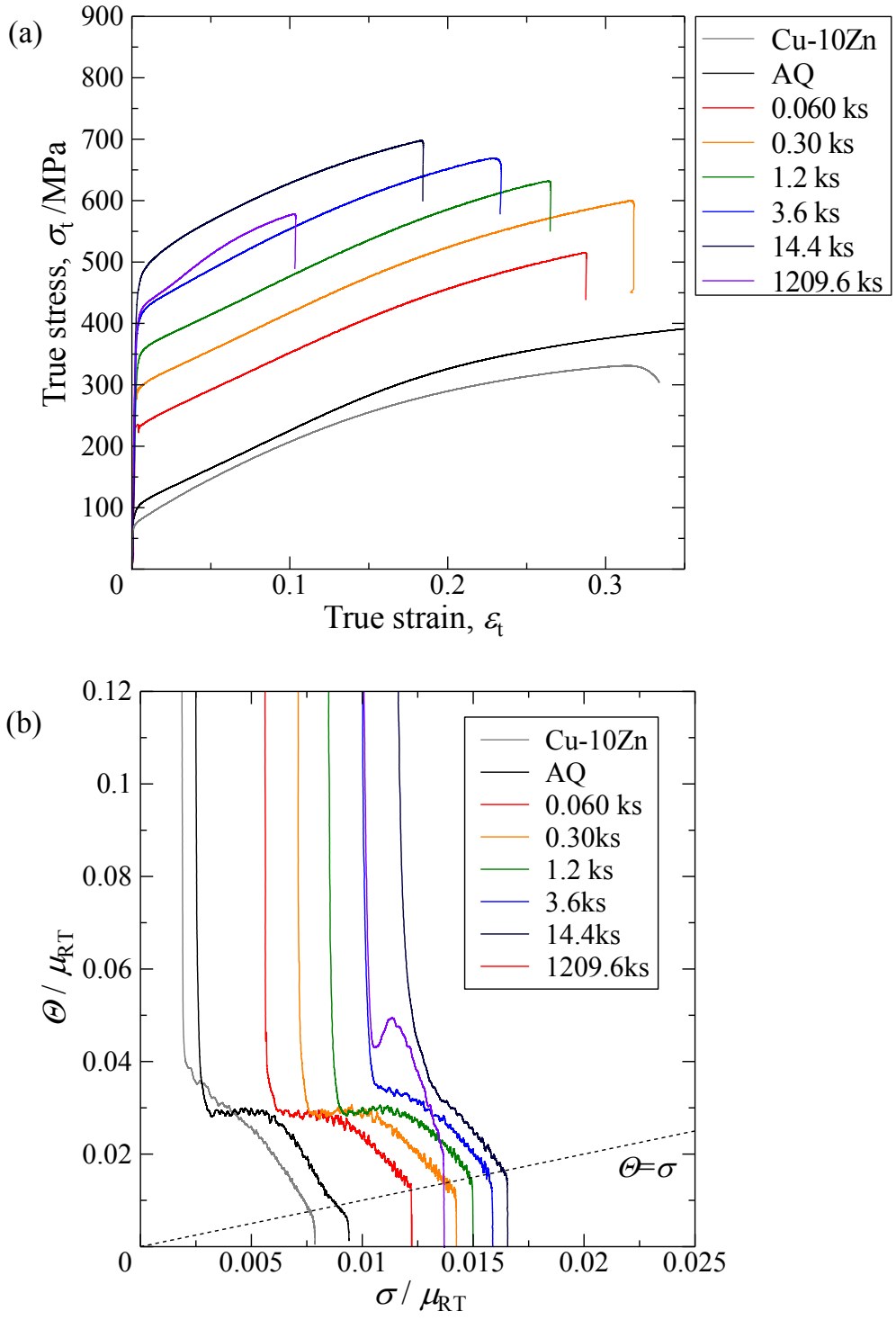

Fig. 4.5 (a) The true stress - true strain curves and (b) the corresponding Kocks-Mecking plots tested at 298 K for the Zn-added 1123-600 specimen aged at 723K for various times.

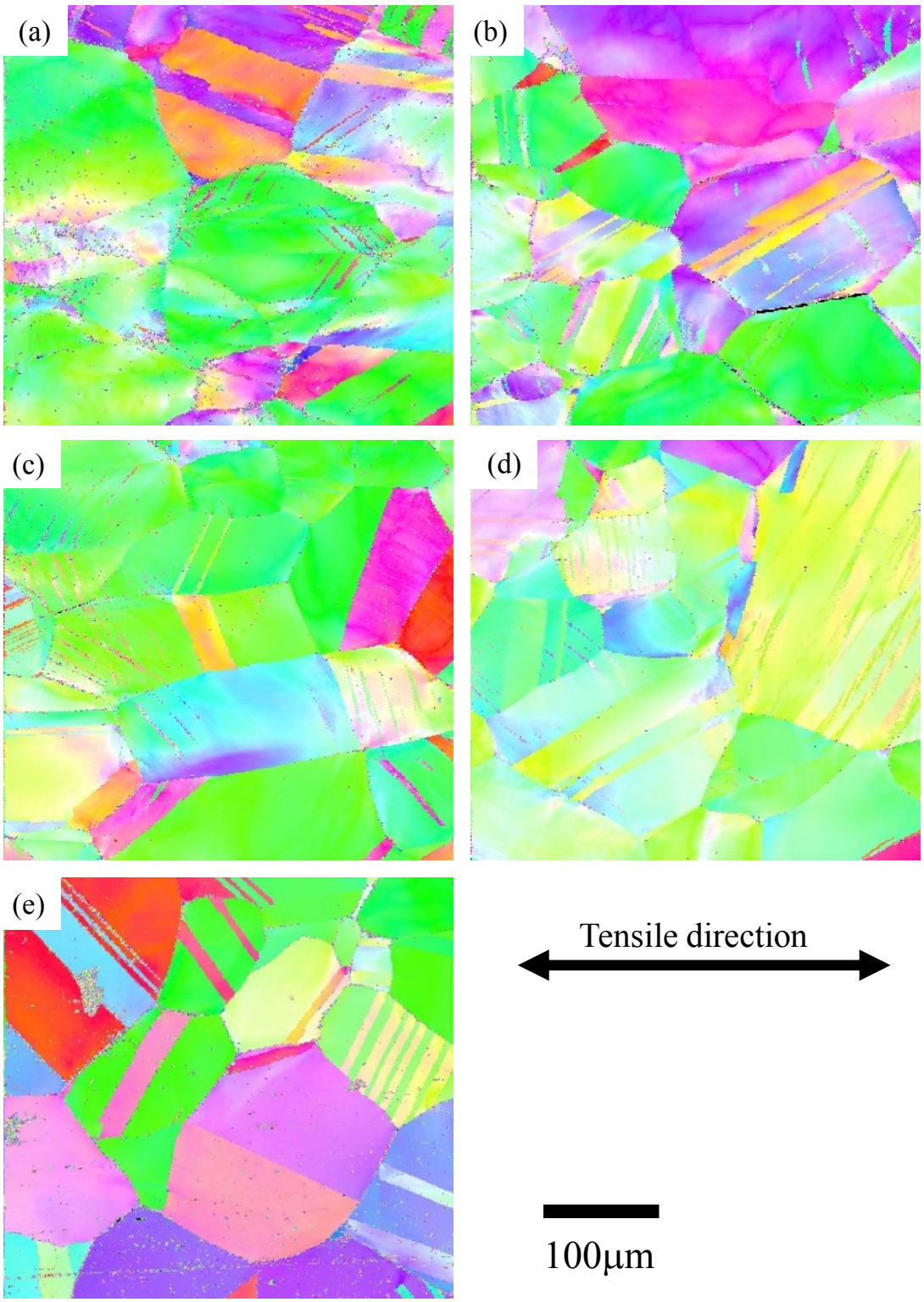

Fig. 4.6 The IPF maps on the surface of the Zn-added 1123-600 specimen tested to fracture at 298 K for (a) the AQ and aged at 723 K for (b) 0.3 ks, (c) 3.6 ks, (d) 64.8 ks and (e) 1209.6 ks.
Note: the true strain at the point of fracture is (a) 0.41, (b) 0.32, (c) 0.23, (d) 0.18 and (d) 0.10.

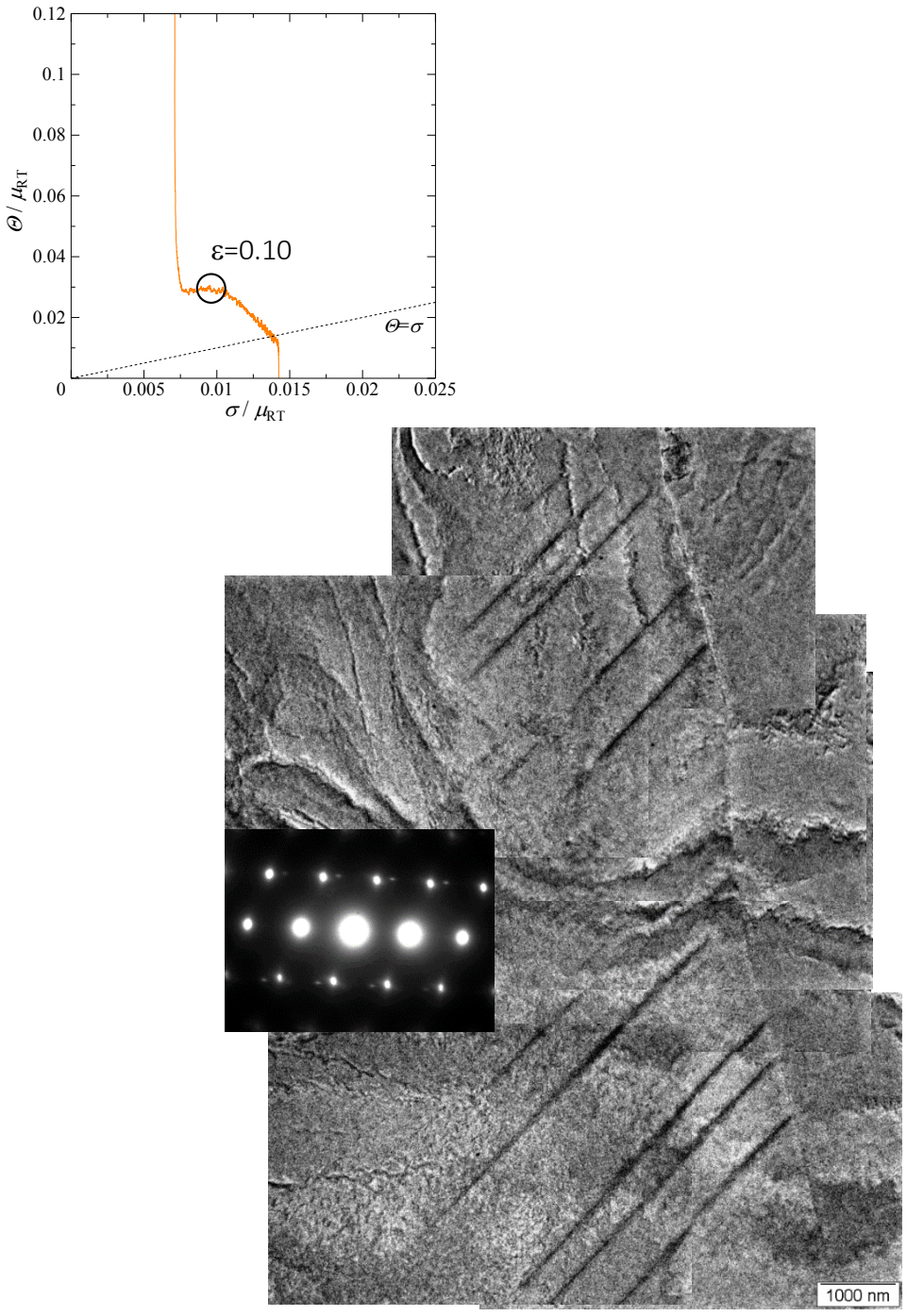

Fig. 4.7 TEM bright field image in the Zn-added 1123-600 specimen aged at 723 K for 0.30 ks and tensile deformed by the strain of 0.10 at 298 K.

.

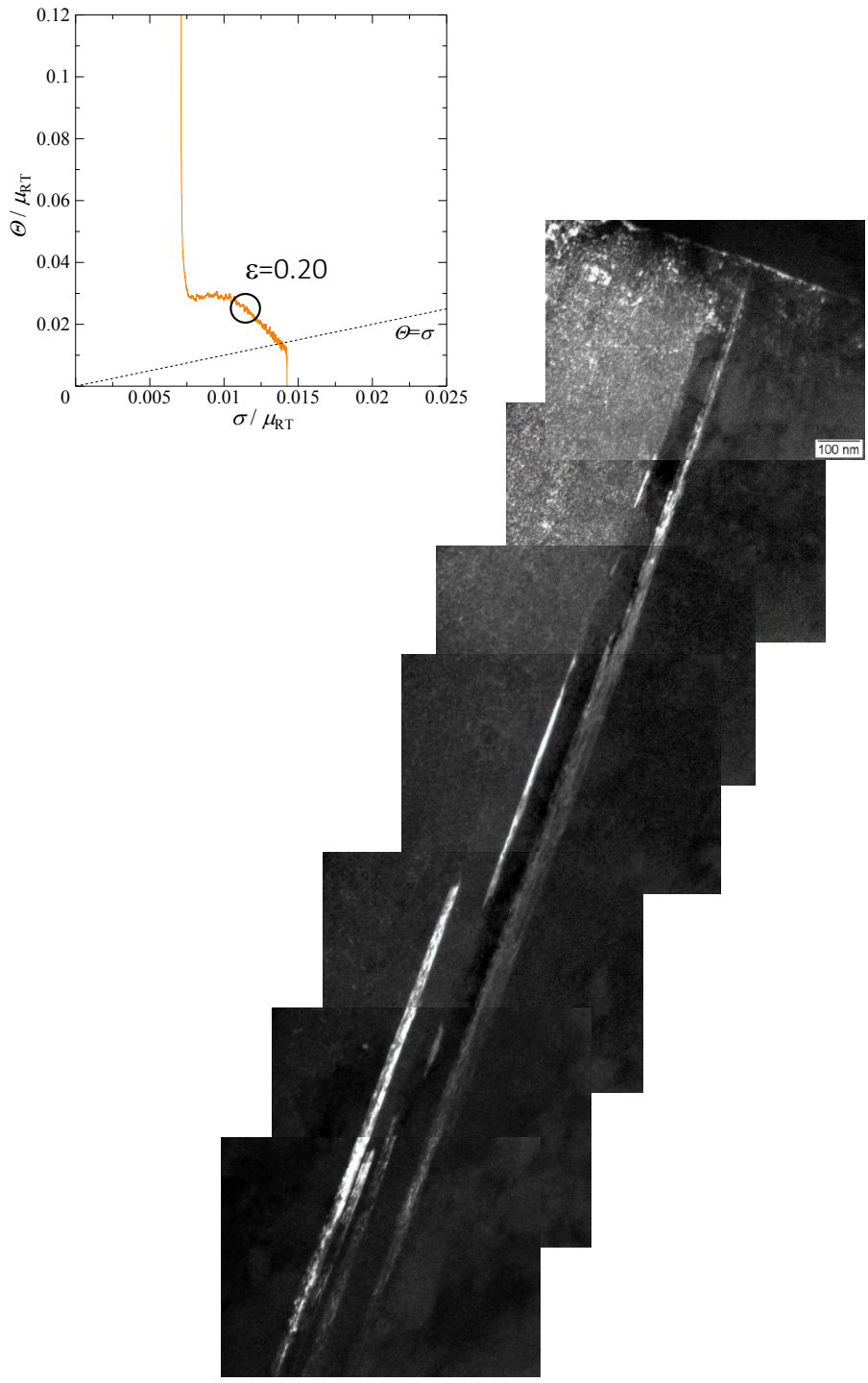

Fig. 4.8(a) TEM dark field image in the Zn-added 1123-600 specimen aged at 723 K for 0.30 ks and tensile deformed by the strain of 0.20 at 298 K.

.

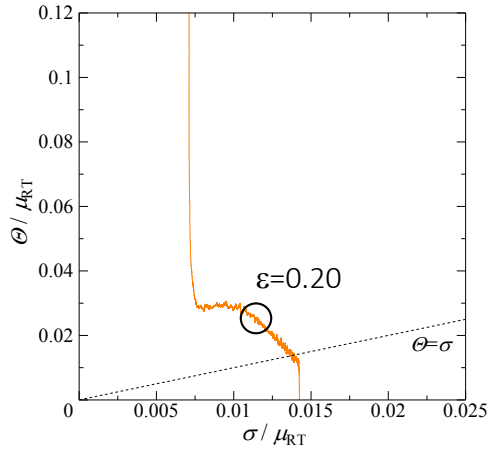

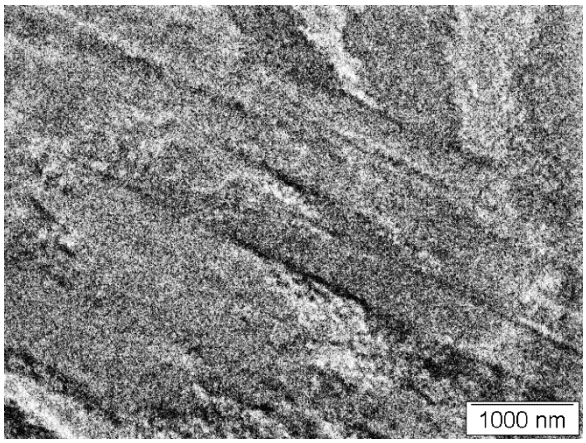

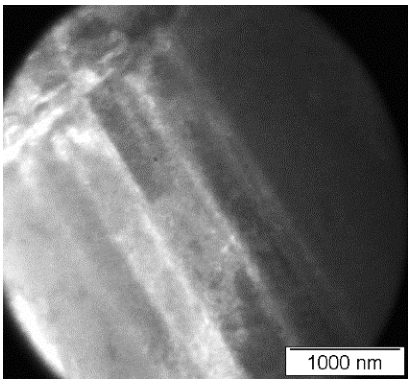

Fig. 4.8(b) TEM images in the Zn-added 1123-600 specimen aged at 723 K for 0.30 ks and tensile deformed by the strain of 0.20 at 298 K.

.

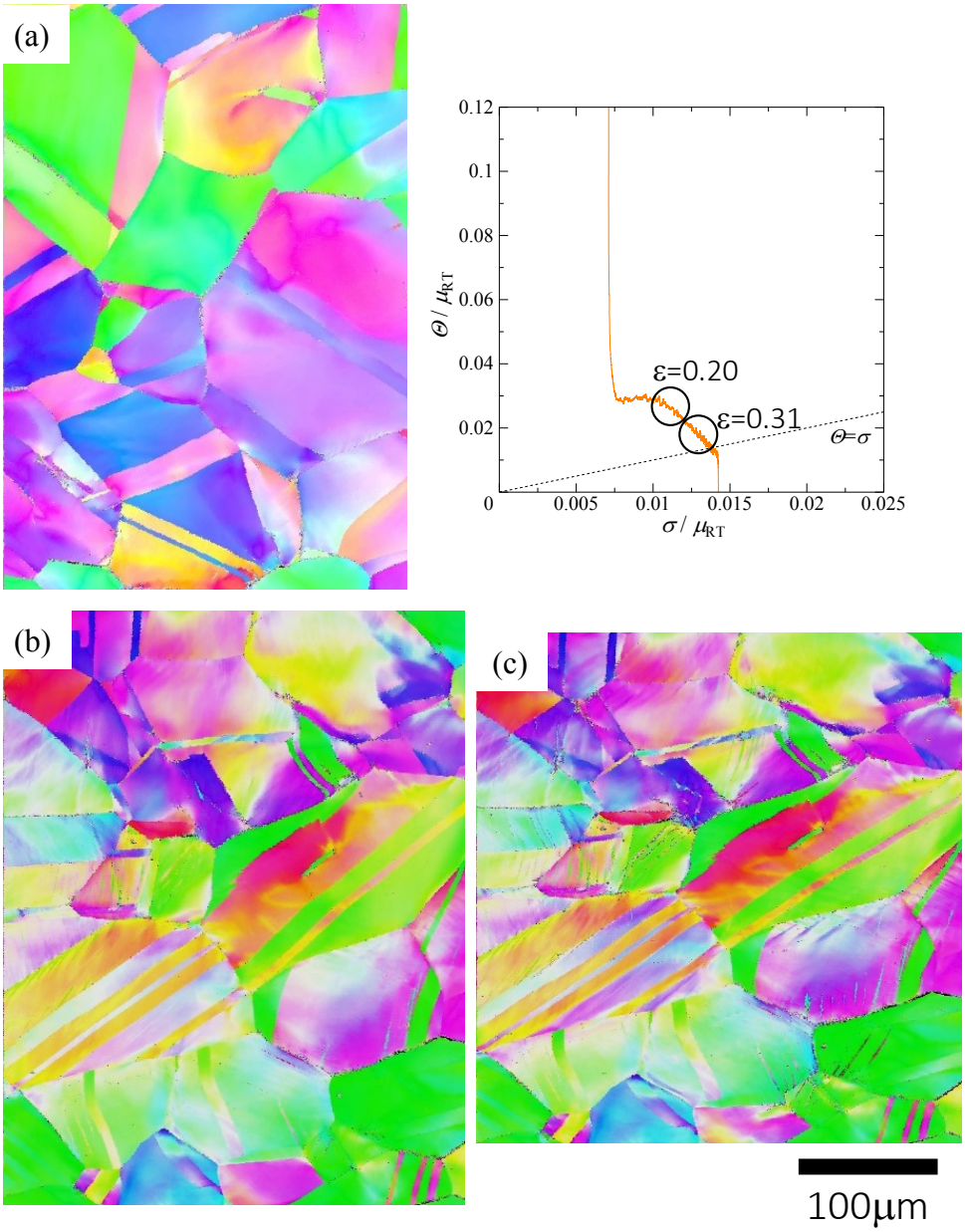

Fig. 4.9 IPF maps for the Zn-added 1123-600 specimen aged at 723 K for 0.30 ks and tensile deformed at 298 K to the strain of (a) 0.20, (b) 0.25 and (c) 0.31. Note that (b) and (c) show the same field on the specimen.

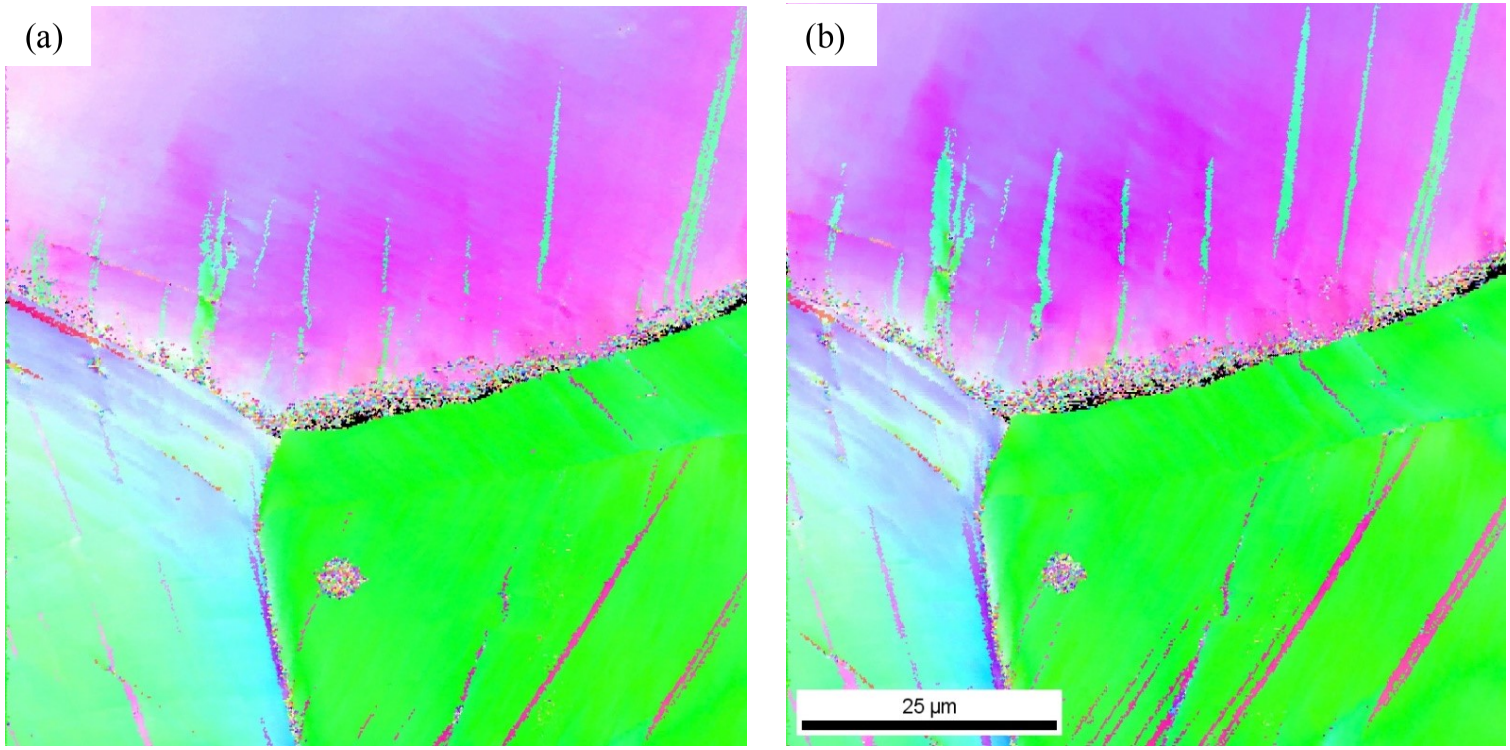

Fig. 4.10 High magnification of IPF maps of for the Zn-added 1123-600 specimen aged at 723 K for 0.30 ks and tensile deformed at 298 K to the strain of (a) 0.28 and (b) 0.31.

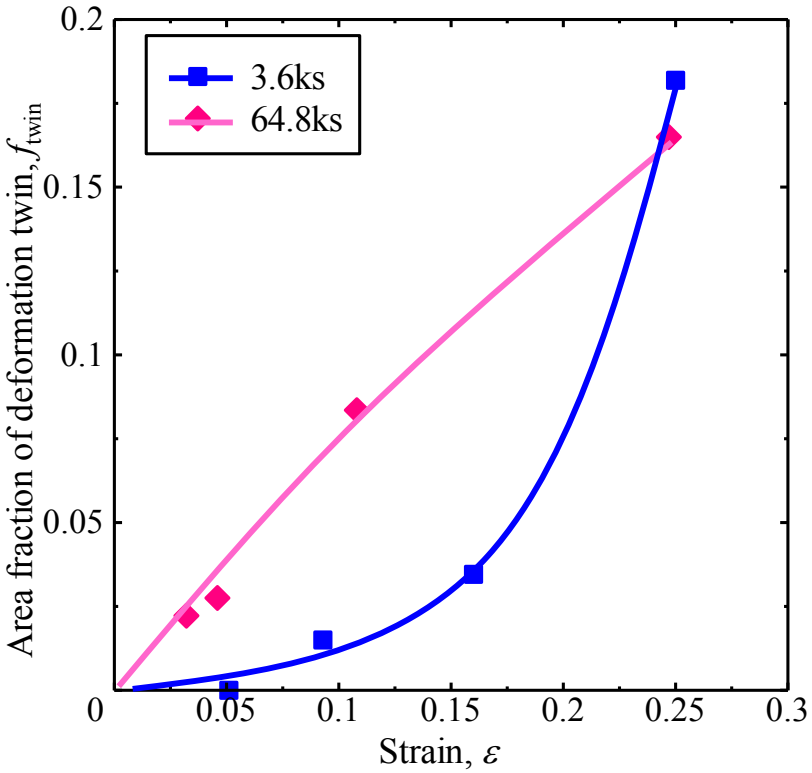

Fig. 4.11 Area fraction of the deformation twin as a function of strain in the 1123-600 specimen aged at 723 K for 3.6 ks and 64.8 ks deformed at 77 K..

.

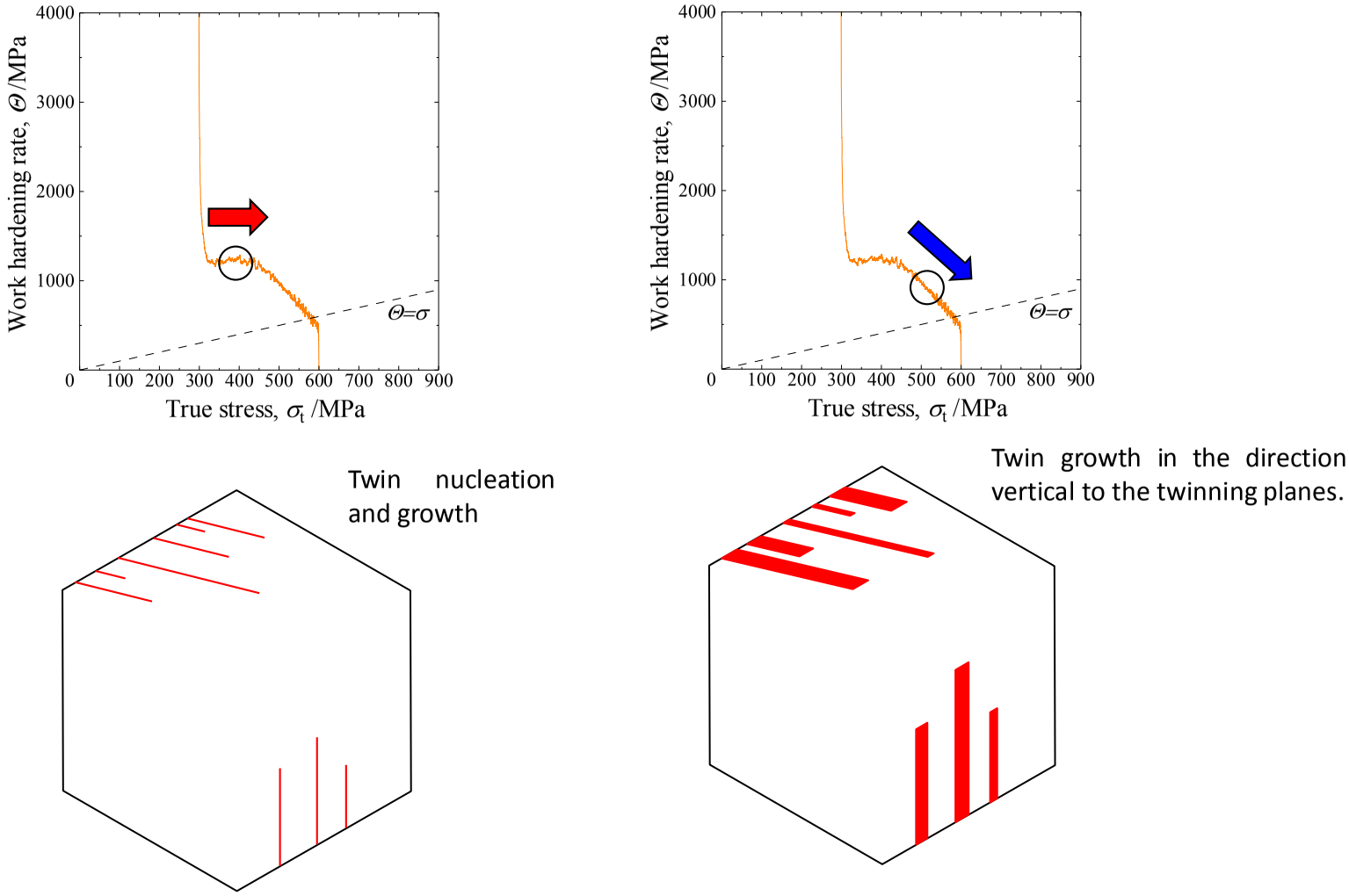

Fig. 4.12 Schematic illustrations for the deformation twinning in the Zn-added specimen aged at 723 K for 0.30 ks deformed at room temperature.

Chapter 5

Effect of precipitates on the deformation twinning

5.1. Introduction

In Chapter 3, it has been concluded that the precipitates are shearable up to the aging condition of 3.6 ks at 723 K and change to non-shearable after the aging condition. In chapter 4, it has been revealed the deformation twinning significantly depends on the precipitate state. The influence of second phase particle on the twinning behavior has not been systematically investigated. For some case, it has reported that the precipitates delay in formation or to suppression of twinning because of the difficulty or impossibility of propagating a twin across a partly coherent or incoherent boundary [1]. In this study, however, the precipitates enhanced the deformation twinning as shown in chapter 3 and chapter 4. It was also expected that the combination of precipitation hardening and deformation twinning can achieve high strength and formability. Therefore, it is important to clarify the effect of the precipitates on the deformation twinning.

Now, the fact is paid attention that the acceleration in the work hardening during room temperature deformation was observed only in under-aged specimen and it is the most remarkable in 3.6 ks aged specimen, but not in as-solution-treated and over-aged specimen of which the tensile strength is higher than that of the under-aged specimen. The aging condition of 3.6 ks at 723 K corresponds to when the precipitates transit from shearable to non-shearable. This result suggests the tendency of the twinning deformation depends not only on the applied stress but also on the interaction between the precipitates and dislocations, i.e. the deformation twinning is accelerated by the existence of shearable precipitates, while it is decelerated by the non-shearable precipitates. Furthermore, it was observed that the deformation twins nucleated near grain boundary. From these results, several possibilities can be considered for the effect of precipitates on the deformation twinning:

- The fine precipitates act as the nucleation site of the deformation twins
- The coarse precipitates restrict the formation of the deformation twins
- The precipitates increase the stress acting on grain boundaries, resulting in twinning

In addition, it can be assumed that the no deformation twin forms in the 1073-30 specimen aged at 723 K from Fig. 3.1(c). Therefore, the solution treatment condition also affect the formation of the deformation twins. E. Danaf *et al.* [2] also suggested that the critical stress for twinning increase

as grain size decrease. J. D. Evensen *et al.* [3] reported that the stress acting on the grain boundary due to the intersection of a slip band with the grain boundary is a sum of applied stress and the stress concentration on slip planes. E. Hornbogen and K. H. Zum Gahr [4] explained that the dislocation slip concentrates on a few planes when the obstacles in matrix can be sheared by dislocations, in contrast it is homogeneous when the obstacles are non-shearable.

In this chapter, the twinning tendency dependence on the aging condition will be discussed from the points of micro view using TEM observation on the precipitates and twins and macro view using slip line observation. The objective of this chapter is to investigate the effect of precipitate on the deformation twinning.

5.2. Experimental

The specimen investigated in this chapter is the Base alloy with the chemical composition given in Table 2.1. In order to observe the precipitates and the deformation twins directly, TEM was conducted using a JEOL JEM-3010 transmission electron microscope operating at 300 kV for the specimens aged for various times and deformed by 10 % in tension at 77 K.

For the slip line observations, differential interference observation using optical microscope with Nomarski prism was conducted on the specimens aged for various times, electropolished and deformed by 2 % in tension at room temperature.

5.3. Result

5.3.1. Interaction between precipitate and deformation twinning

Fig. 5.1 is the dark-field TEM image showing the precipitate and the deformation twin in the over-aged 1123-600 specimen. It looks the precipitate restricted the propagation of the deformation twins and the precipitate got damaged by the deformation twin. However, few deformation twin was observed in the over-aged specimen as shown in Fig. 4.2. Furthermore, no precipitate and deformation twin were observed which interact with each other in the under-aged specimen.

5.3.2. Slip line observation

Fig. 5.2 shows the surface observations for the 1123-600 specimens aged at 723 K for various times and deformed by 2 % in tension at room temperature. The distribution of the slip line changed as aging progressed, i.e. the slip lines in the as-quenched specimen had a relatively uniform distribution, then the distribution became heterogeneous as aging progressed up to 3.6 ks and finally became uniform after 3.6 ks. **Fig. 5.3** also shows the surface observation for the specimens with various solution treatment condition aged at 723 K for 3.6 ks and deformed by 2 %. It became hard to observe the slip lines as the grain size decreased.

5.4. Discussion

5.4.1. Role of precipitates on the deformation twinning

The TEM image for the over-aged specimen deformed by 10 % at 77 K indicates the possibility that the coarse precipitate can restrict the propagation of the deformation twins. However, considering the fact that the only a few number of the deformation twins could be observed in TEM, there should be another mechanism that restricts the nucleation of the deformation twin in the over-aged specimen. In contrast, no precipitate was observed which aids the nucleation of the deformation twins. In addition, it was found that the deformation twins have nucleated at the grain boundary in Chapter 4. Therefore, the possibility that the precipitates act as the nucleation site can be denied.

Now, the indirect effect of the precipitates on the deformation twinning should be concerned. In this work, a parameter average slip line spacing (ASLS) is introduced in order to explain the indirect effect. **Fig. 5.4** shows the ASLS in the 1123-600 specimen as a function of aging time obtained from the slip line observation shown in Fig. 5.2. The ASLS was obtained from at least 10 grains at each aging condition. One can see that the ASLS increase until 3.6 ks and then decrease after the aging condition.

Hornbogen and Zum Gahr [4] reported that the distribution of the dislocation slip depends on the interaction between the obstacles and the dislocations: (1) for the solid solutions, the slip distribution is, for example, determined by the stacking fault energy, (2) when the obstacles are

non-shearable, the slip is spread homogeneously over the volume due to preferred work hardening of particular slip planes and (3) when the obstacles are shearable, the slip is concentrated on a few planes because of local work softening resulting from the decrease of the effective diameter. Poole *et al*. [5] also reported that the slip lines clearly appear when the precipitates are shearable, it becomes unclear and no slip line are observed in over-aged condition for an aluminum alloy.

The increase of the ASLS means the formation of shearable precipitates and the decrease of the ASLS means the formation of non-shearable precipitates. Therefore, the aging condition when the ASLS is maximal, 3.6 ks aging at 723 K in this work, indicates the shearable/non-shearable transition of the precipitates. This aging condition is coincides with the condition determined from the analysis of the initial work hardening rate and the Bauchinger effect given in Chapter 3.

The passed dislocations will pile up on the grain boundary in polycrystalline materials. Therefore, it is obvious that the slip concentration on a specific planes, for the case of shearable precipitates, causes the local stress concentration at the point where the slip plane and grain boundary cross as schematically illustrated in **Fig. 5.5(a)**. A simple model for the stress acting on the grain boundary, σ_{GB} due to the intersection of a slip band with the grain boundary is:

$$\sigma_{GB} = \sigma_{app} + \left(\frac{d}{w}\right)^{1/2}\left(\sigma_{app} - \sigma_0\right) \tag{5.1}$$

where σ_{app} is the applied stress at the far field, d is the length of the slip band which can be approximated by the grain size of the material, w is the width of the slip band and σ_0 is the resistance within the slip band due to precipitates. Thus the nucleation of deformation twins would be expected when the stress acting on grain boundary given by equation (5.1) was equal to the critical stress for twinning. This is the reason the deformation twins form near the grain boundary as shown in Fig. 4.7.

The slip distribution becomes homogeneous when the precipitates are non-shearable, on the other hand, resulting in the homogeneous stress distribution as illustrated in **Fig. 5.5(b)**. In this case, it is difficult for the stress acting on grain boundaries to exceed the critical stress for twinning deformation. Thus, the deformation twinning hardly happens in the over-aged specimens.

The critical factor for the deformation twinning in the Cu-Ni-Si alloy is, thus, the stress acting

on grain boundaries which determined by the superposition of the precipitation strengthening, work hardening and the stress concentration caused by the localized dislocation slip. As shown in Fig. 2.7, the peak-aged condition is 64.8 ks at 723 K and thus the applied stress is the highest. On the other hand, Fig. 5.4 indicates that the stress concentration increases until 3.6 ks and decreases after 3.6 ks. It can be estimated, therefore, that the possibility of deformation twinning is maximal between 3.6 ks and 64.8 ks aged condition.

5.4.2. Effect of solution treatment condition on deformation twinning

From Fig. 5.3, it is obvious that the dislocation slip occur homogeneously in the 1073-30 specimen aged at 723 K for 3.6 ks. This is because the precipitates formed in the 1073-30 specimen change to non-shearable in early stage of aging treatment as discussed in Chapter 2. Furthermore, equation (5.1) also indicates the effect of grain size on the stress acting on grain boundary, i.e. the smaller the grain size, the smaller stress acting on grain boundary. Therefore, the deformation twinning hardly happen in the 1073-30 specimens. Thus, the deformation twinning in Cu-Ni-Si alloy is also affected by the solution heat treatment condition and aging condition.

5.5. Conclusion

(1) The critical factor for the deformation twinning in the precipitate strengthening Cu-Ni-Si alloy is the stress acting on grain boundaries. When the stress on a grain boundary exceeds the critical for deformation twinning, the deformation twins formed from the grain boundary.

(2) The applied stress on grain boundary is determined by the superposition of the stress caused by precipitation strengthening, work hardening and the stress concentration caused by the localized dislocation slip.

(3) It is hard for the deformation twinning to occur in the 1073-30 specimen because the precipitates changes to non-shearable in early stage of aging treatment and due to the small grain size.

Reference

[1] J.W. Christian and S. Mahajan: Prog. Mater. Sci., **39** (1995), 1.

[2] E. El-Danaf, S.R. Kalidindi, and R.D. Doherty, Metal. Mater. Trans. A, **30** (1999), 1223.

[3] J.D. Evensen, N. Ryum and J.D. Embury, Mater. Sci. Eng. **18** (1975), 221.

[4] E. Hornbogen and K.H.Zum Gahr: Metallography, **8** (1975) 181.

[5] W. J. Poole, X. Wang, D. J. Lloyd abd J. D. Embury: Philos. Mag., 85 (2005), 3113.

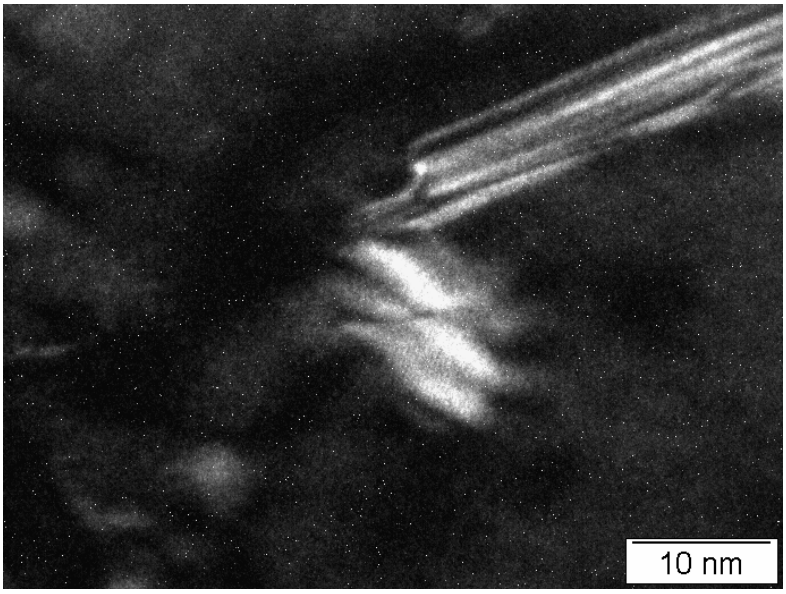

Fig. 5.1 TEM dark-field image for the 1123-600 specimen aged at 723 K for 1209.6 ks and deformed by 10 % at 77 K.

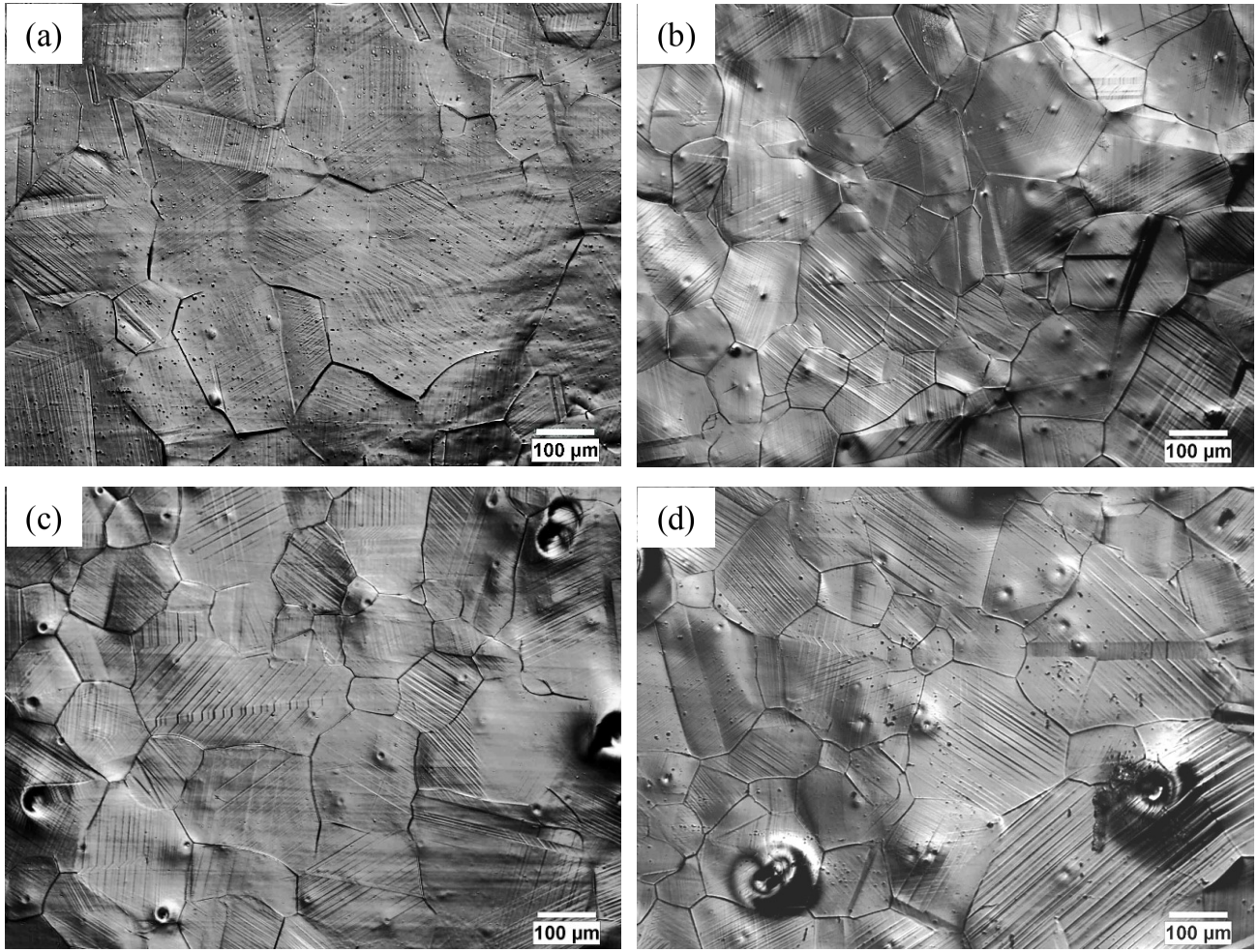

Fig. 5.2 Observations of the 1123-600 specimen surface after deformation by 2 % using Nomarski interference contrast. The specimens have been aged at 723 K for (a) 0 ks (as-quenched specimen), (b) 0.30 ks, (c) 1.2 ks, (c) 3.6 ks (d) 14.4 ks, (e) 64.8 ks, (f) 345.6 ks and (g) 1206.9 ks.

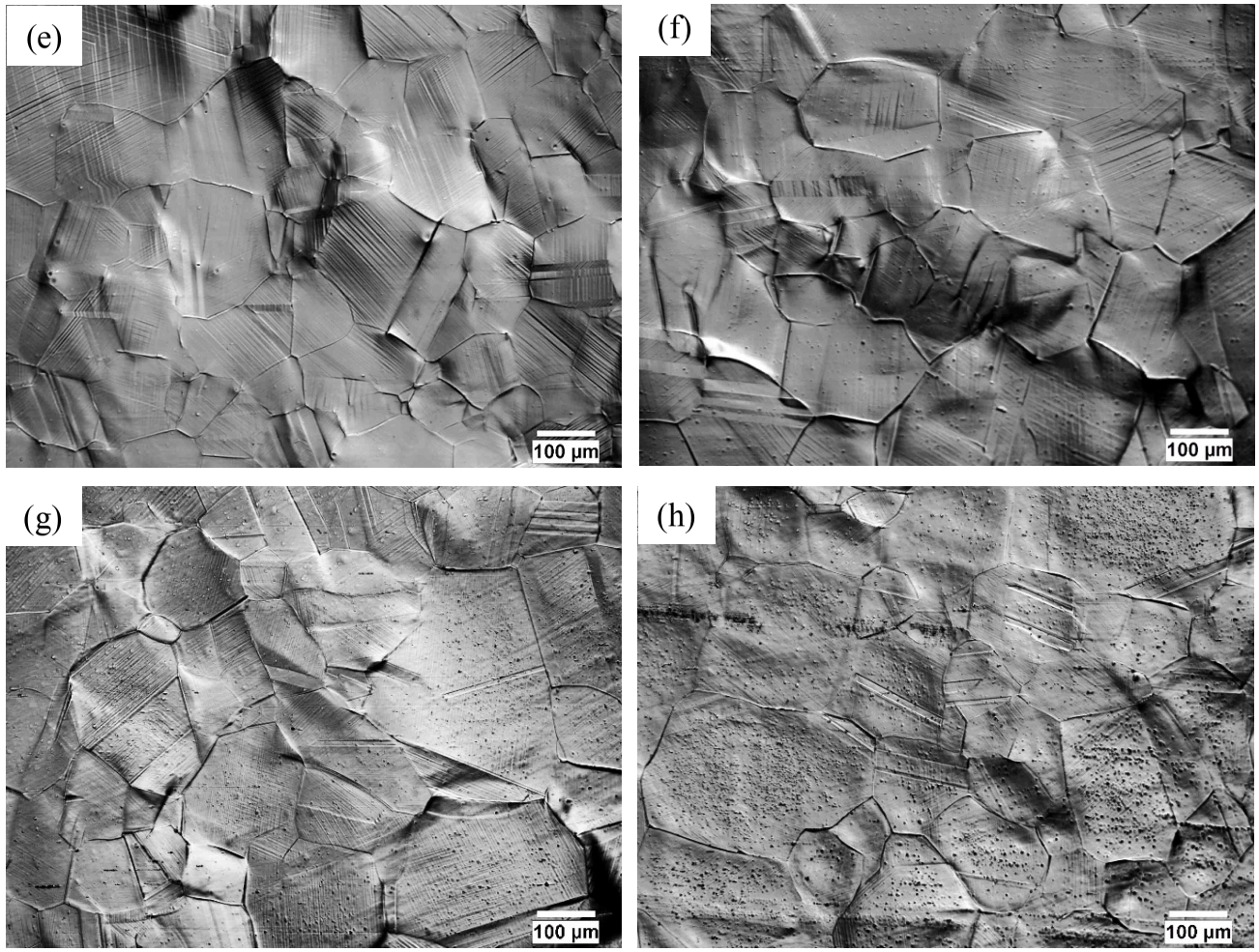

Fig. 5.2 Continued.

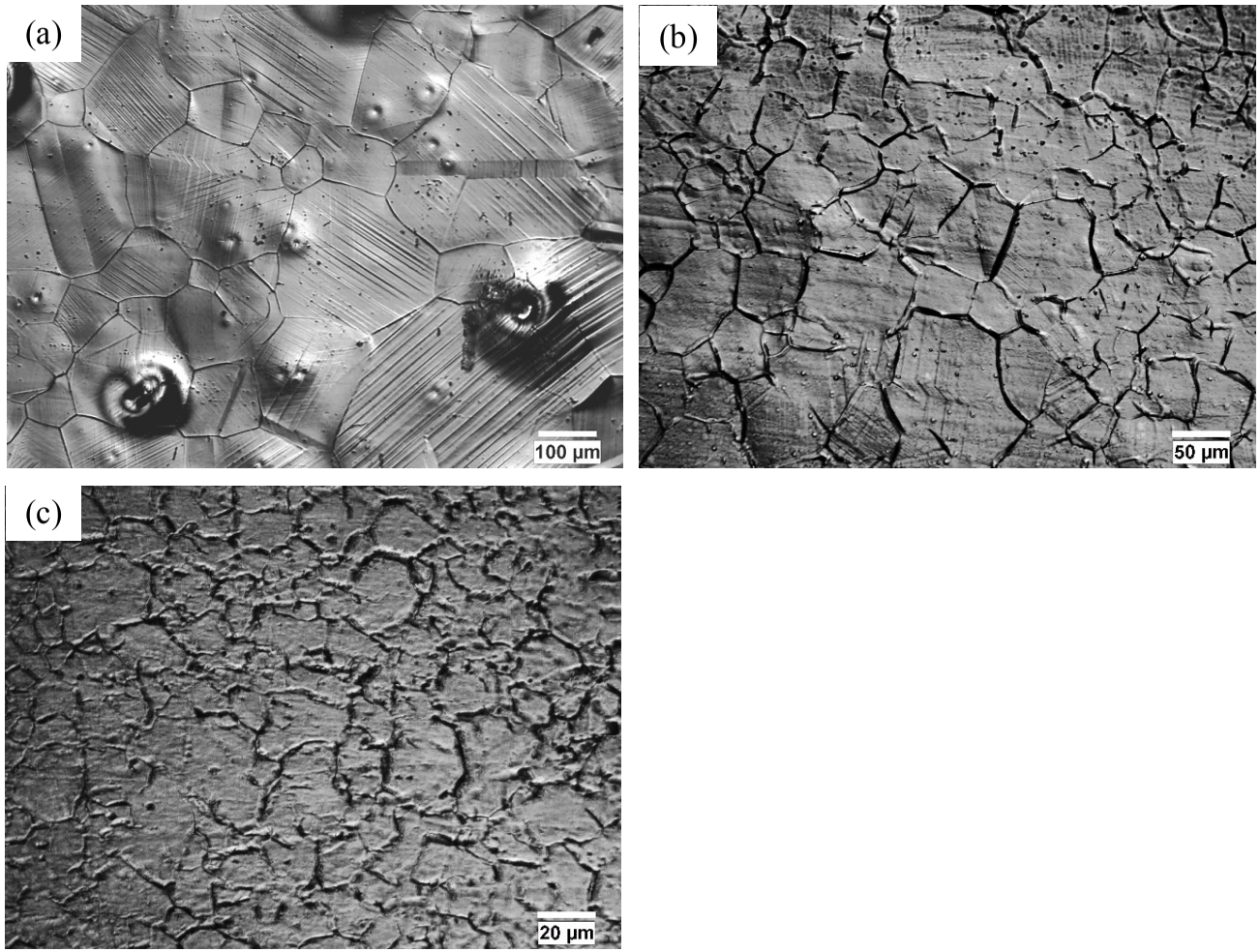

Fig. 5.3 Observations of the specimen surface after deformation by 2 % using Nomarski interference contrast. The specimens have been aged at 723 K for 3.6 ks for the (a) 1123-600, (b) 1123-30 and (c) 1073-30 specimens.

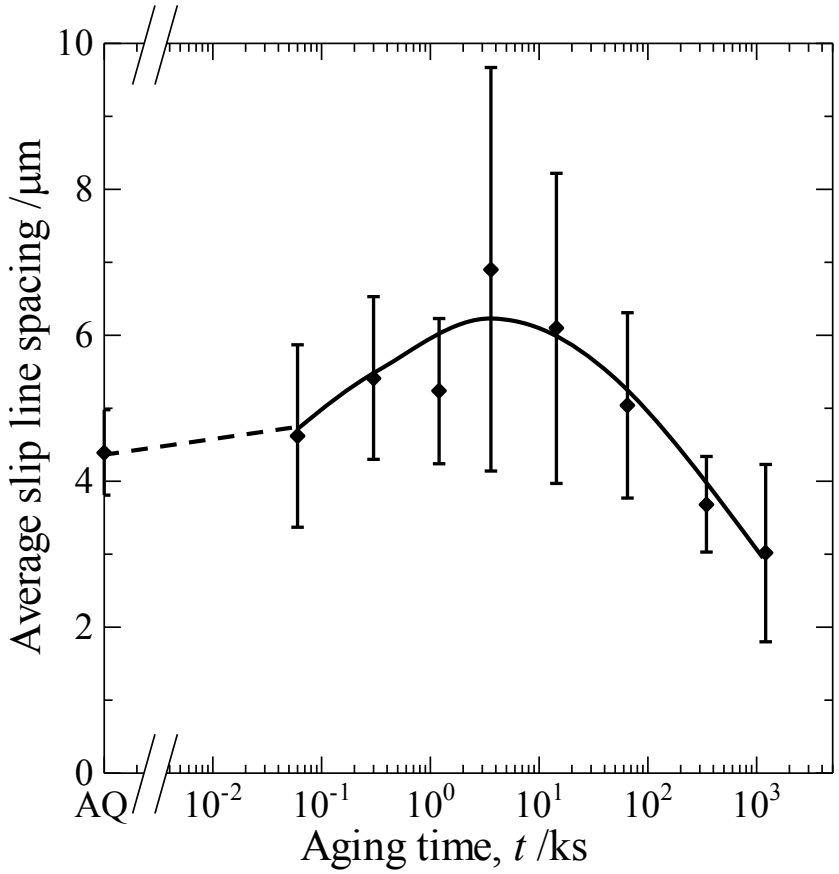

Fig. 5.4 Average slip line spacing (ASLS) on the 1123-600 specimen aged at 723 K for various times and deformed by 2 % at room temperature

(a)

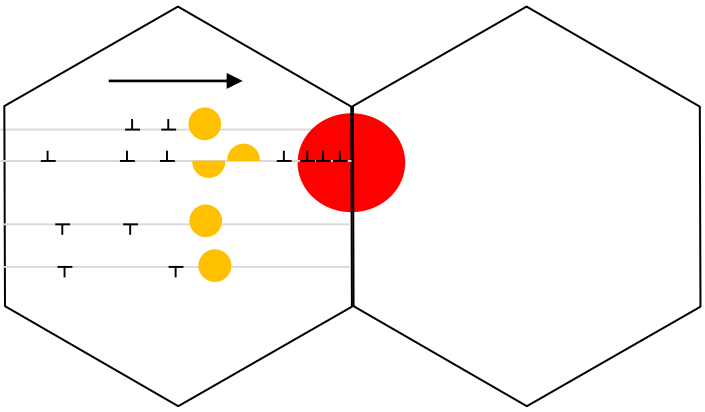

(b)

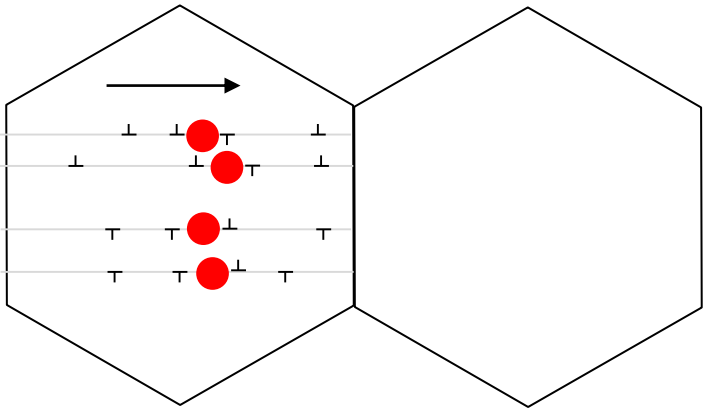

Fig. 5.5 Schematic illustrations for (a) slip localization and (b) homogeneous dislocation slip.

Chapter 6
General conclusion

General conclusions

The principal objective of this thesis described in chapter 1,

"To clarify deformation twinning behavior with precipitate strengthening in Cu-Ni-Si alloys" is successfully achieved throughout the previous chapters. In this chapter, conclusions of the present thesis are summarized based on both the obtained results and discussions described in each chapter.

In Chapter 1 **"General introduction"**, background, current problems and objectives of this thesis are presented. Especially, the importance of clarifying the precipitation process in the early stage of aging and the effect of the precipitate on the work hardening behavior is described.

In Chapter 2 **"Precipitation behavior in Cu-Ni-Si alloy"**, two different precipitates are found to form in this alloy system using DSC and TEM observation. The differences of the two precipitates are demonstrated in this chapter. X-phase is the main precipitating phase during aging treatment at 573 K, whereas the δ-Ni_2Si phase is the main precipitating phase during aging treatment at 723 K. The formation of X phase cause the two-stage hardening behavior.
The size, volume fraction and number density of δ-Ni_2Si as a function of aging time at 723 K is also investigated in this chapter using resistivity measurements and TEM observations.

In Chapter 3 **"Work hardening behavior in Cu-Ni-Si alloy"**, the interaction between the precipitates and dislocations was investigated from the analysis of the initial work hardening rate and the Bauchinger effect. The shearable/nonshearable transition occur at the aging condition of 3.6 ks at 723 K in the specimen with large grain size and low dislocation density. In addition, it was estimated that the most of precipitates are non-shearable after the peak-aged condition. TEM observation confirmed that the precipitate is cut by dislocations before the transition, and the dislocation loops are left around the precipitates after the transition. The transition time becomes earlier in the specimen with high dislocation density because the precipitates can easily form and grow on the dislocations.

The formation of the thin deformation twins was found in the under-aged Cu-Ni-Si alloy deformed at room temperature. In addition, the formation of the deformation twins accelerates the work hardening, resulting in the increase of the work hardening rate.

In Chapter 4 **"Deformation twinning behavior in Cu-Ni-Si alloys"**, the work hardening behavior and microstructure change during tensile deformation of Cu-Ni-Si alloy deformed at 77 K and of Cu-Ni-Si with high content of Zn deformed at room temperature have been investigated. The results for the Cu-Ni-Si alloy deformed at 77 K indicated that the deformation twinning significantly depends on the precipitate state. Investigations for the under-aged and peak-aged specimen revealed the applied stress is a significant factor for the deformation twinning. While the deformation twinning behavior in the over-aged specimen cannot be explained from the point of the applied stress.

Microstructure observation for the Zn-added Cu-Ni-Si alloy revealed the deformation twins first nucleates at the vicinity of the grain boundaries, and then grows as strain increases. Furthermore, the formation of the deformation twins results in the low and constant work hardening rate and high elongation. The combination of the precipitation hardening and twinning deformation is expected to achieve high strength and formability.

In Chapter 5 **"Effect of precipitates on the deformation twinning"**, the cause of the deformation twinning is explained from both micro and macro point of view using TEM observations and slip line observations. The TEM suggested the possibility that the coarse precipitates can restrict the propagation of the deformation twins, while fine precipitates have no direct effect on the deformation twinning.

The slip line observation revealed that the dislocation slip localized on a few slip planes in 3.6 ks aged condition, while the slip distribution was very homogeneous in over-aged condition. The results suggested the stress concentration is another significant factor for the deformation twinning, and the superposition of the precipitation strengthening and the stress concentration successfully explained the twinning deformation behavior in the Cu-Ni-Si alloy.

In Chapter 6, **“General conclusions”**, conclusions obtained each chapter are summarized.

Acknowledgement

I would like to thank Prof. Tatsuo Sato for his supervision through my studies for 5 years. He gave me many lessons including the ways of thinking and how a researcher should be. His critical comments on my study guided to the successes. The Paper Award of Japan Institute of Copper, The Best Paper Award (Young Best Paper) of The Japan Institute of Metals and Materials and The Best Presentation Award at the Second International Education Forum on Environmental and Energy Science provided me unforgettable memories in my life and these awards were definitely owes to his dedicated guidance. I am very glad to graduate with him from Tokyo Tech.

I greatly appreciate Prof. Warren Poole for his very kind supervision during my study at UBC for a half year and two weeks. His advice helped me a lot every time until the end of my research. The studies at UBC also give me friends overseas. I also would like to express my appreciation to Dr. Azizi Hamid and Dr. Kim Wonsang to their great help and advice.

I also appreciate Prof. Masao Takeyama, Shinji Kumai and Masato Sone for their critical comments and valuable advice on my thesis. I would like to thank again Prof. Takeyama for his help on the ACEEES program.

I deeply thank Associate Prof. Equo Kobayashi for his advice and concern. He also showed how to enjoy the life in/outside the laboratory. I deeply appreciate Mr. Hiroyasu Tezuka for his advice and concern. His advice on my study and my life encouraged me.

I also would like to thank Furukawa Electric Corporation for their material supply for my 5 years research. I deeply thank Dr. Kiyoshige Hirose for his kind advice, comment and discussion.

My thanks are also extended to my colleagues at Sato-Kobayashi Lab. I appreciate Dr. Chakkrist, Dr. Hyun-Bom Lee, Dr. Kim JaeHwang, Dr. Z. Zhang and Dr. Y.C.D. Lee who showed me the best attitude as a Doctor Course student. I also thank Ms. A. Tsuno and Mr. Y. Ishizuka who are the senior in Cu-Ni-Si project. I thank to Mr. A. Ohtani, Mr. T. Chijiiwa, Mr. A. Hatori, Mr. T. Hasebe and Mr. Y. Yokoyama who are classmates encouraged me. I also thank to all students: Ms. Yorina S.F. Lantang, Ms. SeongNyeong Kim, Ms. Mihara, Mr. Ishikawa, Mr. Furuta and Mr. Tani.

Finally, I deeply wish to dedicate my accomplishment of Ph. D. to my parents and brothers.

February, 2015

Akiyoshi Araki